Study of Quasi-Elastic Scattering in the NOνA Detector Prototype

A DISSERTATION
SUBMITTED TO THE FACULTY OF THE GRADUATE SCHOOL
OF THE UNIVERSITY OF MINNESOTA
BY

Minerba Betancourt

IN PARTIAL FULFILLMENT OF THE REQUIREMENTS
FOR THE DEGREE OF
Doctor of Philosophy

Advisor
Prof. Kenneth Heller

June, 2013

Acknowledgements

I would like to thank my advisor Prof. Ken Heller and Dr. Jarek Nowak for all the cooperation in the realization of this work and for the support they always offered me.

I also want to express my sincere gratitude to Prof. Mayly Sanchez for her appreciable advice along the graduate school. I learned a lot about physics and data analysis from her. Thank for the teaching and guidance you always offered to me.

I am grateful to many professors at the collaboration, especially to Prof. Hugh Gallagher, Prof. Tricia Vahle, Prof. Gregory Pawloski, Prof. Alex Sousa and Prof. Mark Messier. I learned a lot about data analysis and physics from them.

I would like to say thanks to the entire collaboration for giving me the opportunity to work with them. This thesis work represents the hard work of many people who brought up the detector and made the data taken happen.

I am grateful to the Fermilab people for their collaboration, specially Brian R., Gavin, Denis, Nathan, Mat, Robert, Peter and Jon Paley from Argonne National Laboratory. Also, thanks to my classmates at University of Minnesota, specially Susan, Kanika, Nick, Dominick and Jan.

Thanks to my Mom and Dad for been there when I needed.

Thanks to my friends, specially Addis, Olga, Cyndee and Melissa for their support along graduate school.

Thanks to Jesus Orduna for the company and words when I needed along the last years of the graduate school.

And to all those persons with whom I have shared difficult moments and helped me in the struggle to get the win today.

Thanks to the University of Minnesota graduate school Doctoral Dissertation Fellowship.

Dedication

I dedicate my dissertation work to my family, specially my mom Olga, my dad Luis, my grandmother Patricia, my sisters Mileidy and Ninoska.

Abstract

NOvA is a 810 km long base-line neutrino oscillation experiment with two detectors (far 14 KTon and near detector 300 Ton) currently being installed in the NUMI off-axis neutrino beam produced at Fermilab. A 222 Ton prototype NOvA detector (NDOS) was built and operated in the neutrino beam for over a year to understand the response of the detector and its construction.

The goal of this thesis is to study the muon neutrino interaction data collected in this test, specifically the identification of quasi-elastic charged-current interactions and measure the behavior of the quasi-elastic muon neutrino cross section.

This thesis presents the analysis of the data from two detector configurations, the first configuration collected data from 1×10^{19} protons on target (POT) from April to May 2011 and the second configuration collected data from $1.7 \times 10^{20} POT$ from October 2011 to April 2012. The charged current quasi-elastic muon neutrino events collected with each configuration were analyzed to extract the cross section as a function of energy $\sigma(E_\nu)$ as well as the single differential cross sections with respect to outgoing muon momentum, $\frac{d\sigma}{dP}$, outgoing muon angle from the incident neutrino direction, $\frac{d\sigma}{d\cos\theta}$ and the momentum transfer squared of the interaction, $\frac{d\sigma}{dQ^2}$.

Contents

Introduction

The Quasi-Elastic cross section is not well understood in the energy range of the NOνA experiment, specifically at energies around 2 GeV and below. This region is crucial to NOνA, since electron neutrinos from the oscillation from muon neutrino to electron neutrino occur in this region. Experiments such as MiniBooNE and NOMAD made recently cross section measurements [1]. They have covered energy regions above and below 2 GeV; but where their data overlap, around 2 GeV, these experiments show discrepancies with each other and with theoretical predictions.

The goals of this thesis is to investigate the detector design for the NOνA experiment, evaluate its performance and study Charged Current Quasi-Elastic (CC QE) interactions using the data collected from the NOνA Detector Prototype. This thesis is structured as follows:

- Chapter 1 briefly presents the history of the discovery of neutrinos, neutrino cross sections and neutrino oscillation.
- Chapter 2 summarizes the theory of neutrino cross sections and presents a review of the CC QE cross section measurements.
- Chapter 3 describes the experiment, the neutrino beam, the NOνA detector technology and the Detector Prototype used for the measurements in this thesis.
- Chapter 4 describes the software used to simulate the detector, reconstruct the events detected, and calibrate the detector.
- Chapter 5 gives the event selection criteria and demonstrates the implementation of the event selection for simulated events. This chapter also describes the determination of the neutrino energy and four momentum transfer.
- Chapter 6 presents the analysis. This chapter gives the prediction for the background and signal events using MC simulations, explains the cross section measurement with details about the background subtraction, efficiency, resolution correction and the

number of neutron targets. It also presents the results of the cross sections measurements.

- Chapter 7 presents details about possible systematic uncertainties in the measurement.
- Chapter 8 presents a summary of what was learned about the detector design, compares the cross-section measurements to that of other experiments, discussion and gives future prospects for the NOνA Near Detector.

Chapter 1

The Physics of Neutrinos

1.1 A Brief History of Neutrinos

The basic properties of neutrinos have been studied for many years. The first experimental evidence for neutrinos was obtained in 1956 by Reines and Cowan [2]. Since then, many experiments have investigated the properties of the neutrinos. This section presents a brief review of history of neutrinos, specifically the discovery of three types of neutrinos, neutrino cross-section measurements and the discovery of neutrino oscillations.

1.1.1 The discovery of three types of neutrinos

The neutrino was first postulated by Pauli in 1930 to explain the results from the beta decay process. Beta decay experiments showed that emitted electrons have a continuous energy spectrum. At that time, it was believed that only a single electron was emitted during this process. But the continuous energy of the electron violated the principle of the conservation of energy. Pauli then suggested that another particle was emitted along with the electron that was not and probably could not be observed. He proposed the existence of a neutral particle that later Fermi gave the name of neutrino.

The first experimental evidence for neutrinos was obtained by Reines and Cowan's experiment in 1956[2] through the inverse beta decay reaction:

$$\bar{\nu} + p \rightarrow n + e^{+}. \tag{1.1}$$

This experiment used electron antineutrinos from a nuclear reactor at the Savannah River Nuclear Plant. The experiment contained two tanks with approximately 200 liters of a mixture of water and Cadmium chloride. After this experiment, new experiments followed quickly to investigate the properties of the neutrino.

In 1962, muon neutrinos were discovered by Lederman, Schwartz, Steinberger, et. al. at the Brookhaven National Laboratory. This experiment used a beam of protons focused

toward a beryllium target[3]. The resulting interaction produced a large number of pions which decayed to muons and muon neutrinos.

In 1973, the Gargamelle experiment at CERN discovered the weak neutral current interaction $\bar{\nu_\mu} + e \rightarrow \bar{\nu_\mu} + e$ [4].

Much later in 2001, the tau neutrinos were detected by the DONUT experiment[5]. This experiment collided 800 GeV protons with a block of tungsten. This collision produced D_S mesons that subsequently decayed into tau-leptons which then produced tau neutrinos. These and the experiments which followed showed the existence of three neutrino flavors: the electron neutrino (ν_e), the muon neutrino (ν_μ), and the tau neutrino (ν_τ).

1.1.2 Neutrino Cross Section

Experiments have studied neutrino cross sections in three different energy ranges, from 1 MeV to 100 MeV (low energy), from 0.1 GeV to 20 GeV (intermediate energy) and from 20 GeV to 350 GeV (high energy). We present a brief summary of those cross sections experiments.

Low energy cross sections have been measured from inverse beta decay using different targets: deuterium and nuclear target such as ^{12}C,^{2} H,^{56} Fe,^{71} Ga,^{127} I.

For the inverse beta decay, neutrinos are produced from the fission of ^{239}Pu,^{241} Pu and ^{238}U [6]. The most precise determination of the cross-section is from the Bugey nuclear power plant in 1994, they report a high precision measurement at 15m from a 2800 MWth reactor. This experiment reported the ratio of measured cross-section to the expected theory of the weak interactions $\frac{\sigma_f}{\sigma_{V-A}} = 98.7\% \pm 1.4\% \pm 2.7\%$ [7]. A compilation of inverse β decay cross sections is found in [8].

In 1980 Los Alamos studied electron neutrino interactions with deuterium, $\nu_e d \rightarrow e^- pp$. This experiment used a six-ton Cherenkov counter filled with D_2O . The experiment reported a cross-section measurement $\sigma(\nu_e d \rightarrow e^- pp) = (0.52 \pm 0.18) x 10^{-40} cm^2$ [9]. Other, direct cross-section measurements have been made using antineutrinos from nuclear reactors for both the charged current ($\bar{\nu}_e d \rightarrow e^+ nn$) and the neutral current ($\bar{\nu}_e d \rightarrow \bar{\nu}_e pn$) interactions at Savannah River, ROVNO, Bugey and Krasnoyarsk [10].

In addition, several experiments have made measurements for neutrino interactions on nuclei at low energies (1-300) MeV. For example the KARMEN experiment in 2005 studied $\nu_e^{12} C \rightarrow (e^-) +^{12} N$ and reported a measurement of the flux average cross section $(9.1 \pm 0.5(stat) \pm 0.8(sys)) \times 10^{-42} cm^2$. Experimental data is also available from LAMPF, E225, LNSD, GALLEX and SAGE experiments. A compilation of all the experimental data is found in [8].

Intermediate energy neutrino cross sections in the 0.1-20 GeV range have been made

using deuterium and heavier nuclear targets. These measurements include the cross sections for quasi-elastic, resonance and deep inelastic interactions. Early measurements from the 1970s and 1980s were made using either bubble chamber or spark chambers detectors. For example the BNL 7-foot bubble chamber in 1981 measured the total cross section $\sigma_T(\nu n)/E_\nu = (1.07 \pm 0.05) \times 10^{-38}$, $\sigma_T(\nu p)/E_\nu = (0.54 \pm 0.04) \times 10^{-38}$, and $\sigma_T(\nu N)/E_\nu = (0.80 \pm 0.03) \times 10^{-38} cm^2/GeV$. Furthermore, cross section measurement for this have been made using different nuclei such as C, F_e, H_2O. The experimental data available is extensive and a compilation is found in [8]. A detailed review of the experimental data for this energy range, specifically for the quasi-elastic cross section is presented in Chapter 2.

Finally, high energy neutrino cross section measurements in the 20 GeV to 350 GeV range have been made for both neutrinos and antineutrinos in experiments such as BEBC, CCFR, CDHS, ZP C35, GGM-SPS, PL, IHEP-ITEP, MINOS, NOMAD and NuTeV. The world-average cross section for neutrinos $\sigma_\nu/E_\nu = (0.677 \pm 0.014) \times 10^{-38} cm^2/GeV$ and for antineutrinos $\sigma_\nu/E_\nu = (0.334 \pm 0.008) \times 10^{-38} cm^2/GeV$ [8].

1.1.3 Neutrino Oscillations

In 1957 Pontercorvo and Sakata proposed a new phenomenon for neutrinos, called neutrino oscillation. From the formulation of neutrino oscillations, the three flavor states of neutrinos ν_e, ν_μ, ν_e are related to the mass eigenstates ν_1, ν_2, ν_3 by the 3×3 PMNS neutrino mixing matrix[11]. This matrix is expressed in terms of the mixing parameters $\theta_{12}, \theta_{23}, \theta_{13}$ and a CP violating phase δ. Currently, experiments that study neutrino oscillations provide values for θ_{12}, θ_{23} and θ_{13}, and for the square of the mass differences Δm^2_{12}, Δm^2_{32}, where $\Delta m^2_{ij} = m^2_i - m^2_j$ gives the mass differences of the mass eigenstates.

The first experimental result indicating neutrino oscillation was in 1968[12], Davis Homestake experiment measured the flux of neutrinos from the sun and detected a deficit when compared with the prediction of Bahcall's Standard Solar Model. This discrepancy was called the solar neutrino problem. The Davis experiment used a chlorine-based detector and radiological techniques to measure the flux of solar neutrinos interacting in the detector.

In 1988, a similar deficit of atmospheric muon neutrinos was observed by the Kamiokande experiment [13].

In 1998, the Super-Kamiokande experiment studied the interactions of both solar and atmospheric neutrinos [14]. This experiment used a cylindrical stainless steel tank with 50Ktons space of water surrounded by 11,146 photomultipliers. The deficit in the angular and energy distribution was explained by neutrino oscillations.

In 2002, the SNO experiment made precise measurements of solar neutrinos[15]. SNO

is a heavy water Cherenkov detector in a nickel mine in Ontario (Canada) at a depth of 204 m of rock. The detector contained 1000 tons of D_2O. This experiment measured the electron and nonelectron component of the solar neutrino spectrum by comparing the charged current and neutral current neutrino reactions on deuterium. The result from this experiment was a detailed confirmation of the flavor changing signature of neutrino oscillation.

In 2003, the KamLAND experiment found the first evidence for reactor $\bar{\nu}_e$ oscillations[16]. The neutrinos produced in nuclear power plants have energies similar to the energies of the neutrinos generated from the solar fusion cycle, 1-20 MeV. KamLAND is a liquid scintillator anti-neutrino detector that measured the $\bar{\nu}_e$ flux from nuclear reactors at an average distance of 180Km. This experiment observed 258 events with an expected 365 ± 24 events for the case of no oscillations.

The experiments Super-Kamiokande, SNO, and KamLANB provided the first precision measurements of the solar oscillation parameters $(\theta_{12}, \Delta m^2_{32})$. The current limit from this data provides the best fit parameters [17] $\sin^2 2\theta_{12} \approx 0.86^{+0.03}_{-0.04}$ and $\Delta m^2_{21} \approx 8.0 \pm 0.3 \pm 10^{-5} eV^2$.

Furthermore, experiments made measurements for θ_{23} and Δm^2_{32}, the best measurement of $\sin^2(2\theta_{23})$ is from the Super-K experiment and the most precise measurement of the mass splitting $\Delta m^2_{32} = 2.35^{+0.11}_{-0.08} \times 10^{-3} eV^2$ is from the MINOS experiment[18].

Finally, two reactor experiments, Daya Bay in China and RENO in Korea, measured this final mixing parameter θ_{13}. The Daya Bay Reactor Neutrino Experiment found $sin^2 2\theta_{13} = 0.091 \pm 0.016(stat) \pm 0.005(syst)$. At about the same time, the RENO experiment reported $sin^2 2\theta_{13} = 0.113 \pm 0.013(stat) \pm 0.019(syst)$[20]. In addition, T2K, MINOS experiments provided limits on θ_{13}. MINOS experiment reported $0.01(0.03) < 2\sin^2 2\theta_{13} \sin^2(\theta_{23}) < 0.12(0.18)$ and T2K experiment reported $0.03(0.04) < \sin^2 2\theta_{13} < 0.28(0.34)$ for $\delta = 0$ and a normal (inverted hierarchy)[19].

There is now substantial evidence that neutrinos have mass, and they oscillate between weak flavor states as they travel. This phenomenon has been observed for neutrinos from many sources, the sun, reactors, cosmic ray interactions, and accelerator beams. While these experiments tell us about neutrino mixing angles and differences in the square of their masses, we still do not have a complete understanding of neutrinos. Remaining questions in neutrino physics concern the absolute mass of neutrinos, whether there is CP violation in the neutrino sector, their mass hierarchy and if they are Dirac ($\nu \neq \bar{\nu}$) or Majorana ($\nu = \bar{\nu}$) particles.

1.2 Neutrinos in the Standard Model

The standard model describes three fundamental forces, the strong, weak and electromagnetic interactions, it does not describe the gravity. In the standard model there are three kind of elementary particles: leptons, quarks and mediators. Figure 1.1 shows the components of the standard model. There are six leptons, the charged leptons: the muon, the electron and the tau and the uncharged leptons: the muon neutrino ν_μ, the electron neutrino ν_e and the tau neutrino ν_τ. There are also six antileptons.

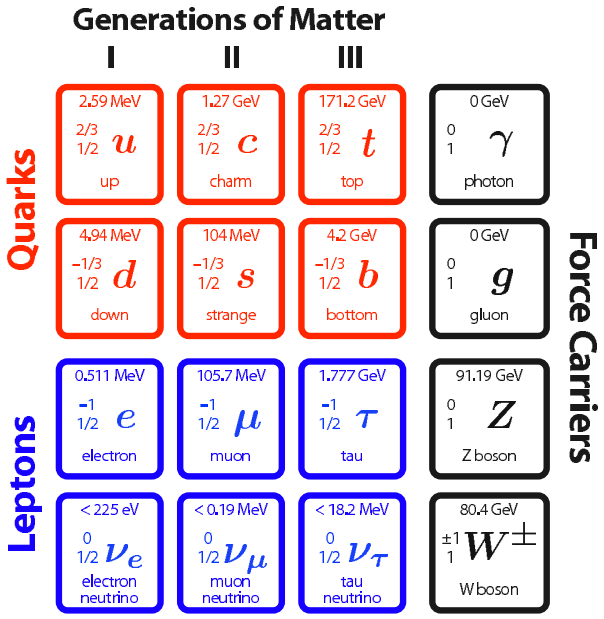

Figure 1.1: Building blocks of matter and force carrying particles in the Standard Model.

Similarly, there are six flavors of quarks, which are classified according to charge, strangeness (S), charm (C), bottom (B), and top (T). The quarks also fall into three generations. There are also six antiquarks.

Every interaction has its mediators: the photon for the electromagnetic force, two W's and a Z for the weak force, eight gluons for the strong force. The gluons themselves carry color, and therefore cannot exist as isolated particles.

Particles with half-integer spin are known as fermions. The leptons and the quarks are fermions. Particles with integer spin are known as bosons. The force mediators are bosons.

The standard Model is an $SU(3) \times SU(2) \times U(1)$ gauge theory, where color $SU(3)$ correspond to quantum chromodynamics (QCD), and the weak isospin and weak hyper charge group $SU(2) \times U(1)$ to the electro-weak theory.

1.2.1 Weak Interactions in the Standard Model

Neutrinos interact only through the weak interaction, mediated by the W^{+-} and Z bosons. Therefore, we concentrate the review on the electroweak portion of the Standard Model. The neutrino cross section in the Standard Model is described in the next chapter, section 2.1.

In 1960, Glashow, Weinberg and Salam introduced a model to unify the electromagnetic and weak forces. The electromagnetic and weak interactions are unified under $SU(2)\times U(1)$ gauge group. Experiments by Wu and Goldhaber [21] had already demonstrated the left-handedness of the neutrino, showing that the charged current weak interactions couple to particular chirality states. The following review is taken from [22].

The SU(2) group allows a natural implementation of this property because only the left-handed fermion field (and the right-handed anti-fermion fields) have a non trivial representation in the group. The left-handed states are arranged in doublets:

$$L_e = \begin{pmatrix} \nu_e \\ e^- \end{pmatrix}_L, \qquad L_\mu = \begin{pmatrix} \nu_\mu \\ \mu^- \end{pmatrix}_L, \qquad L_\tau = \begin{pmatrix} \nu_\tau \\ \tau^- \end{pmatrix}_L. \tag{1.2}$$

And the right-handed states do not couple to the $W^{\pm}$, they are expressed as SU(2) singlets:

$$l_e = e_R, \quad l_\mu = \mu_R, \quad l_\tau = \tau_R. \tag{1.3}$$

Similar assignments can be made in the quark sector

$$Q_u = \begin{pmatrix} u \\ d \end{pmatrix}_L, \qquad Q_c = \begin{pmatrix} c \\ s \end{pmatrix}_L, \qquad Q_t = \begin{pmatrix} t \\ b \end{pmatrix}_L, \tag{1.4}$$

$$u_u = u_R, \quad u_c = c_R, \quad u_t = t_R, \quad d_d = d_R, \quad d_s = s_R, \quad d_b = d_R \tag{1.5}$$

The model introduced by Glashow, Weinberg, and Salam to explain the electroweak forces is that of a spontaneously broken $SU(2) \times U(1)$ gauge theory. A generalized position dependent rotation in the space of $SU(2) \times U(1)$ of a field ϕ requires the existence of four vector fields, three (W^a_μ) corresponding to the original $SU(2)$ group and one (B_μ) from the $U(1)$ group. The covariant derivative of ϕ is given by

$$D_\mu\phi = (\partial_\mu - igW^a_\mu\tau_a - \frac{i}{2}g'B_\mu)\phi \tag{1.6}$$

where g and g' are the different coupling constants of the SU(2) and U(1) factors of the gauge group. And $\tau^a = \sigma^a/2$, where σ^a denotes the Pauli matrices.

To introduce massive gauge bosons, the symmetry has to spontaneously broken. The spontaneous symmetry breaking is used to give mass to the particles through the called Higgs

mechanism[23]. A scalar field H is introduced and assumed to acquire a vacuum expectation value of the form

$$< H >= \frac{1}{\sqrt{2}} \begin{pmatrix} 0 \\ v \end{pmatrix}. \tag{1.7}$$

The mass of the gauge fields will come from the interaction with this new scalar field. The relevant contribution to the electroweak Lagrangian will be the expectation value of the interaction of the scalar field ground state. Then the gauge boson mass terms come from the square of (1.6), evaluated at the scalar field vacuum expectation value $< H >$, equation (1.7)

$$\Delta L = \frac{1}{2}(0 \quad v)(gW_\mu^a \tau^a + \frac{1}{2}g' B_\mu)(gW^{b\mu}\tau^b + \frac{1}{2}g' B^\mu) \begin{pmatrix} 0 \\ v \end{pmatrix}. \tag{1.8}$$

Evaluating the matrix product explicitly and using the σ^a, we find

$$\Delta L = \frac{1}{2}\frac{v^2}{4}[g^2(W_\mu^1)^2 + g^2(W_\mu^2)^2 + (-gW_\mu^3 + g^{'}B_\mu)^2]. \tag{1.9}$$

Three massive vector bosons can be defined, the W_μ^+ as a function of W_μ^1 and W_μ^2 as follows

$$W_\mu^\pm = \frac{1}{\sqrt{2}}(W_\mu^1 \mp iW_\mu^2) \tag{1.10}$$

with mass $m_W = g\frac{v}{2}$.
The Z_μ^0 in function of W_μ^3 and B_μ

$$Z_\mu^0 = \frac{1}{\sqrt{g^2 + g'^2}}(gW_\mu^3 - g'B_\mu) \tag{1.11}$$

with mass $m_Z = \sqrt{g^2 + g'^2}\frac{v}{2}$, where v has been defined in equation 1.7.
The fourth vector field, orthogonal to Z_μ^0, remains massless:

$$A_\mu = \frac{1}{\sqrt{(g'W_\mu^3 + gB_\mu)}} \tag{1.12}$$

The A_μ field is identified with the electromagnetic vector potential.
Using the gauge fields $W_\mu^\pm$, Z_μ^0 and A_μ, the equation (1.9) can be written as follows

$$\Delta L = \frac{1}{2}\frac{v^2}{4}(g^2 W_\mu^+ W^{-\mu} + (g^2 + g'^2)Z_\mu^0 Z^{0\mu}, \tag{1.13}$$

where the mass for $m_{W^\pm}$ and m_{Z^0} are given by

$$\begin{aligned} m_{W^\pm} &= g\frac{v}{2}, \\ m_{Z^0} &= \frac{v}{2}\sqrt{g^2 + g'^2}. \end{aligned} \tag{1.14}$$

Now to complete the description of the electroweak interactions, consider a fermion field belonging to a general SU(2) representation, with U(1) charge Y. The covariant derivative, in terms of the mass eigenstate fields, becomes

$$\begin{aligned} D_\mu &= \partial_\mu - i\frac{g}{\sqrt{2}}(W_\mu^+ T^+ + W_\mu^- T^-) - i\frac{1}{\sqrt{g^2+g'^2}} Z_\mu (g^2 T^3 - g'^2 Y) \\ &- i\frac{gg'}{\sqrt{g^2+g'^2}} A_\mu (T^3 + Y), \end{aligned} \tag{1.15}$$

where $T^\pm = (T^1 \pm iT^2)$. In the spinor representation of SU(2), $T^\pm = \sigma^\pm$.
From the covariant derivative equation (1.15), we can identify the coefficient of the electromagnetic interaction as the electron charge e:

$$e = \frac{gg'}{\sqrt{g^2+g'^2}}, \tag{1.16}$$

and the electric charge quantum number as $Q = T^3 + Y$.
To further simplify equation (1.15), we introduce the weak mixing angle defined by

$$cos\theta_w = \frac{g}{\sqrt{g^2+g'^2}}, \quad sin\theta w = \frac{g'}{\sqrt{g^2+g'^2}}. \tag{1.17}$$

Using the Z^0 coupling $g^2 T^3 - g'^2 Y = (g^2+g'^2)T^3 = g'^2 Q$. The covariant derivative (1.15) can be written in the form

$$D_\mu = \partial_\mu - i\frac{g}{\sqrt{2}}(W_\mu^+ T^+ + W_\mu^- T^-) - i\frac{g}{cos\theta_w} Z_\mu (T^3 - sin^2\theta_w Q) - ieA_\mu Q, \tag{1.18}$$

where $g = e/sin\theta_w$.
The Lagragian for the weak interactions of quarks and leptons is given by:

$$\begin{aligned} L_{ew} &= \bar{L}_i (i\gamma^\mu)\partial_\mu L_i + \bar{l}_i (i\gamma^\mu) l_i + \bar{Q}_j (i\gamma^\mu \partial_\mu) Q_j + \bar{u}_j (i\gamma^\mu \partial_\mu) u_j + \bar{d}_k (i\gamma^\mu) d_k \\ &+ g(W_\mu^- J_W^{\mu+} + W_\mu^- J_W^{\mu-} + Z_\mu^0 J_Z^\mu) + eA_\mu J_{EM}^\mu, \end{aligned} \tag{1.19}$$

where

$$J_W^{\mu+} = \frac{1}{\sqrt{2}}(\bar{\nu_L}\gamma^\mu e_L + \bar{u}_L \gamma^\mu d_l); \tag{1.20}$$

$$J_W^{\mu-} = \frac{1}{\sqrt{2}}(\bar{e}_L \gamma^\mu \nu_L + \bar{d}_L \gamma^\mu u_L); \tag{1.21}$$

$$\begin{aligned} J_Z^\mu &= \frac{1}{cos\theta_w}[\bar{\nu}_L\gamma^\mu(\frac{1}{2}\nu_L + \bar{e}_L\gamma^\mu(-\frac{1}{2} + sin^2\theta_w)e_l + \bar{e}_R\gamma^\mu(sin^2\theta_w)e_R \\ &+ \bar{u}_L\gamma^\mu(\frac{1}{2} - \frac{2}{3}sin^2\theta_w)u_L + \bar{u}_R\gamma^\mu(-\frac{2}{3}sin^2\theta_w)u_R + \bar{d}_L\gamma^\mu(-\frac{1}{2} - \frac{1}{3}sin^2\theta_w)d_l \\ &+ \bar{d}_R\gamma^\mu(\frac{1}{3}sin^2\theta_w)d_R]; \end{aligned} \tag{1.22}$$

$$J_{EM}^\mu = -\bar{e}\gamma^\mu e + \frac{2}{3}\bar{u}\gamma^\mu u - \frac{1}{3}\bar{d}\gamma^\mu d. \tag{1.23}$$

The terms $W_\mu^- J_W^{\mu+} + W_\mu^- J_W^{\mu-}$ in equation 1.19 are responsible for all charged-current interactions in which the lepton charge is changed by ± 1 units, and W_μ^+ and W_μ^- represent, respectively, W^+ and W^- gauge bosons. The last two terms in equation 1.19 generates interactions mediated by the neutral gauge boson Z^0, and by the photon, denoted here by the gauge A_μ.

1.2.2 Neutrino Mass in the Standard Model

The standard model makes a prediction concerning the mass of neutrinos. A short review is given in this section.

A neutral fermion may exist either as a Dirac particle (fermion≠antifermion) or as a Majorana particle (fermion≡antifermion). The lagrangian can contain either Dirac mass terms or Majorana mass terms. A Dirac mass term for a neutrino ν can be written

$$L_{Dirac} = -m(\bar{\nu}_L \nu_R + \bar{\nu}_R \nu_L), \tag{1.24}$$

where m is the neutrino mass. In the Standard Model only the left handed helicity state of the neutrino ν_L is presented at each generation. Consequently the Standard Model does not contain any Dirac mass terms for neutrinos.

We can also construct mass terms out the ν_L alone or ν_R alone [24]. These mass terms are called Majorana mass terms. We can have the "left handed Majorana mass"

$$-L_{ML} = -\frac{m_L}{2}(\bar{\nu}_L)^C \nu_L + h.c., \tag{1.25}$$

or we can have the "right handed Majorana mass"

$$-L_{ML} = -\frac{m_R}{2}(\bar{\nu}_R)^C \nu_R + h.c.. \tag{1.26}$$

In these expressions, m_L and m_R are mass parameters, and for any field ψ, ψ^C is the corresponding charge-conjugate field. In terms of ψ, $\psi^C = C\bar{\psi}^T$, where C is the charge conjugation matrix, and T denotes transposition. ψ^C represents the antiparticle field ψ. In the Dirac bases $C = \gamma^2$ (up to an arbitrary phase). Note $(\nu_L)^C$ is a right-handed neutrino field and $(\nu_R)^C$ is a left-handed neutrino field.

A Dirac mass term turns a neutrino into a neutrino, or an antineutrino into an antineutrino, while a Majorana mass term converts a neutrino into an antineutrino, or vice versa. A Dirac mass terms conserve the lepton number L that distinguishes leptons from anti-leptons, while Majorana mass terms do not. The quantum number L is also conserved by the Standard Model coupling of neutrinos and other particles. Thus, if we assume that the interactions between neutrinos and other particles are well described by the Standard Model, then any L non-conservation that we observe in neutrino experiments would have to arise from Majorana mass terms, not from interactions.

An electrically charged fermion such as a quark cannot have a Majorana mass term, because such a term would convert it into an antiquark, in violation of electric charge conservation. However, for the electrically neutral neutrinos, Majorana mass terms are not only allowed but likely within the Standard Model, given that the neutrinos are now known to be particles with mass.

Chapter 2

Neutrino Cross Section

Neutrinos interact with matter via the weak interaction by exchanging W^+ or Z^0 bosons. Neutrino interactions can be classified into two main categories: the neutrino charged current interactions CC which involves the $W+/-$ and the neutral current NC processes with Z exchange:

$$\nu_\mu N \to \mu^- X \quad , \qquad \bar{\nu}_\mu N \to \mu^+ X \quad CC \tag{2.1}$$

$$\nu_\mu N \to \nu_\mu X \quad , \qquad \bar{\nu} N \to \bar{\nu} X \quad NC, \tag{2.2}$$

where $N = p, n$ or a target (with given neutrons and protons) and X as the hadronic final state.
Furthermore, the charged current and the neutral current interactions are each classified into three main categories

1. Quasielastic and elastic scattering: The neutrino scatters elastically off the nucleon ejecting a nucleon from the target. The quasi elastic is for charged current events and the elastic is for neutral current events.

2. Resonance production: The neutrino can excite the target nucleon to a resonance state. This resonance quickly decays usually into a nucleon and a single pion final state: $\nu_\mu N \to \mu^- N^*$, then the resonance $N*$ decays to $N* \to \pi N'$, where $N, N' = n, p$. This interaction occurs in both CC and NC processes.

3. Deep inelastic scattering: the neutrino scatter off a quark in the nucleon via the exchange of W and Z boson producing a lepton and a hadronic system in the final state. This interaction occurs in both charged and neutral current interactions.

Figure 2.1 shows the existing measurements of charged current neutrino cross sections across the entire energy range, including quasi elastic, resonance and deep inelastic interactions.

In addition, the theoretical models for each of the interactions are shown.

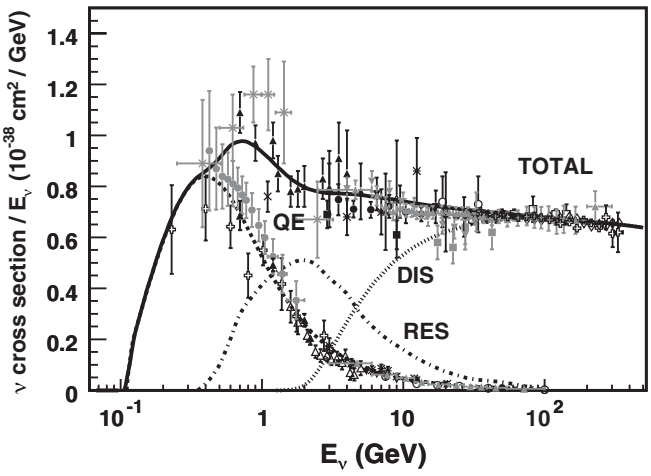

Figure 2.1: Total neutrino per nucleon charged current cross section divided by neutrino energy and plotted as a function of the energy. The Monte Carlo prediction is from the NUANCE generator. The experimental data are from the following experiments: ANL, PRD 16, 3103 (1977), BEBC, NP B343, 285 (1990), BNL, PRD 23, 2499 (1981), FNAL, PRD 28, 436 (1983) (D_2), GGM, NC A38, 260 (1977), MiniBooNE, PRD 81, 092005 (2010), C, NOMAD, EPJ C63, 355 (2009), Serpukhov, ZP A320, 625 (1985), Al, SKAT, ZP C45, 551 (1990), BEBC, ZP C2, 187 (1979), MINOS, PRD 81, 072002 (2010), NOMAD, PLB 660, 19 (2008), NuTeV, PRD 74, 012008 (2006). Also show are the predictions for the quasi-elastic (QE), resonance (RES), and deep inelastic (DIS) cross sections as well as the total cross section. This plot was taken from[8].

2.1 Neutrino Scattering

The general expression of the differential cross section for two body reaction to two body final states is

$$d\sigma = \frac{|\mathcal{M}|^2}{4[(p_1.p_2)^2 - m_1^2 m_2^2]^{1/2}} d\Phi_f, \tag{2.3}$$

where $\mathcal{M}$ is the transition amplitude: $< f|M|i >=< p_3, p_4|\mathcal{M}|p_1, p_2 >$ and $d\Phi_f$ stands for the phase space volume element in the final state

$$\int_{d\Gamma} d\Phi_f(p_3, p_4) = (2\pi)^4 \delta^4(p_3 + p_4 - p_1 - p_2) \frac{d^3p_3}{(2\pi)^2 2E_3} \frac{d^3p_4}{(2\pi)^3 2E_4}. \tag{2.4}$$

The $\mathcal{M}$ can be applied analytically for point like particles. For example, for a muon neutrino scattering off of an electron via W exchange $\nu_\mu + e^- \to \mu^- + \nu_e$. The review below is taken from [25]. The matrix element can be written as

$$\mathcal{M} = \frac{g_w^2}{8}[\bar{u}(p_3)\gamma^\mu(1-\gamma^5)u(p_1)]\frac{-i(g_{\nu\mu}-\frac{q_\mu q_\nu}{M_W^2})}{q^2-M_W^2}[\bar{u}(p_4)\gamma_\mu(1-\gamma^5)u(p_2)] \tag{2.5}$$

Considering $q^2 << M_W^2c^2$ the propagator can be simplified and averaging the spins the amplitude is written as

$$\begin{aligned}\sum_{spins}|\mathcal{M}|^2 &= \frac{g_w^2}{(8(M_Wc)^2)^2}Tr[\gamma^\mu(1-\gamma^5)(p_1+m_ec)\gamma^\nu(1-\gamma^5)p_3] \\ &\times \quad Tr[\gamma_\mu(1-\gamma^5)p_2\gamma_\nu(1-\gamma^5)(p_4+m_\mu c)].\end{aligned} \tag{2.6}$$

Using the trace theorems the amplitude is

$$\sum_{spins}|\mathcal{M}|^2 = 4(\frac{g_w}{M_Wc})^4(p_1.p_2)(p_3.p_4). \tag{2.7}$$

Neglecting the mass of the electron and if we go to the center of mass frame, the differential cross section is

$$\frac{d\sigma}{d\Omega} = \frac{1}{2}(\frac{\hbar c g_W^2 E}{4\pi(M_Wc^2)^2})^2[1-(\frac{m_\mu c^2}{2E})^2]^2. \tag{2.8}$$

As another example of the neutrino scattering, consider the neutrino nucleon scattering $\nu_\mu(p_1)+n(p_2)\rightarrow\mu^-(p_3)+\nu_e(p_4)$. The amplitude can be obtained replacing the point like $e-\nu_e$ current $\bar{u}(p_3)\gamma^\mu(1-\gamma^5)u(p_1)$ by the nucleon n-p current

$$\begin{aligned}V_{ud}<p(p_3)|V_\mu-A_\mu|n(p_1)> &= V_{ud}\bar{u}(p_3)\{\gamma_\mu f_1(q^2)+\frac{i\sigma_{\mu\nu}q^\nu}{2M}f_2(q^2) \\ &- \quad g_1(q^2)\gamma_\mu\gamma_5 - g_3(q^2)\frac{q_\mu}{M}\gamma_5\}u(p_1),\end{aligned} \tag{2.9}$$

where M is the nucleon mass and $q_\mu=(p_3-p_1)_\mu$. For the neutrino scattering off of a neutron, there is no analytical way to find the matrix amplitude $\mathcal{M}$. The nucleon form factors of V_μ are denoted by $f_{1,2}(q^2)$ which capture the internal structure of the nucleon and those of the A_μ by $g_{1.3}(q^2)$[26].

2.2 Quasielastic Scattering

This section reviews the quasi-elastic scattering process. The quasi-elastic cross section gives the information about the static properties of the proton and the neutron. Consider the neutrino nucleon scattering

$$\nu_l(p_1)+n(p_2) \quad\rightarrow\quad \mu^-(p_3)+p(p_4) \tag{2.10}$$

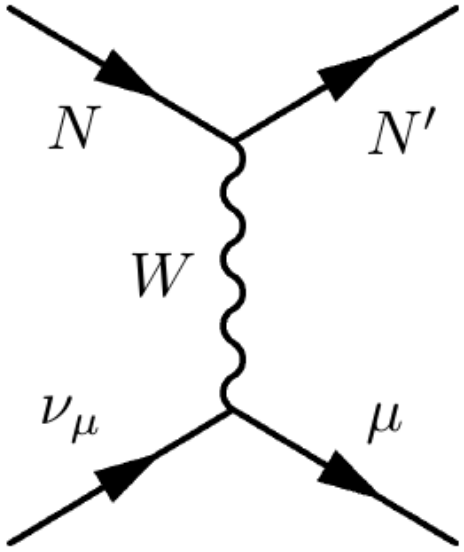

Figure 2.2: Feynman diagram for neutrino-nucleon charged current scattering.

where p_1, p_2, p_3 and p_4 are the four momenta. These four momenta are:

$$\begin{aligned} p_1 &= (E_\nu, \vec{p}_\nu) \\ p_2 &= (E_\mu, \vec{p}_\mu) \\ p_3 &= (M, 0) \\ p_4 &= (E, \vec{p}). \end{aligned} \tag{2.11}$$

The momenta can be written as a function of the Lorentz invariant variables s, t and u (called Mandelstam variables) as follow:

$$\begin{aligned} s &= (p_1 + p_2)^2 = (p_3 + p_4)^2 = M^2 + 2ME_\nu, \\ u &= (p_1 - p_4)^2 = (p_2 - p_3)^2 = M^2 + m^2 - 2ME_l, \\ t &= (p_1 - p_4)^2 = (p_2 - p_3)^2 = q^2 = 2M^2 + m^2 - (s + u) = 2M(E_l - E_\nu). \end{aligned} \tag{2.12}$$

Other set of kinematic variables are:

$$\begin{aligned} Q^2 &= -q^2 = 2E_\nu(E_l - p_l) - m^2 \\ \nu &= E_\nu - E_l, \\ W^2 &= M^2 + 2M\nu - Q^2, \\ x &= Q^2/2M\nu, \end{aligned} \tag{2.13}$$

where Q^2 is the four momentum transfer between the leptonic and hadron vertices and can be computed using the kinematics of the outgoing muon and incoming neutrino energy. The

E_ν is the neutrino, m is the mass of the muon, M is the nucleon mass, E_l and p_l are the energy and momentum of the lepton.

The neutrino interaction can be written as a leptonic current times a hadronic current. The hadronic current depends on the underlying nucleon structure and is written in terms of the Dirac and Pauli nucleon vector form factors. The amplitude is

$$\mathcal{M} = \frac{G}{\sqrt{2}}\bar{u}_\mu(p_3)\gamma_\lambda(1-\gamma_5)u_{\nu_\mu}(p_1)cos(\theta_c)\bar{u}_p(p_4)\Gamma^\lambda_{CC}(q^2)u_n(p_2). \tag{2.14}$$

Here θ_C is the Cabibbo angle which measures the probability of quark flavor change in the weak interactions[23]. $\Gamma^\mu_{CC}(q^2)$ gives the weak form factors for the nucleon

$$\Gamma_\lambda = \gamma_\lambda F_V^1(q^2)+\frac{i\sigma_{\lambda\nu}q^\nu\xi F_V^2(q^2)}{2M}+\frac{q_\lambda F_V^3(q^2)}{M}+\gamma_\lambda\gamma_5 F_A(q^2)+\frac{q_\lambda\gamma_5 F_p(q^2)}{M}+\frac{\gamma_5(p_1+p2)_\lambda F_A^3(q^2)}{M}, \tag{2.15}$$

here M is the mass of the struck nucleon. These weak form factors parameterize the amount of each type of weak current participating in the interaction. They are functions of the four momentum q^2.

The form factors in equation (2.15): F_V^1, F_V^2 and F_V^3 are the vector nucleon form factors, F_A is the axial-vector form factor, F_p is the pseudo scalar form factor and ξ is $\xi = \mu_p - \mu_n$, the difference of the anomalous magnetic moments of the proton and neutron.

The Γ_λ can be reduced using invariances following Llewellyn-Smith[28]. First, T invariance, requires that all form factors are real. Second, charge symmetry gives, $F_V^{1,2}, F_A$ and F_p real and $F_{V,A}^3$ imaginary. Third, T invariance plus charge symmetry implies no second class currents so $F_{V,A}^3 = 0$. Fourth, conserved vector current (CVC) requires $F_V^3 = 0$. And finally the Dirac electromagnetic isovector form factor $F_V^1(q^2) = [F_1^P(q^2) - F_1^n(q^2)]$ and the Pauli electromagnetic isovector form factor $F_V^2(q^2) = \frac{\mu_p F_2^p(q^2) - \mu_n F_2^n(q^2)}{\mu_p - \mu_n}$.

Using the matrix element 2.14 and the invariances from Llewellyn-Smith[28], the differential cross section for neutrino quasi elastic scattering can be written as

$$\frac{d\sigma}{dq^2} = \frac{G_F^2 M^2 \cos^2\theta_c}{8\pi E_\nu^2}[A(q^2) \mp B(q^2)\frac{(s-u)}{M^2} + \frac{(s-u)^2}{M^4}C(q^2)] \tag{2.16}$$

where G_F is the Fermi constant, s and u are the Mandelstam variables defined in equation (2.12). The $(-)+$ refers to (anti)neutrino scattering. $A(q^2), B(q^2)$, and $C(q^2)$ are:

$$\begin{aligned}
A(q^2) &= \frac{m^2-q^2}{4M^2}[(4-\frac{q^2}{M^2})|F_A|^2 - (4+\frac{q^2}{M^2})|F_V^1|^2 \\
&- \frac{q^2}{M^2}|\xi F_V^2|^2(1+\frac{q^2}{4M^2}) - \frac{4q^2F_V^1\xi F_V^2}{M^2} \\
&- \frac{m^2}{M^2}((F_V^1+\xi F_V^2)^2 + |F_A|^2], \\
B(q^2) &= \frac{q^2}{M^2}((F_V^1+\xi F_V^2)^2)F_A), \\
C(q^2) &= \frac{1}{4}(|F_A|^2 + |F_V^1|^2 - \frac{q^2}{4M^2}|\xi F_V^2|^2).
\end{aligned} \tag{2.17}$$

$F_V^1(q^2)$ and $F_V^2(q^2)$ are the Dirac electromagnetic isovector form factor and the Pauli electromagnetic isovector form factor. And the $\xi = \mu_p - \mu_n = 3.71$ (μ = anomalous magnetic moment).

The F_V^1 and F_V^2 can be written as a function of the Sachs from factors:

$$\begin{aligned} F_V^1(q^2) &= (1 - \frac{q^2}{4M^2})^{-1}[G_E^V(q^2) - \frac{q^2}{4M^2}G_M^V(q^2)] \\ \xi F_V^2(q^2) &= (1 - \frac{q^2}{4M^2})^{-1}[G_M^V(q^2) - G_E^V(q^2)]. \end{aligned} \tag{2.18}$$

The Sachs form factors have been well measured in electron scattering experiments [29]. The G_M^V, G_E^V are described to within $\pm 10\%$ experimentally by:

$$\begin{aligned} G_E^V(q^2) &= \frac{1}{(1 - \frac{q^2}{0.71GeV^2})^2} \\ G_M^V(q^2) &= \frac{1 + \mu_p - \mu_n}{(1 - \frac{q^2}{0.71GeV^2})^2}. \end{aligned} \tag{2.19}$$

The cross section equation 2.16 also depends on the axial vector from factor $F_A(q^2)$. This axial-vector form factor can be written using a dipole approximation as follows

$$F_A(q^2) = \frac{F_A(0)}{(1 - \frac{q^2}{(M_A)^2})^2} \tag{2.20}$$

where M_A is the axial vector mass. F_A at $(q^2 = 0)$ has been measured in neutron β decay experiments. The q^2 dependance of the axial form factor is extracted from the neutrino-nucleon quasi elastic data. This is equivalent to measuring M_A.

The differential cross section for charged current quasi elastic (CC QE) interactions depends on the value of axial vector mass M_A. Figure 2.3 shows the differential cross section for CC QE interactions as a function of Q^2 for mono energetic neutrinos scattering off free nucleons using different values of M_A, for $M_A = 1.0$ GeV, $M_A = 1.1$ GeV and $M_A = 1.2$ GeV. The left plot shows the curves normalized by area and shows that changing the value of M_A has an effect on the shape of the cross section. The right plot shows the curves absolutely normalized and shows that changes to M_A also changes the overall normalization of the cross section.

Measurements of the axial vector mass M_A have been made by several experiments, the next section provides a review of some experimental results.

The changes of M_A can affect the shape and rate information as is shown in figure 2.3. Some experiments present results for M_A using only rate information, only shape information or both. Those depending only on a rate analysis require a good knowledge of the flux. Many of these experiments did not have sufficient knowledge of the incident neutrino flux to use the rate information.

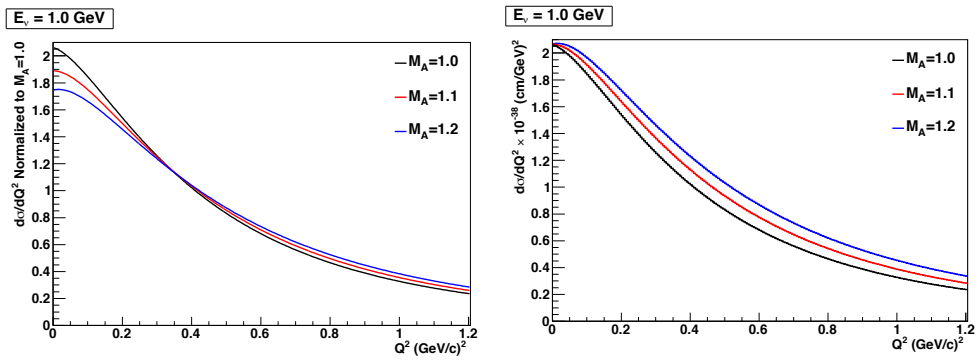

Figure 2.3: Cross section for different values of M_A. The curves correspond to mono-energetic neutrinos (at 1GeV) and do not include any nuclear effects. The left curves are normalized to area and the right curves are absolutely normalized. Plots taken from [30]

2.2.1 Nuclear Effects

Section 2.2 reviewed neutrino nucleon scattering from a nucleon $\nu_\mu n \rightarrow \mu^- p$. However, neutrino experiments use nuclear target. For example, NOνA uses mainly (CH_2) as a target. Because the target nucleons are bound in (CH_2), there are additional complications due to interactions with the other nucleons within the nucleus called nuclear effects. The following review of nuclear effects is taken from [30].

Nuclear effects change both the cross section and the kinematics of the final state. For example when a charged current pion is made and the pion is absorbed in the target nucleus the visible final state is different from the original interaction.

The nuclear effects include the Fermi motion of the nucleons (the movement of the nucleon inside the target nucleus), a nucleon's binding energy in the nucleus, Pauli blocking and final state interactions (FSI) such as re-scattering of the outgoing particles with the nuclear remnant.

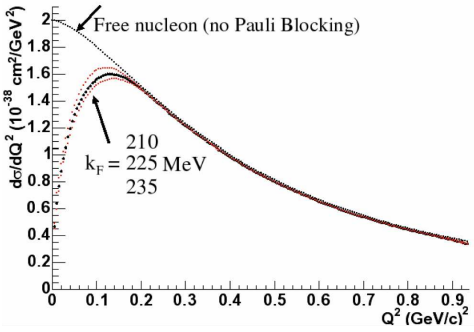

Figure 2.4: Charge current QE differential cross section as a function of Q^2 for several values of Fermi momentum k_F compared to the free nucleon. Plot taken from [30] .

Pauli blocking is a consequence of the application of the Pauli Exclusion Principle to

the nucleus in which two identical fermions cannot occupy the same quantum state. In the quasi elastic interactions this means that the struck nucleus can only be excited if there is an unoccupied final energy state for the outgoing nucleon. Recent experiments have used the relativistic Fermi Gas model (RFG) to describe the effects of both Pauli-blocking, and Fermi motion for quasi elastic scattering. In the RFG model, the excitation of the nuclear system is described as the transition of a nucleon from a state below the Fermi surface to one above the Fermi surface [30]. In the FG model the nucleus is a translationally invariant system composed of an infinite number of nucleons with a momentum distribution

$$n(|\vec{p}|) = \frac{\tau}{\frac{4}{3}\pi k_F^3}\Theta(k_F - |\vec{p}|), \tag{2.21}$$

where τ is the atomic number Z for protons or the neutron number N, Θ is the Heaviside step function, k_F is the Fermi momentum; and $\vec{p}$ is the three momentum of the nucleon. The value of the Fermi momentum depends on the nucleus and is typically around 200-300 MeV. In Fermi Gas simulations all energy levels up to the Fermi surface are considered to be filled and any interaction with a momentum transfer that leaves the final state nucleon with a momentum less than the Fermi momentum is considered to be Pauli blocked.

In 1972 Smith and Moniz [31] evaluated quasi elastic neutrino nucleus scattering, comparing this with quasi elastic neutrino nucleon scattering and found the largest effect is for low values of Q^2. Figure 2.4 shows the effect on the cross section σ of moving from a free nucleon approach to Free Gas model. The figure shows three different values of the Fermi momentum.

2.3 Review of Quasi-elastic cross section measurements

This section presents a review of the experiments that have measured the axial vector mass and the cross section. Table 2.1 is a survey of axial vector mass M_A measurements, indicating the target used, the type of detector, the axial vector mass M_A obtained and the number of events.

2.3.1 Result from Bubble Chamber experiments

In 1982 the axial mass was measured by the Argonne 12-foot bubble chamber [32]. This experiment studied a muon neutrino beam interacting with deuterium. The reaction studied was $\nu_\mu d \to \mu^- pp_s$. The experiment used a 12.4 GeV proton beam extracted from the Zero Gradient Synchrotron and focused onto a beryllium target. Charged particles (pions and kaons) are produced from this interaction and focused toward the bubble chamber by two

Table 2.1: Review of the Ma axial vector measurements.

Experiment	Target	Detector	Ma±Error (GeV)	Events
ANL[32]	D	Bubble chamber	1.00 ± 0.05	1,737
FNAL[112]	D	Bubble chamber	1.05+0.12-0.16	362
BNL[35]	D	Bubble chamber	1.08+0.040-0.045	1,1381
CERN[36]	CF_3Br, C_3H_8	Bubble chamber	0.94 ± 0.05	766
SKAT[37]	CF_3B_r	Bubble chamber	1.05 ± 0.14	540
BNL[38]	F_e	Segmented tracker	1.05 ± 0.20	6000
K2K[39]	H_2O	Segmented tracker	1.20 ± 0.12	5,568
MiniBooNE[40]	CH_2	Chrenkov detector	1.35 ± 0.17	146,070
NOMAD[41]	C	Segmented tracker	$1.05 \pm 0.02 \pm 0.06$	14,021
MINOS[40]	Fe	Segmented tracker	1.26 ± 0.17	345,000

magnetic horns. Neutrinos come from the decay of the pions and kaons in the 30-m long drift space upstream of the bubble chamber.

The neutrino flux was calculated using the measured yields of pions in the p-Be collision and propagating the particles through the horn system and the decay tunnel. The flux uncertainty was estimated as 15% from the pions and 25% from the kaons.

The event selection for the data sample was done through human scanning. The overall efficiency for events in fiducial volume was $(98 \pm 2)\%$. They reported a total of 2.4×10^6 pictures taken with the 12-foot bubble chamber. The sample contained 1737 events and the background for the quasi elastic interactions was estimated to be $(2 \pm 2)\%$.

Figure 2.5 shows the weighted number of events as function of Q^2, where the solid line is obtained from a maximum-likelihood fit of the data to the dipole model. The axial vector mass result for this experiment was $M_A = 1.00 \pm 0.05$ GeV.

The table 2.1 shows the result from several bubble chamber experiments using different targets. The axial mass world average value is $M_A = 1.026 \pm 0.021$ GeV [33].

2.3.2 Result from the K2K experiment

In 2006, the K2K experiment measured the axial vector mass using neutrino interactions on oxygen[39]. This experiment used a neutrino beam produced by 12 GeV protons hitting an aluminum target. Two magnetic horns focus the charged particles (pions and kaons) into a 200 m long decay pipe, where they decayed to produce the neutrino beam. The neutrino energy was peak at 1.2 GeV with energies from 0.3 GeV to 5 GeV.

The K2K experiment analyzed one-track and two-track events. The requirement for the recoil proton of the two-track sample was a threshold of 600 MeV proton momentum. The purity of the sample was 63%.

K2K did not include the low Q^2 bins in the fit, events below 0.2 GeV^2, since, the largest

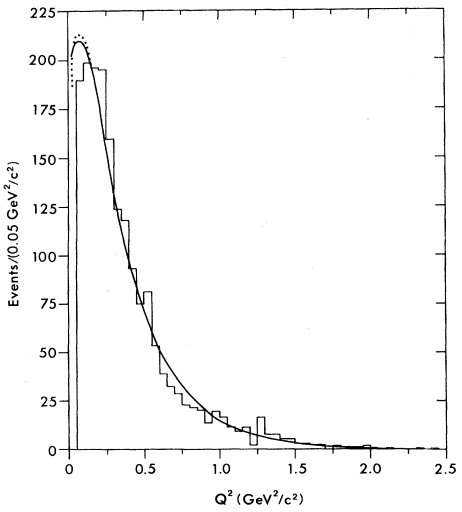

Figure 2.5: Q^2 distribution from the ANL experiment[32], the solid histogram is the data and the lines are the result from the fit. The solid curve is the maximum-likehood fit to the dipole model ($M_A = 1.00\ GeV/c^2$). The dotted curve is from a fit to AVMD model ($M_A = 1.11\ GeV/c^2$).

uncertainty of the model for nuclear effects is the low Q^2 region. They also used a free parameter for the overall normalization and rescaled the neutrino in each energy region. The figure 2.6 shows the data and the best fit Q^2 distribution for the one-track, two track QE enhanced, and the two-track non-QE enhanced samples.

K2K found, from a fit to the shape of the Q^2 distribution, $Ma = 1.20 \pm 0.12$ GeV.

2.3.3 Result from the NOMAD experiment

The NOMAD experiment studied the neutrino and antineutrino quasi-elastic cross section. The axial vector mass parameter M_A for the quasi-elastic neutrino cross section was extracted from their cross section measurement.

This experiment used a neutrino beam produced by the 450 GeV proton synchrotron at CERN. The proton beam interact with a beryllium target producing π^+ and K^+ mesons. Those charged particles are focused by magnetic lenses and subsequently decay producing neutrinos [41].

The NOMAD experiment consists of an active target of 44 drift chambers made of low Z material with a total fiducial mass of 2.7 tons located in a 0.4 Tesla dipole magnetic field. The average energy of the incoming neutrinos is 25.9 GeV. The data sample used by the CCQE analysis was 751000 charged current interactions.

The NOMAD used two samples for the analysis of quasi-elastic charged current interactions. In the first sample of 1-track events, only one charged lepton was reconstructed

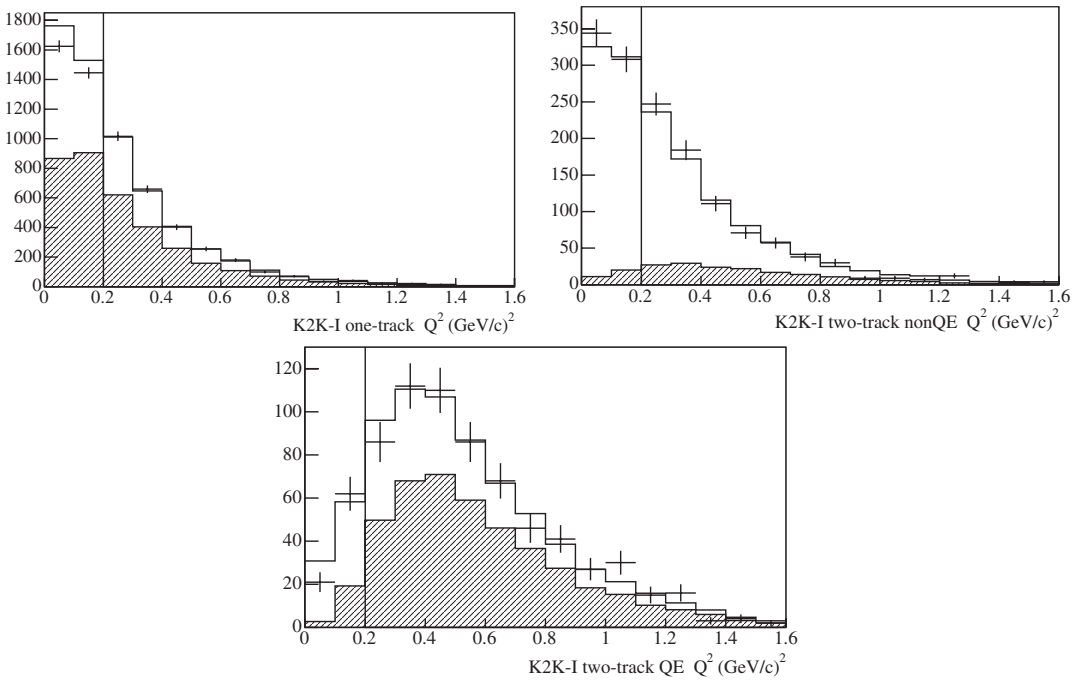

Figure 2.6: Q^2 distribution for data and the best fit for a set of the K2K data. The points are the data and the solid histogram is their MC simulation for signal plus background. The first graph is the one-track sample, the second the two-track non QE sample and the third the two-track QE enhanced sample. The shaded region is their MC prediction for the QE interactions[24].

and identified and in the second sample 2-track events, the negative muon and a positively charged track were reconstructed. For the second track proton candidate, they required to have a momentum of $p > 300$ MeV/c. The figure 2.7 shows the reconstructed Q^2 distribution for data and their MC. This plot also shows the expected background contamination. NOMAD used the DIS interactions to constraint the flux normalization.

The cross section and axial mass M_A extracted from the combined of 1-track and 2-track sample is

$$\begin{aligned} < \sigma_{qel} >_{\nu_\mu} &= (0.92 \pm 0.02(stat) \pm 0.06(syst)) \times 10^{-38} cm^2 \\ M_A &= 1.05 \pm 0.02(stat) \pm 0.06(syst) GeV. \end{aligned} \tag{2.22}$$

The figure 2.8 shows the $< \sigma_{qel} >_{\nu_\mu}$ as a function of the neutrino energy in the 1-track and 2-tracks samples.

2.3.4 Result from the MiniBooNE experiment

In 2010, the MiniBooNE experiment made the first measurement of the double differential cross section for charged current quasi elastic (CCQE) scattering on carbon [40]. This

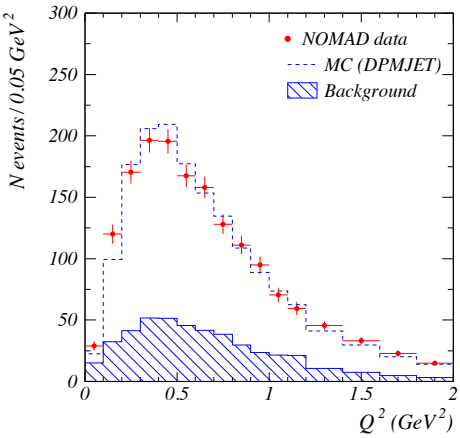

Figure 2.7: Q2 distribution for the selected CCQE events [41].

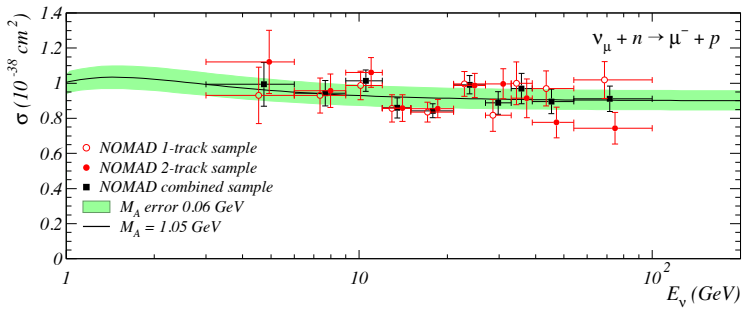

Figure 2.8: Cross section as a function of the neutrino energy for the 1-track and 2 track subsamples [41].

section presents a review of their results. The MiniBooNE experiment uses a neutrino beam from the Fermilab Booster. Protons are accelerated to 8 GeV kinetic energy in the Fermilab Booster synchrotron, are extracted, and interact with a beryllium target. The secondary mesons that are produced are then focused by a toroidal magnetic field which serves to direct the resulting beam of neutrinos towards the downstream detector. The MiniBooNE detector consists of a spherical steel tank of 610 cm inner radius filled with mineral oil (CH_2).

The procedure to determine the cross section was made selecting a CCQE sample and measuring the $CC\pi^+$ background. The $CC\pi^+$ background to the CCQE signal is measured by adjusting the weights of the simulated $CC\pi^+$ events to achieve data-MC agreement in the Q^2 distribution for the background sample ($CC\pi^+$). This weighting is applied to the simulated $CC1\pi^+$ events, giving an estimate of the $CC1\pi^+$ background to the CCQE signal. Figure 2.9 shows the Data and MC for the selected samples after background correction, on the top a sample dominated by CCQE interactions and on the bottom a background sample dominated by $CC1\pi^+$.

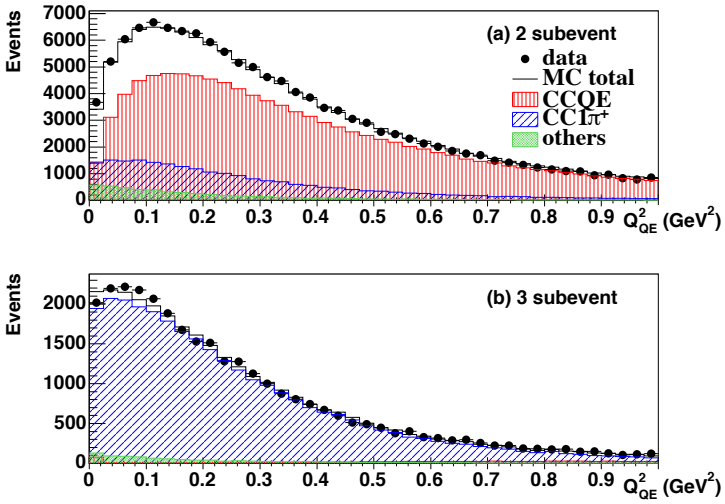

Figure 2.9: Q^2 distribution for two sets of data after the $CC1\pi^+$ background constraint. The points are the data and the black histogram is the result from the fit. The top plot is the quasi elastic sample and the bottom plot is the background sample[40]

The MiniBooNE experiment used a set of data corresponding to $5.58 \times 10^{20} POT$ with a total of 146070 events passing the CCQE selection. The CCQE sample is estimated to contain 23.0% of background events dominated by $CC1\pi^+$ interactions.

The results are shown in figures 2.10. The left hand plot shows the flux integrated differential cross section and the right hand plot is the flux integrated single differential cross section.

MiniBooNE experiment measured the flux integrated CCQE cross section by integrating the double differential cross section providing the value of $9.429 \times 10^{-39} cm^2$ with 10.7% on the total normalization error.

In addition the MiniBooNE experiment performed a shape only fit for the single differential cross section. The right hand plot in figure 2.10 shows the RFG model for the world average ($M_A = 1.03 GeV, k = 1.000$) [40] and the parameters from their fit ($M_A = 1.35 GeV, k = 1.007$).

The flux unfolded CCQE cross section as a function of the neutrino energy was measured by the MiniBooNE experiment. This is shown in figure 2.11. The extracted parameters from their fit are: ($M_A^{eff} = 1.35 GeV, k = 1.007$).

We have reviewed measurements for the axial vector mass M_A from modern experiments using different targets and old bubble chamber experiment using deuteron as target. Those experiments provide the current knowledge for the axial vector mass M_A. In addition to these experiments, other experiments are analyzing their data using different targets such as the MINOS experiment which uses (Fe) as target and the Minerva experiment which

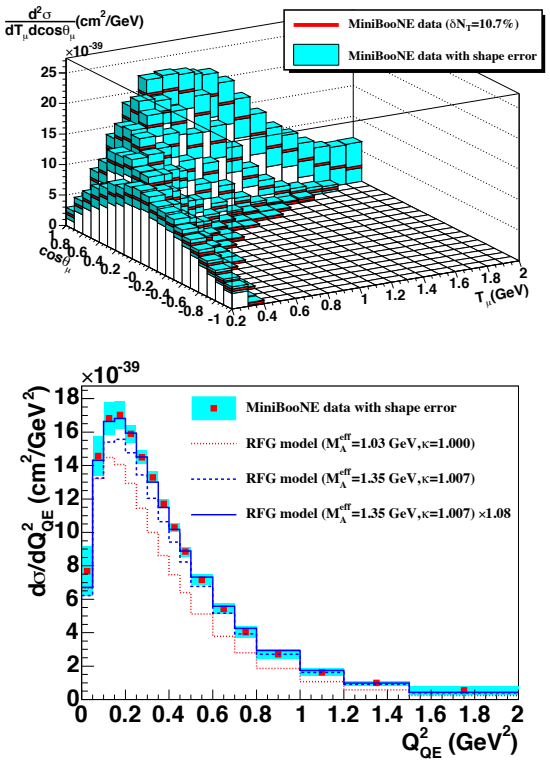

Figure 2.10: Top: Flux integrated double differential cross section per target neutron for the ν_μ CCQE interactions. Bottom: Flux integrated single differential cross section per target neutron for the ν_μ CCQE interactions [40].

uses several different nuclear targets (C,Fe,Pb)[43].

The MINOS experiment reported preliminary results for the axial vector M_A, measuring M_A for two regions of Q^2, $(1.26^{+0.12}_{-0.10}(fit)^{+0.08}_{-0.12}(syst)$ GeV between 0.3 and 1.2 GeV^2 and $(1.19^{+0.09}_{-0.10}(fit)^{+0.12}_{-0.14}(syst)$ for Q^2 between 0 and 1.2 GeV^2 [42].

The K2K, NOMAD, MiniBooNE and MINOS experiments reported a higher axial vector mass than the values reported by the Bubble chamber experiment (Table 2.1). In addition, the NOMAD and MiniBooNE experiments reported measurements of cross section as a function of the neutrino energy which seem to disagree. Figure 2.12 shows the result from both experiments. This plot also shows the MC predictions for different models, the dash red curve is the RFG model with $M_A = 1.03$ GeV and $k = 1.00$, the blue curve the RFG model with $M_A = 1.35$ GeV and $k = 1.007$ and the dash green the Free nucleon model with $M_A = 1.03$ GeV. None of those models describe the experimental data for both experiments. It is important to understand that the MiniBooNE experiment quasi elastic selection did not use the information about the recoil proton in the final state, while NOMAD experiment identified the recoil proton for the 2-track sample for the selected quasi elastic interactions.

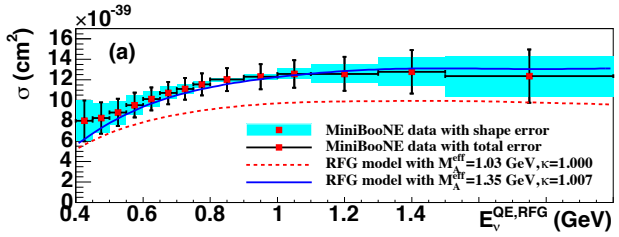

Figure 2.11: Cross section per neutrino as a function of the neutrino energy [40].

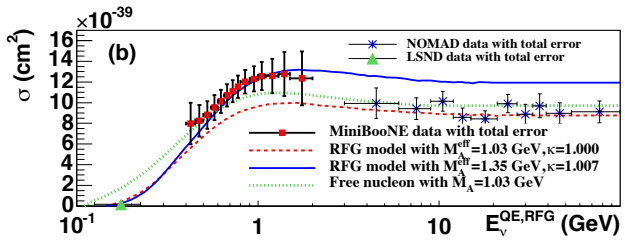

Figure 2.12: Quasielastic cross section measurement as a function of neutrino energy for MiniBooNE experiment and NOMAD experiment [40].

Recently, theorists have been comparing the this data to different models using an interesting new approach that matches the data from MiniBooNE, the multi nucleon model by M. Martini et al., [44]. This model considers the neutrino interacting with multiple nucleons at once. They consider events involving a correlated nucleon pair from which the partner nucleon is also ejected. This leads to the excitations of 2 particle 2 hole (2p-2h) states. Their prediction for the 2p-2h in C is shown in figure 2.13. The plot shows the dash curve the Fermi Fas model ($M_A = 1.0$ GeV), the red curve the 2p-2h and the points are the data from MiniBooNE experiment. This model does not remedy the discrepancies between MiniBooNE data and NOMAD.

2.4 Brief review of Resonance and Deep inelastic scattering

This section presents a brief review of the resonance scattering and deep inelastic scattering.

2.4.1 Resonance scattering

Neutrinos interact with a nucleon and excite that nucleon into a resonant state which subsequently decays producing a pion. Typical resonances reactions, in which intermediate states like $\Delta(1232)$ are produced for charged current interactions are

$$\nu_\mu p \to \mu^- p\pi^+, \quad \nu_\mu n \to \mu^- n\pi^+, \quad \nu_\mu n \to \mu^- p\pi^0 \tag{2.23}$$

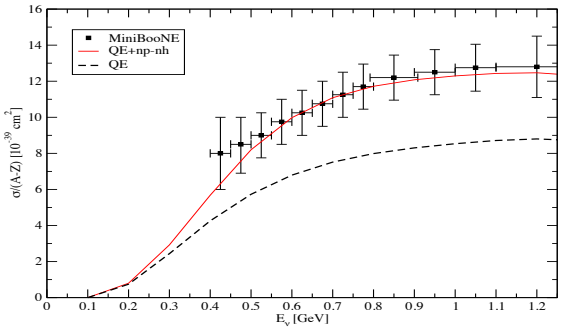

Figure 2.13: Quasi elastic $\nu_\mu C$ cross section per neutron as a function of neutrino energy. The dashed curve the pure quasi elastic cross section, the solid curve the 2p-2h model and the points the data from MiniBooNE [44].

and for neutral current

$$\nu_\mu p \to \nu_\mu p \pi^0 \quad \nu_\mu p \to \nu_\mu n \pi^+ \quad \nu_\mu n \to \nu_\mu n \to \nu \mu n \pi^0, \quad \nu_\mu n \to \nu_\mu p \pi^-. \tag{2.24}$$

The model used for resonant pion production is the Rein-Sehgal model [45]. This model predicts both CC and NC resonance production.

The differential cross section for resonance scattering using the phase space factors can be written as

$$\frac{\partial \sigma}{\partial q^2 \partial E_q} = \frac{G_F^2 cos^2\theta_c}{8\pi^2} \frac{q^2}{Q^2} \frac{\Gamma}{(W - M_\Delta)^2 + \frac{\Gamma^2}{4}} (u^2 \sigma_- + v^2 \sigma_+ + 2uv\sigma_0), \tag{2.25}$$

where $\frac{\Gamma}{(W-M_\Delta)^2+\frac{\Gamma^2}{4}}$ is the Breit-Wigner factor and W is the invariant mass of the resonance, Γ is the width of the resonance and $\sigma_\pm$, σ_0 are

$$\sigma_\pm = \frac{m_\Delta}{m_N} \frac{1}{2} \sum_{j_z} f^2_{\pm, j_z} \tag{2.26}$$

$$\sigma_0 = -\frac{m_N}{m_\Delta} \frac{Q^2}{q^2} \sigma_{j_z} f^2_{0, j_z} \tag{2.27}$$

$$f_{k,j_z} = < N, j_z + k | F_k | \Delta, j_z > . \tag{2.28}$$

Equation 2.25 gives the differential cross section for a single resonance (Δ). However, a number of other resonances contribute to pion production and these resonances and their interference have to be taken into account.

The Rein-Sehgal model shows some disagreement with the pion production data, especially for the low Q^2. To improve the agreement between model and data some modifications to the Rein-Sehgal model have been proposed. In the original Rein-Sehgal calculation, the mass of the muon was approximated as zero. Extensions of the model to include muon mass have been described [46]. A compilation of measurements and MC simulation of CC and NC single pion production cross section is found in [8].

2.4.2 Deep Inelastic scattering

In deep inelastic scattering, the neutrino interacts with a quark in the nucleon and produces a lepton and a hadronic system. Studies of deep inelastic scattering have provided measures of electroweak parameters and nucleon structure functions coupling constants.
The deep inelastic scattering can be described in terms of the four momentum transfer, the inelasticity and the Bjorken scaling parameters given by

$$x = \frac{Q^2}{2M\nu}, \tag{2.29}$$

$$y = \frac{E_{had}}{E_\nu}, \tag{2.30}$$

$$Q^2 = -m_\mu^2 + 2E_\nu(E_\mu - p_\mu cos\theta_\mu), \tag{2.31}$$

where E_ν is the incident neutrino energy, $\nu = E_{had}/E_\nu$ is the energy of the hadronic system, E_μ the energy of the muon and $cos\theta_\mu$ is the scattering angle of the outgoing muon.
The inclusive cross section for deep inelastic scattering neutrinos can be written using these variables and structure functions which contain the information about the structure of the target

$$\frac{d^2\sigma^\nu}{dxdy} = \frac{G_F^2 M E_\nu}{\pi(1+Q^2/M_{W,Z}^2)^2}[\frac{y^2}{2}2xF_1(x,Q^2) + (1-y-\frac{Mxy}{2E})F_2(x,Q^2) + y(1-\frac{y}{2})xF_3(x,Q^2)], \tag{2.32}$$

where $F_i(x,Q^2)$ are the dimensionless nucleon structure functions. There is an approximate simplification using massless, free spin 1/2 partons, first derived by Callan and Gross, where $2xF_1 = F_2$.
Using the quark parton model this structure function can be written in terms of the quark composition of the target:

$$2xF_1^{\nu p,CC} = x[d_p(x) + \bar{u}_p(x) + s_p(x) + \bar{c}_p(x)], \tag{2.33}$$

$$xF_3^{\nu p,CC} = x[d_p(x) - \bar{u}_p(x) + s_p(x) - \bar{c}(x)], \tag{2.34}$$

where $d_p(x)$ refers to the parton distribution function (PDF), of a given quark flavor in the proton and the contributions from the third generation quarks are neglected. A compilation of the experimental measurements and simulation for the deep inelastic neutrino cross sections are found in [8].

The cross sections are very important for the study neutrino interactions, specifically in neutrino oscillations measurements. Neutrino oscillation experiment uses the quasi-elastic sample as signal sample for the analysis of the appearance and disappearance measurements.

2.5 Brief review of theoretical formulation for neutrino oscillations

Results from studies of neutrino oscillations have provided evidence that neutrinos have mass. This section reviews the theoretical formulation for neutrino oscillation.

Neutrino oscillation is a phenomenon that occurs when a neutrino from one type changes to another type as the neutrino propagates. The theory of neutrino oscillation states that neutrino mass eigenstates are not necessary the same as the flavor eigenstates [11]. A relationship between these eigenstates can be shown as

$$|\nu_\alpha >= \sum_{i=1}^{N} U^*_{\alpha i}|\nu_i > \tag{2.35}$$

where α is the index for each type of flavor eigenstates, corresponding to the electron neutrino $|\nu_e >$, muon neutrino $|\nu_\mu >$, and tau neutrino $|\nu_\tau >$. On the right hand side of equation (2.35), the i corresponds to the mass eigenstates, $|\nu_1 >, |\nu_2 >$; and $|\nu_3 >$, and U is the NxN unitary matrix also known as Pontecorvo-Maki-Nakagawa-Sakata(PMNS) mixing matrix[11].

To obtain the probability for a ν_α neutrino to be converted into ν_β at any time $t > 0$, we need the time evolution of the neutrino. A neutrino of the generation i, after a time interval of t, is given by

$$|\nu_i(t) >= e^{-E_i t}|\nu_i >, \tag{2.36}$$

where the energy $E_i = \sqrt{P^2 + m_i^2}$. The time evolution of a flavor eigenstate $|\nu_\alpha >$ can be written by substituting equation (2.36) into equation (2.35)

$$|\nu_\alpha(t) >= \sum_{i=1}^{N} U^*_{\alpha i}|\nu_i(t) >= \sum_{i=1}^{N}\sum_{\beta=1}^{N} U_{\beta i}U^*_{\alpha i}e^{-iE_i t}|\nu_\beta > . \tag{2.37}$$

The probability that a neutrino created as a ν_α eigenstate will be detected as a ν_β after a time t is

$$\begin{aligned} P(\nu_{\alpha\to\beta}) &= |<\nu_\beta|\nu_\alpha(t)>|^2 \\ &= |\sum_{i=1}^{N} U_{\beta i}U^*_{\alpha i}e^{-iE_i t}|^2 = \sum_{i=1}^{N}\sum_{j=1}^{N} U^*_{\alpha i}U_{\alpha j}U_{\beta i}U^*_{\beta j}e^{-it(E_i-E_j)}. \end{aligned} \tag{2.38}$$

For relativistic neutrinos, the momentum $|p_i| = |p| \approx E$ and the energy $E_i \approx E_i + m_i^2/2E$, since $m_j << |p_j|$. Neutrinos travel a distance L in a time t, with $c = 1$, the distance $L = t$. The probability result is then

$$P(\nu_{\alpha\to\beta})(t) = \sum_{i=1}^{N}\sum_{j=1}^{N} U^*_{\alpha i}U_{\alpha j}U_{\beta i}U^*_{\beta j}e^{-i\frac{L}{2p}\Delta m^2_{ij}}, \tag{2.39}$$

where $\Delta m^2_{ij} = m^2_i - m^2_j$. For any unitary matrix $\sum_i U_{\beta i} U^*_{\alpha i} = \delta_{\alpha\beta}$. Adding and subtracting this term to the last expression, the probability can be written as

$$\begin{aligned} P(\nu_{\alpha\to\beta}) &= \sum_{ij} U_{\beta i} U *_{\alpha i} U *_{\beta j} U_{\alpha j} (e^{-i\frac{L}{2p}\Delta m^2_{ij}-1}) + \sum_{ij} U_{\beta i} U *_{\alpha i} U *_{\beta j} U_{\alpha j} \\ &= \delta_{\alpha\beta} - 4\sum_{i>j} Re(U^*_{\alpha i} U_{\alpha j} U_{\beta i} U^*_{\beta j}) sin^2(\frac{\Delta m^2_{ij} L}{4E}) \\ &+ 2\sum_{i>j} Im(U^*_{\alpha i} U_{\alpha j} U_{\beta i} U^*_{\beta j}) sin^2(\frac{\Delta m^2_{ij} L}{4E}). \end{aligned} \tag{2.40}$$

This is the probability that a neutrino that starts as ν_α eigenstate after it travels a distance L is detected as a ν_β. We can see from the probability equation (2.40) if the neutrino masses are equal to zero oscillations do not occur.

2.5.1 Two flavor approximation

The study of neutrino oscillation can be described with the two flavor approximation. From the relation of the mass eigenstates and flavor eigenstates equation (2.35), the ν_μ and ν_e flavor eigenstates are related to the mass eigenstates ν_1 and ν_2 as follows

$$|\nu_\mu> = \cos\theta|\nu_1> + \sin\theta|\nu_2>, \tag{2.41}$$

$$|\nu_e> = -\sin\theta|\nu_1> + \cos\theta|\nu_2> . \tag{2.42}$$

The time evolution of the weak eigenstate $|\nu_\mu>$ is

$$|\nu_\mu> = cos\theta e^{-E_1 t}|\nu_1> + sin\theta e^{-E_2 t}|\nu_2> . \tag{2.43}$$

The probablity of a muon neutrino transforming into a electron neutrino is

$$\begin{aligned} P(\nu_\mu \to \nu_e) &= |<\nu_\mu|\nu_e>|^2 \\ &= sin^2\theta cos^2\theta |e^{-iE_2} - e^{-iE_1}|^2 = sin^2 2\theta sin(\frac{(E_2 - E_1)t}{2}), \end{aligned} \tag{2.44}$$

where $E_1 \approx p + \frac{m_1^2}{2p}$ and $E_2 \approx p + \frac{m_2^2}{2p}$. And again considering that a muon neutrino travels a distance L in a time t, $L = t$. Substituting the energies into the last expression, the probablity is

$$P(\nu_\mu \to \nu_e) = sin^2 2\theta sin^2(\frac{(m_1^2 - m_2^2)L}{4E}) \tag{2.45}$$

where L is the distance from the source, E is the neutrino energy, and $\Delta m^2 = m_1^2 - m_2^2$ is the mass differences. Returning the constants c and h, the phase $\frac{\Delta m^2 c^3 L}{4hE} \approx 1.267 * \frac{\Delta m^2}{eV^2}\frac{L}{km}\frac{GeV}{E}$.

2.5.2 Three neutrino mixing

Considering three generations of neutrinos, in the neutrino oscillations formulation, the flavor eigenstates are related with mass eigenstates through the PMNS matrix. Writing the equation 2.36 for the three neutrino flavor in matrix form, we have

$$\begin{pmatrix} \nu_e \\ \nu_\mu \\ \nu_\tau \end{pmatrix} = \begin{pmatrix} U_{e1} & U_{e2} & U_{e3} \\ U_{\mu 1} & U_{\mu 2} & U_{\mu 3} \\ U_{\tau 1} & U_{\tau 2} & U_{\tau 3} \end{pmatrix} \begin{pmatrix} \nu_1 \\ \nu_2 \\ \nu_3 \end{pmatrix} =$$

$$\begin{pmatrix} c_{13}c_{12} & c_{13}s_{12} & s_{13}e^{-i\delta} \\ -c_{23}s_{12} - s_{13}s_{23}c_{12}e^{i\delta} & c_{23}c_{12} - s_{13}s_{23}s_{12}e^{i\delta} & c_{13}s_{23} \\ s_{23}s_{12} - s_{13}c_{23}c_{12}e^{i\delta} & -s_{23}c_{12} - s_{13}c_{13}s_{12}e^{i\delta} & c_{13}c_{23} \end{pmatrix} \begin{pmatrix} \nu_1 \\ \nu_2 \\ \nu_3 \end{pmatrix}$$

where $c_{jk} = cos\theta_{jk}$ and $s_{jk} = sin\theta_{jk}$. The parameters of the matrix can be classified into different neutrino oscillations. The atmospheric neutrino oscillations are determined by the θ_{23} and Δm^2_{23} parameters. The solar neutrino oscillations are determined by θ_{12} and Δm^2_{12}. And the cross mixing can be determined by θ_{13}, Δm^2_{13}, and δ. This matrix can also be written as the multiplication of the three matrices

$$U = \begin{pmatrix} 1 & 0 & 0 \\ 0 & cos\theta_{23} & sin\theta_{23} \\ 0 & -sin\theta_{23} & cos\theta_{23} \end{pmatrix} \begin{pmatrix} cos\theta_{13} & 0 & e^{-i\delta sin\theta_{13}} \\ 0 & 1 & 0 \\ -e^{-i\delta} sin\theta_{13} & 0 & cos\theta_{13} \end{pmatrix} \begin{pmatrix} cos\theta_{12} & sin\theta_{12} & 0 \\ -sin\theta_{12} & cos\theta_{12} & 0 \\ 0 & 0 & 1 \end{pmatrix}.$$

The parameter δ is still unknown.

Using this matrix and the probability from equation (2.40), it is possible to construct the probability of $\nu_\mu \to \nu_e$ oscillations in vacuum. Ignoring the matter effect, solar term, and CP violating phase, the oscillation probability is

$$P(\nu_\mu \to \nu_e) \approx \sin^2\theta_{23} \sin^2 2\theta_{13} \sin^2(1.27\Delta m^2_{31} L/E_\nu). \tag{2.46}$$

The main goal of the Nova experiment is to find the mixing angle θ_{13} and the CP phase δ.

Chapter 3

The Neutrino Beam and NOνA Detector

3.1 Neutrino Beam

The NOνA Detector Prototype sees neutrino from two different beams, NuMI and Booster. The NuMI neutrino beam is produced at Fermilab using 120 GeV proton from the Main Injector and the Booster beam is produced at Fermilab using 8 GeV proton from the Booster. However, this thesis will present only the analysis with the data from the NuMI.

The process of particle acceleration at Fermilab begins with gaseous hydrogen which is injected into the ion source to produce negatively charged hydrogen ions. The ions are extracted from the source at 18 keV and the pre accelerator produces a beam at 750 keV to be injected into a linear accelerator called Linac. The Linac accelerates the ions to 400 MeV and sends them to the Booster. The Booster takes 500 MeV H^- ions from the Linac, strips the electron off, accelerates the remaining protons to 8 GeV, and then sends them to the Main Injector.

The Booster is a synchroton with a radius of 75.47 meters. It accelerates protons from a kinetic energy of 400 MeV to 8 GeV, using 17 RF cavities with frequency that slews from 37.8 MHz at injection to 52.8 MHz at extraction to match the MI frequency. The injection process lasts for ten Booster turns, resulting in a total average current of 420 mA. The injected beam is a stream of bunches equally spaced at the linac RF frequency of 201.2 MHz.

The main Injector is another synchroton with a radius of 528.30 meters, and its acceleration cycle is 2.2 s. It accepts 8 GeV proton from Booster and accelerates protons to 120 GeV. Fig. 3.1 shows the pictures of the Booster and the Main injector.

Figure 3.1: The Fermilab accelerators. The left plot is a picture from the Booster and the right picture is from the Main injector NuMI.

3.1.1 Neutrino Production

The beam of neutrinos from the NuMI is generated by focusing 120 GeV protons from the Main Injector NuMI onto a graphite target 940mm long, 6.4mm wide and 15mm high. This interaction produces mesons (pions and kaons) as well as other particles. These mesons decay in a pipe filled with He at 1atm, which is 675 m in length and 2 m in diameter. The pions and kaons decay and produce neutrinos. A representation of the generation of the neutrino beam is shown in Fig. 3.2. Two magnetic focusing horns are located next to the target. The two magnetic horns that focus the particles produced in the target are pulsed with a 200kA current, yielding a maximum 30KG toroidal field. The two horns focus positively charged particles and defocus negatively charged particles. These focused mesons decay and produce a neutrino beam. A change of current polarity through the horns produces an antineutrino beam. The mesons decay primarily through the channels $\pi^{\pm} \rightarrow \mu^{\pm}\nu_{\mu}(\bar{\nu}_{\mu})$ and $K^{\pm} \rightarrow \mu^{\pm}\nu_{\mu}(\bar{\nu}_{\mu})$ and the muons decay and produce $\mu^{\pm} \rightarrow \nu_{\mu}(\bar{\nu}_{\mu}) + e^{\pm} + \nu_{e}(\bar{\nu}_{e})$. At the end of the decay pipe is a hadron monitor followed by an absorber to monitor and stop the remnant hadrons. The absorber is followed by rock of about 240 m to stop the muons, leaving only neutrinos [48].

The NuMI neutrino beam can produce different beam energy configurations; since NuMI allows the possibility of changing the relative positions of the target to the horns and changing the horn current. The change in position and current provides a low energy beam, medium energy beam, and high energy beam. In addition, changes in current polarity allows running an anti-neutrino mode. The NOνA Detector Prototype experiment uses the low energy beam and NOνA Near and Far Detector will use the medium energy beam.

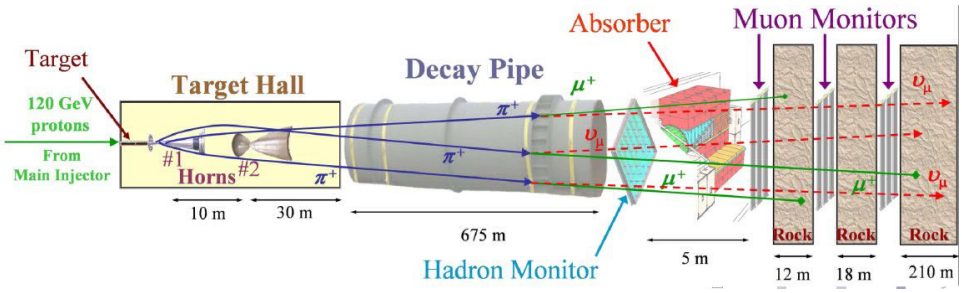

Figure 3.2: Components of the NuMI beam line. 120 GeV protons from the Main Injector hit a graphite target, producing pions and kaons. These charged particles are focused by two parabolic horns into a 675 m decay pipe filled with He. The pions and kaons decay and produce neutrinos. Following the decay pipe is the hadron monitor and the absorber to stop any of the remnant hadrons and charged leptons, leaving only neutrinos.

3.1.2 Neutrino energy

The pions and kaons decay and produce neutrinos. These neutrinos have an isotropic angular distribution in the meson rest frame. In the lab frame, the energy of the neutrinos produced by the decay of pions depends on the energy of the pions and on the angle between the decay axis and the beam direction. The energy of the neutrinos in the lab frame is

$$E_\nu = \frac{(1 - \frac{m_\mu^2}{m_{\pi,K}^2})E_{\pi,K}}{1 + \gamma^2\theta^2}. \tag{3.1}$$

Where $\gamma = 1/\sqrt{1-\beta^2}$, $E_{\pi,K}$ is the energy of pions or kaons and m_μ, m_π, m_K is the mass of muon, pion and kaon. The Figure 3.3 shows neutrino energy spectrum E_ν as a function of the energy of the kaons E_k and the energy of the pions E_π for two different off axis angle $\theta = 110$ mrad and $\theta = 120$ mrad.

The simulated neutrino energy spectra for the NuMI are shown in Figure 3.4. The distributions on the left correspond to the neutrino run and the distributions on the right are for antineutrino run. The blue curve is the ν_μ component and the red curve is the $\bar{\nu}_\mu$. The neutrino mode from NuMI shows two peaks, the low energy peak is produced from the pion decay and the peak around 2GeV is produced from the kaon decay.

3.2 The NOνA Prototype Detector

The NOνA Prototype Detector is located on the surface at Fermilab. This detector is located off-axis at an angle of 110 mrad. The dimensions of the detector are 2.9 m wide, 4.2 m high, and 14.3 m long. The detector is split into the following parts: fiducial event region and a muon catcher made mainly from iron. This detector consists of a total active

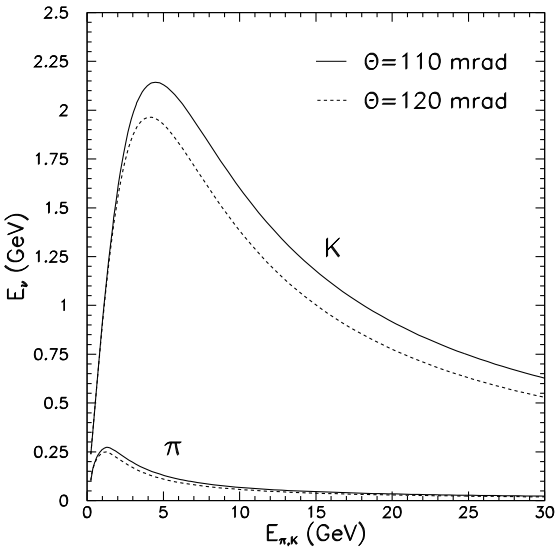

Figure 3.3:

detector PVC mass of 40.973 metric tons, total active detector scintillator mass of 97.67 metric tons; and 86.72 metric of total steel mass located at the end of the detector[48]. The total detector mass is 225.35 metric tons. A representation of the detector is shown in figure 3.5. The detector contains 199 planes of PVC with a liquid scintillator, 99 planes with horizontal cells and 100 with vertical cells.

Studies using the data from Prototype Detector showed that event containment could be a problem for the NOνA Near Detector. For the Prototype Detector we found about 50% of events exit the detector[49]. Now the NOνA Near Detector has been modified and the new dimensions are 4 m wide, 4 m high and 15 m long.

3.2.1 NOνA Detector Technologies

The basic unit of the NOνA detector is a rectangular rigid PVC plastic cell containing liquid scintillator and a wavelength-shifting fiber. Each cell has a wavelength shifting (WLS) fiber of 0.7 mm. The fiber collects the light created in the liquid scintillator. The violet light (380-425nm) emitted by the scintillator is reflected by the TiO2 in the PVC walls and finally absorbed by a fluorescent dye in the WLS fiber. The blue green (450-650 nm) light emitted by the dye is partially trapped within the fiber by total internal reflection. The short wavelength light less than 520 nm is attenuated while traveling through a full length of the WLS fiber, however the longer wavelengths are only weakly attenuated.

The figure 3.6 illustrates a cell with a fiber that is looped at the bottom. When a charged particle goes through the cell, the scintillator produces light. This light bounces around the

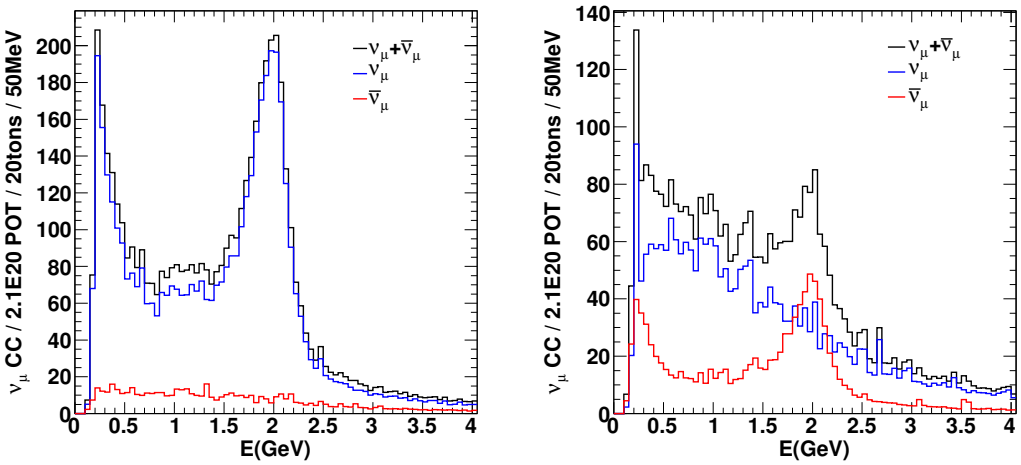

Figure 3.4: Simulated neutrino energy spectrums. The blue distribution is the energy spectrum for the neutrinos ν_μ, the red distribution is the energy spectrum for the antineutrinos $\bar{\nu}_\mu$ and the black distribution is the energy spectrum for the addition of neutrinos and antineutrinos $\nu_\mu + \bar{\nu}_\mu$. Left: Neutrino run from NuMI. Right: Antineutrino run from NuMI.

rectangular cell which has a width of W=3.87cm and depth of D=6cm until the lights gets captured by a wavelength shifting fiber or absorbed by the PVC or the scintillator.

The NOνA PVC is designed to be highly reflective by adding more titanium dioxide (TiO_2). This can yield reflectivity values as high as 92% at 430 nm, near the peak of the scintillator emission spectrum. A PVC module consists of a 32 cell PVC extrusion assembly, and end-plane, and a fiber manifold. A module representation is illustrated in the right plot of Figure 3.6. At the bottom of the extrusion, the end is glued with an end-plate. At the top of the extrusion, the two fiber ends per cell are routed through a PCV manifold to an optical connector. The manifold cover is glued to the snout and on the top of the snout is the electronic box, which carries the front end board with the electronics.
The modules are glued into a block, in alternating horizontal and vertical orientations as shown in Figure 3.7.

3.2.2 Photodetector

NOνA uses avalanche photodiode (APD) photodetectors operated at a gain of 100 and readout via a Front-End Board (FEB). Both ends of the fiber are connected to one pixel on an Avalanche Photodiode (APD). The light detectors(APD) provides high quantum efficiency but low amplification. Electronic noise is reduced using Peltier effect coolers and a water cooling system which allows the APDs temperature to be maintained at $-15C$. Because condensations problems in the prototype detector, the APDs were run without cooling for most of their operation. The APDs are packaged in arrays of 32 pixels and

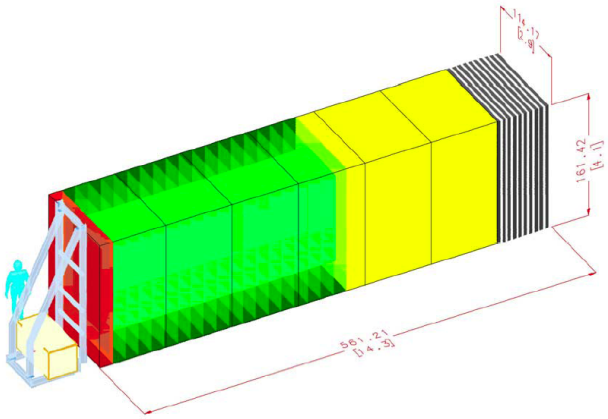

Figure 3.5: NOνA Near Detector. The dimensions of the detector are: 2.9 m wide, 4.2m high; and 14.3m long. The green region represents the fiducial volume and the region in black represent the muon catcher.

mounted on a carrier board. This is shown in Figure 3.8.

The APDs use the photoelectric effect to convert light to electricity. The light is absorbed in the collection region, electron-hole pairs are generated and under the influence of the applied electric field, electrons propagate to the p-n junction. At the junction, the electric field is high enough that avalanche multiplication of the electrons occurs. The multiplication of the current is determined by the electric field at the junction and by the mean free path of the electrons between ionizing collisions, which depends on both the accelerating field and on the temperature. This light is converted to an electric signal and which is processed through electronics of the front end boards.

3.2.3 Front End Boards

The NOνA Detector uses a Front-End Board (FEB) for each module to readout signals from the APDs. Each FEB reads out the 32 pixels from one APD.
The FEB is connected to the APD carrier board as in shown in Figure (3.9). This figure shows the ASIC amplifier which provides amplification and shaping of signal followed by multiplexing to an array of ADCs on the FEB for digitization. The FEBs readout is continuous with no dead time.
The FEB FPGA applies a Digital Signal Processing (DSP) algorithm to select signals above a configurable pixel-by-pixel programmable threshold for each channel and extract the pulse height and timing edge for the signal. The timing resolution determined by the DSP is better than the digitization period because a Matched Filtering algorithm compares the raw

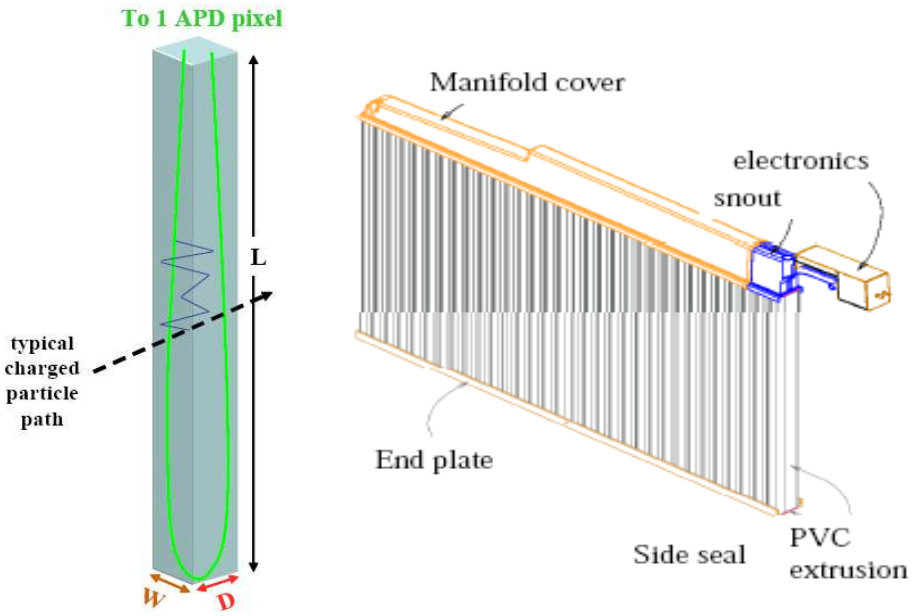

Figure 3.6: Representation of a module constructed with two PVC extrusions, each PVC extrusion is made by 16 cells. The main components for each extrusion are shown: manifold cover, end plate seal, snout, and electronic box [48] .

data response to an ideal response function in the FPGA. The algorithm used in Detector Prototype is a simple Dual Correlected Sampling algorithm which subtracts the signal from the baseline [50].

The NOνA detector uses a Data Concentrate Module (DCM) to consolidate and concatenate the data from up to 64 FEBs; program, configure and monitor the FEBs; and pass the Timing System Clock and Sync command to the FEBs. The FEB FPGA produces timing markers at periodic intervals (50μs) interspersed with digitized hits. The digitized hits are consolidated by the DCM FPGA to 50μs time slices containing data from all 64 FEBs. An application running on the DCM CPU consolidates this data further to a longer time slice (5ms) and routes this time slice to a downstream buffer node for further processing.

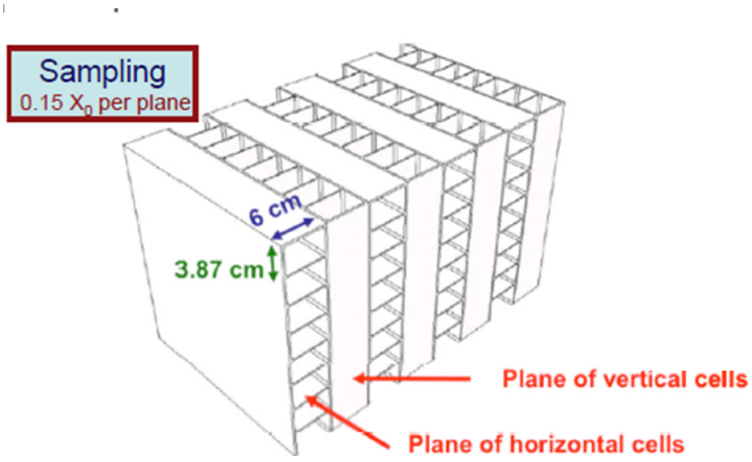

Figure 3.7: Representation of the detector layout[48]

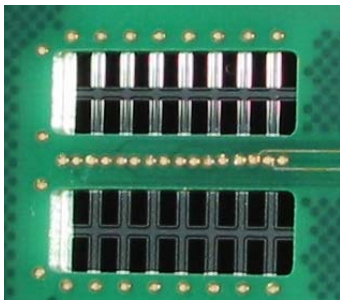

Figure 3.8: NOνA APD mounted on a carrier board [48].

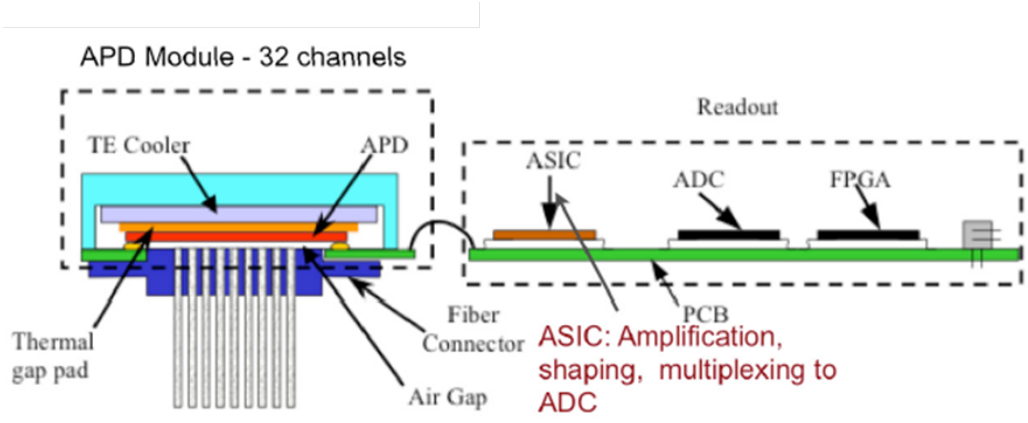

Figure 3.9: Schematic view of a Front End Board[50].

Figure 3.10: Photo of a FEB from the Near Detector Prototype.

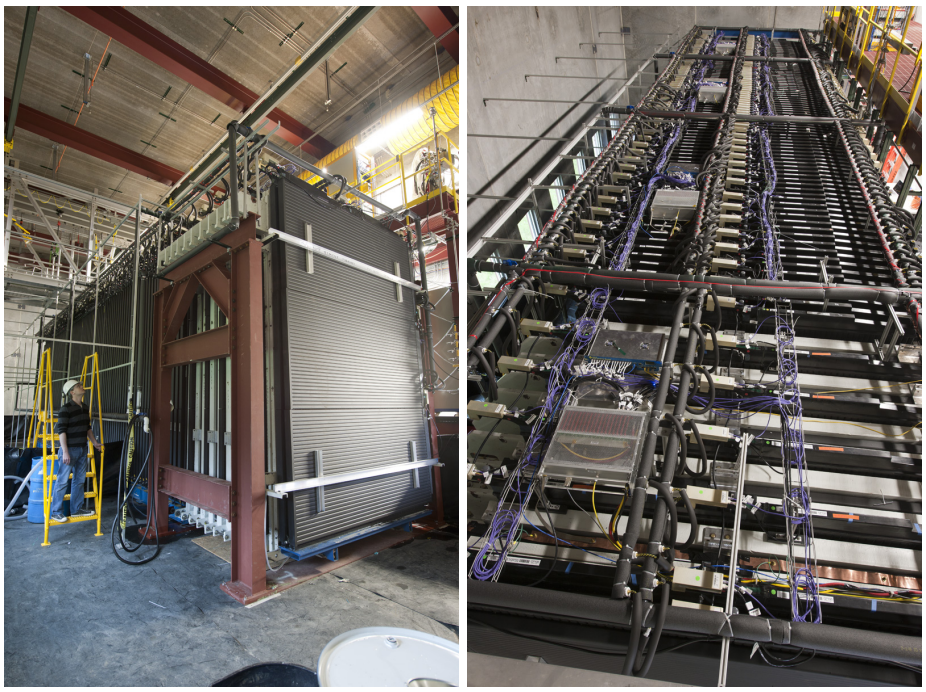

Figure 3.11: NOνA Detector Prototype. The left shows a photo of the entire detector, the last planes are the muon catcher made of alternative planes of PVC modules and steel. The right photo shows the top of the detector. This photo shows the data concentrator modules and the electronic boxes that contain the FEB and the APD.

3.3 Detector Prototype Commissioning

The main goal of the Detector Prototype was to test all the detector systems including: assembly technique, data acquisition system, APD installation, scintillator filling, electronic installation and commissioning, as well as study its response to the NuMI beam neutrino beam and cosmic rays events.

The operation of the Detector Prototype allowed us to test and modify detector systems as necessary before building the NOνA Far and Near detectors. For example, base on the prototype experience installation procedures have changed, the APDs and scintillation filling procedures were also changed[51]. Furthermore, the manifold cover plastic developed some cracks in the Detector Prototype which were repaired. These covers were redesigned for the Far Detector[52].

3.3.1 Performance of the detector

The Detector Prototype started taking data in October 2010. Table 3.1 summarizes all detector configurations taken with the Near Detector Prototype, the beam configurations and the number of protons on target (POT) collected. We collected both cosmic ray data and neutrino data.

Table 3.1: Neutrino and Anti-neutrino configurations.

Neutrino beam	Neutrino	Neutrino
Protons on Target	$9.63 \times 10^{18} POT$	1.7×10^{20}POT
Dates	04-05 2011	10-2011 to 04-2012
Detector configuration	configuration 1	configuration 2

Simulation and reconstruction software have been developed and tested with the Detector Prototype. Figure 3.12 shows the track reconstruction efficiency for Monte Carlo cosmic muons and 2 GeV muons as a function of the zenith angle of the true tracks for the Detector Prototype [53].

The performance of the detector has been study using cosmic data. Figure 3.13 shows the measured cosmic ray muon rate as a function of the time for the Detector Prototype. The plot shows the rate changes over time as APDs are added and removed from the detector. The estimated cosmic ray muon rate is 1.95kHz [54].

Another measure of the performance of the detector is the mean energy deposition or light level for cosmic ray muons as a function of time[55]. This is shown in figure 3.14. The figure shows 8 channels in one module as a function of time. The change in the light level is due to cooling the channels and their subsequent gain change. In addition, the plot shows a slow drop of light levels due to an oil leak in the module.

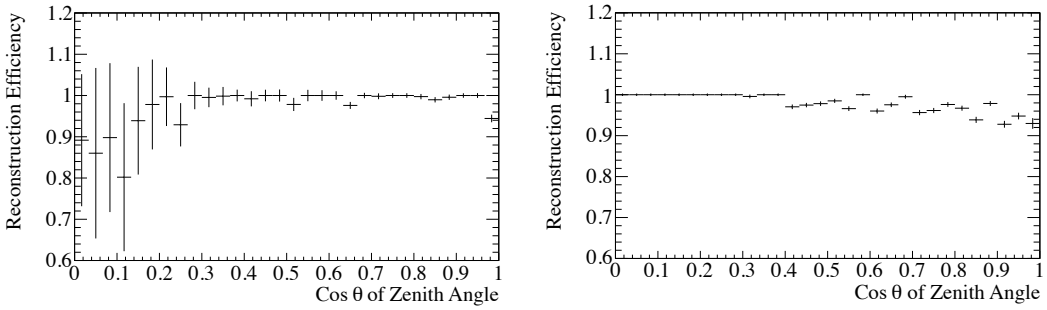

Figure 3.12: Reconstruction efficiency of simulated MC as a function of the zenith angle of the true tracks. Left: Simulated cosmic ray. Right: Simulated uniform distributed single particle 2 GeV muons tracks. Plots taken from [53]

The detector response calibration was studied for the the quasi-elastic analysis, details of this work is presented in the thesis [55].

3.3.2 Neutrinos in the Detector Prototype

We collected data with a trigger window associated with the NuMI beam spill. The trigger window is open for 500 μs synchronized with the 10 μs long NuMI spill. The plot on the left figure 3.15 shows the time for the neutrino interaction candidates from NuMI beam relative to the start of 500 μs window. The right plot in figure 3.15 contains an extra selection which requires correlation with the NuMI beam direction. We apply $\cos\theta_{NuMI} > 0.7$ to remove the cosmic background. At this stage in the commissioning, neutrino interaction candidates required only events which had more than 4 hits in each view and the vertex of the event in the fiducial region. The fiducial region is defined as follows: $|x| < 110$ cm, $|y| < 140$ cm and the longitudinal coordinate $z > 50$ cm and $z < 770$ cm. The reconstruction used for commissioning analysis is called Cana. This reconstruction takes any collection of raw hits and tries to fit a 3D line to them, more details are given in [56].

Using the fiducial region and a time cut to select only the events that are in time with the neutrino beam, the reconstructed particle track angle with respect to the beam direction is shown in figure 3.16. The distribution shows that the neutrino events are peaked around $\cos\theta_{NuMI}$ equal 1 in black. The peak for small values of $cos\theta_{NuMI}$ is due to cosmic background. The solid line shows the data not in the NuMI spill window. This data has been normalized to the in time data according to the relative sizes of the time windows used to select the events.

During the commissioning of the Detector Prototype APDs were damaged when they were cooled to their nominal operating temperature of -15 degrees C. This was caused by the condensation of atmospheric water vapor on the active surface of the APD because the

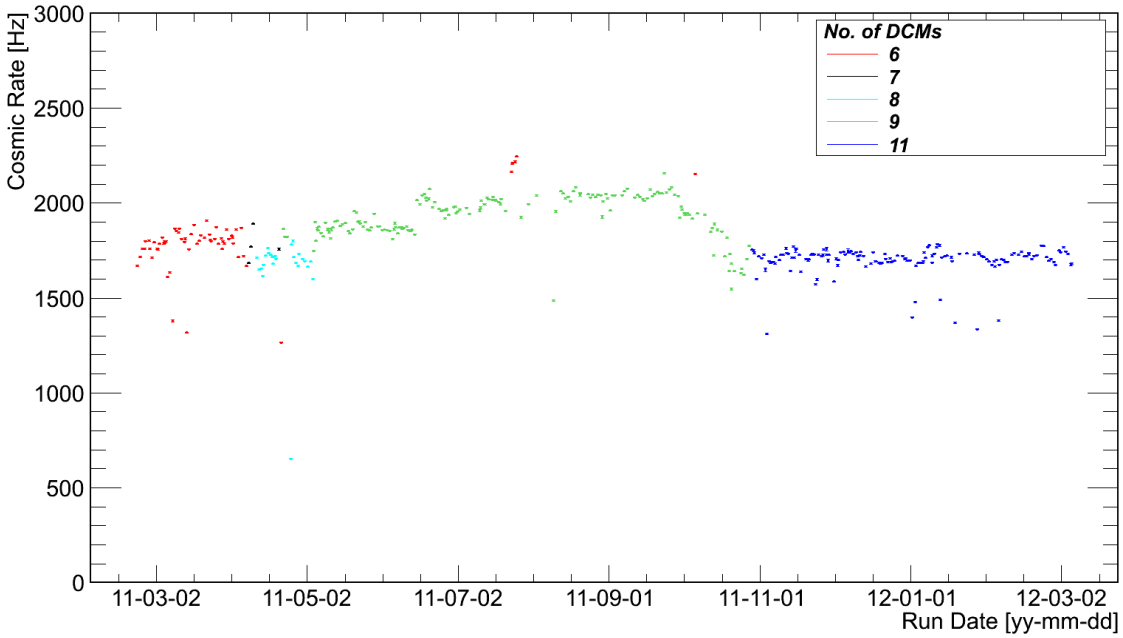

Figure 3.13: Cosmic rate in the Detector Prototype as a function of time. Each color corresponds to the number of active DCMs which is proportional to the number of active channels in the detector [54].

design of the seal between the atmosphere and the APD allowed for improper mounting. The APD tests of the Detector Prototype showed the necessity of having a surface coating for APDs to protect the surface from potential contact with contaminants. . Because of this the design of the NOvA detector was changed by adding a parylene coating to the APD surface as well as a dry air flow to that APD surface[51].

Because cooling damaged many APDs, we had to reconfigured the channels of the detector [57]. Analysis tools were developed to study the different configurations and from this study a reconfiguration was chosen and implemented. Figure 3.17 shows the two detector configurations. The detector in the period between April to May 2011 we called configuration 1 and in the period from October 2011 to April 2012 we called configuration 2. In next chapters we will show the data from each configuration separately.

Figure 3.18 shows the distribution of the number of active channels as a function of time and the distribution of the number of candidates per POT as function on time. The number of channels increases with time as more APDs were installed and then decreases as the cooling system was turned on and APDs were damaged by water condensation. The maximum number of active channels correspond to the configuration 1.

During this time the neutrino production target had to be replaced. Figure 3.19 shows

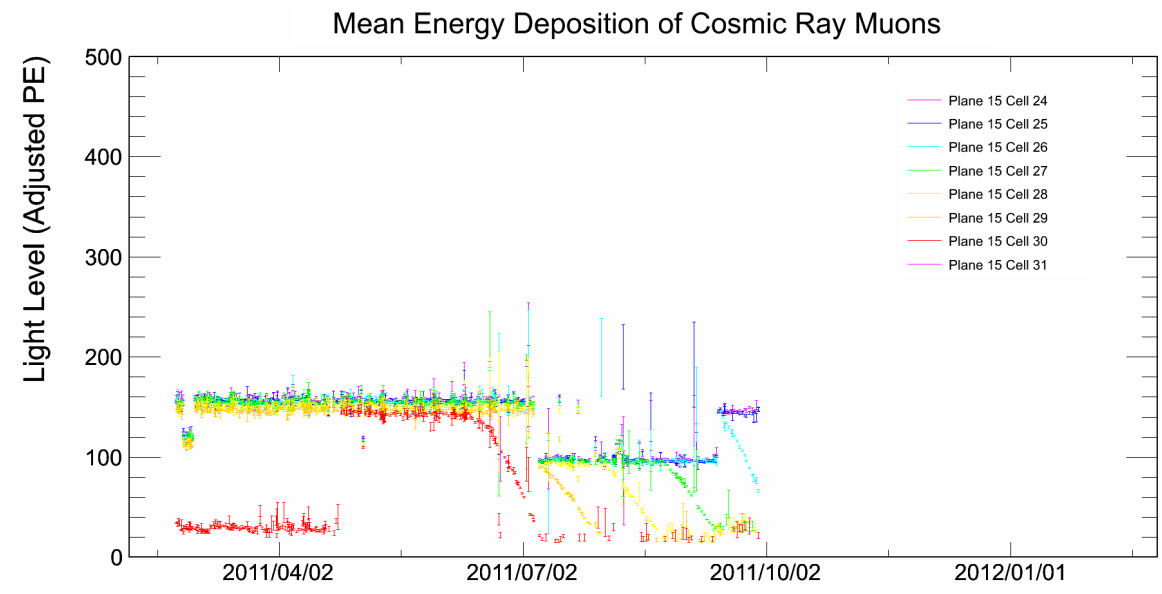

Figure 3.14: Light level in 8 channels on an APD as a function of time. Each color corresponds to one of those 8 channels responses. The first low point is due to low levels of scintillator in that cell, once it was filled the light level returned to a value similar to the other channels. The slow drop of light levels in these 8 channels is due to a leak in the module. The general shift in light levels in July through September are due to cooling tests on the APDs. Plot taken from [55].

the number of candidates as function of Protons on Target for the different target configurations. The different targets are represented with different colors.

Analysis of the Detector Prototype data required proper tracking of the live channels both between the two configurations and within each configuration. We developed a channel masking technique which removed the dead channels from the detector simulation, details can be found [59]. The channels are removed before any reconstruction in both Data and MC. Figure 3.20 shows an example of cell number as a function of plane number for the active channels and the dead channels from a data run (Run=12141). The red dots are the bad channels and the green dots are the good channels.

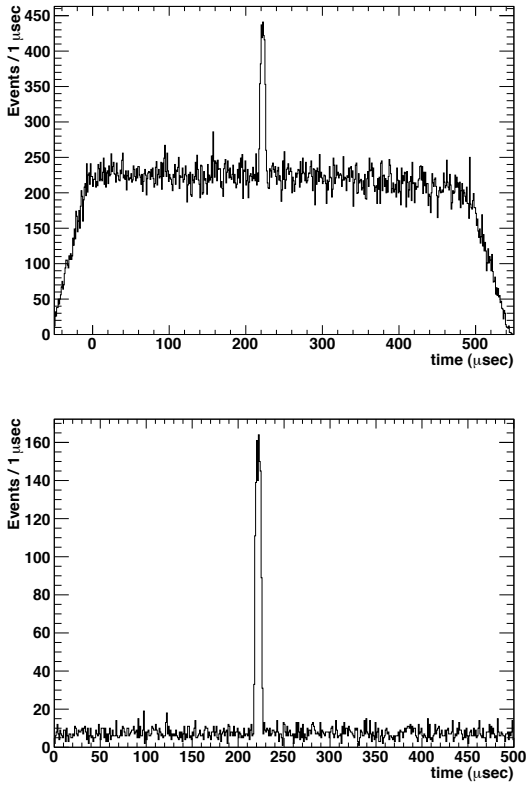

Figure 3.15: Arrival time of events inside the NuMI trigger windows. Top: Fiducial cuts applied and four hits in each view. Bottom: Fiducial cuts, four hits cut and required correlation with the NuMI beam direction $\cos\theta_{NuMI} > 0.7$. The sharp spike shows the NuMI beam.

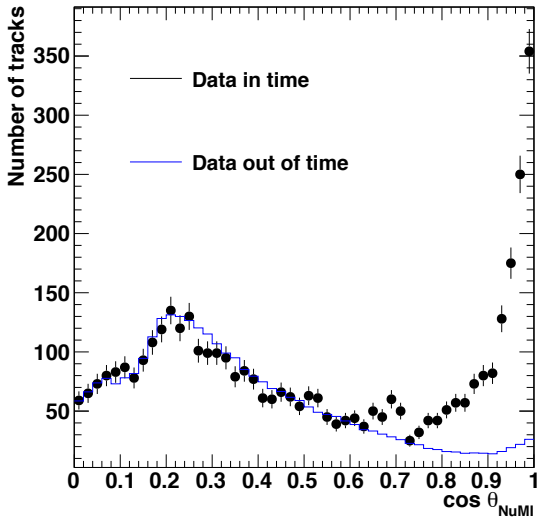

Figure 3.16: Reconstructed particle track angle with respect to the beam direction using fiducial cuts and four hits in each view.

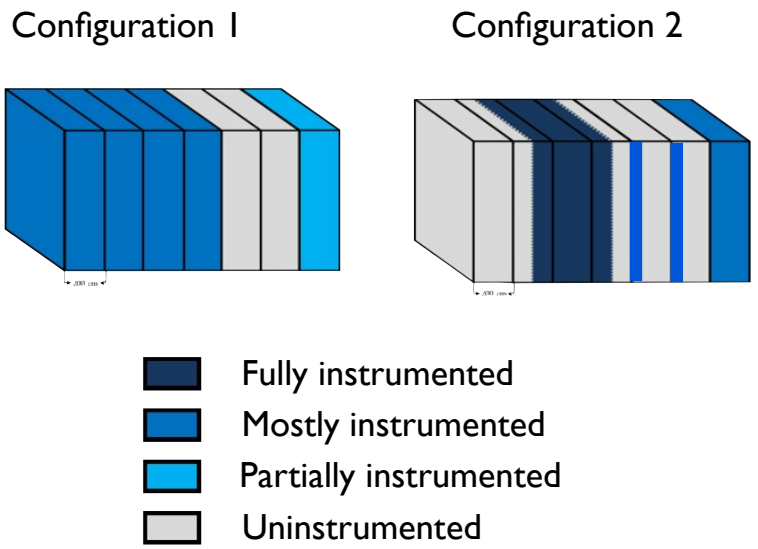

Figure 3.17: Detector configurations. On the left is the configuration 1 and on the right the configuration 2. Figure taken from [58].

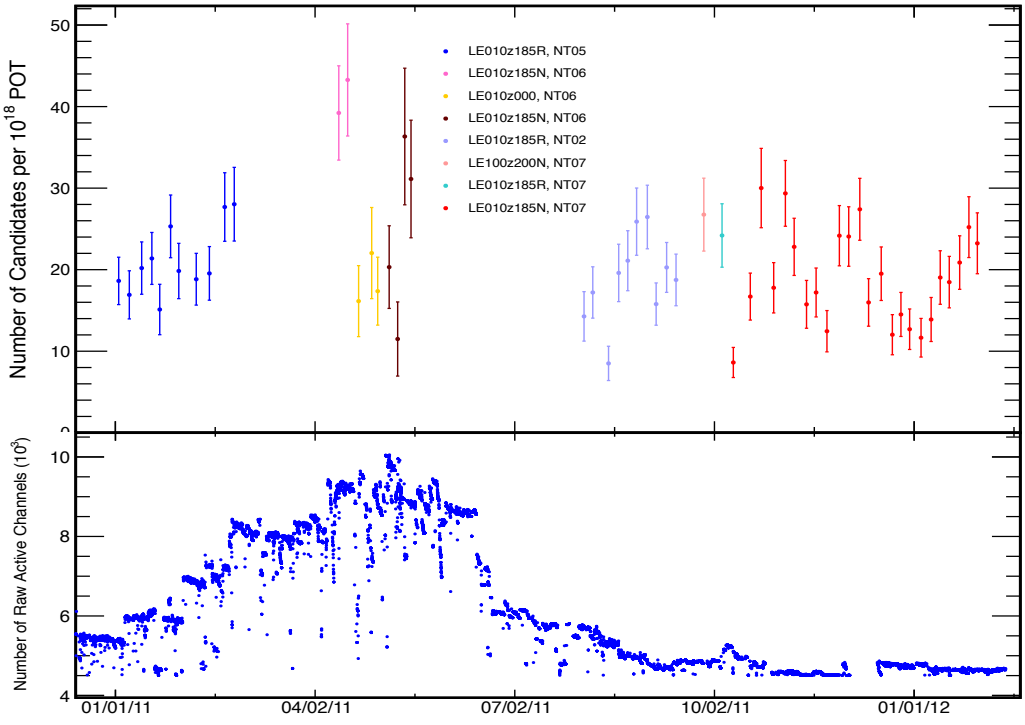

Figure 3.18: Top distribution shows the number of candidates for each target configuration as a function of time. The bottom distribution shows the number of raw active channels as a function of time. Plot taken from [60].

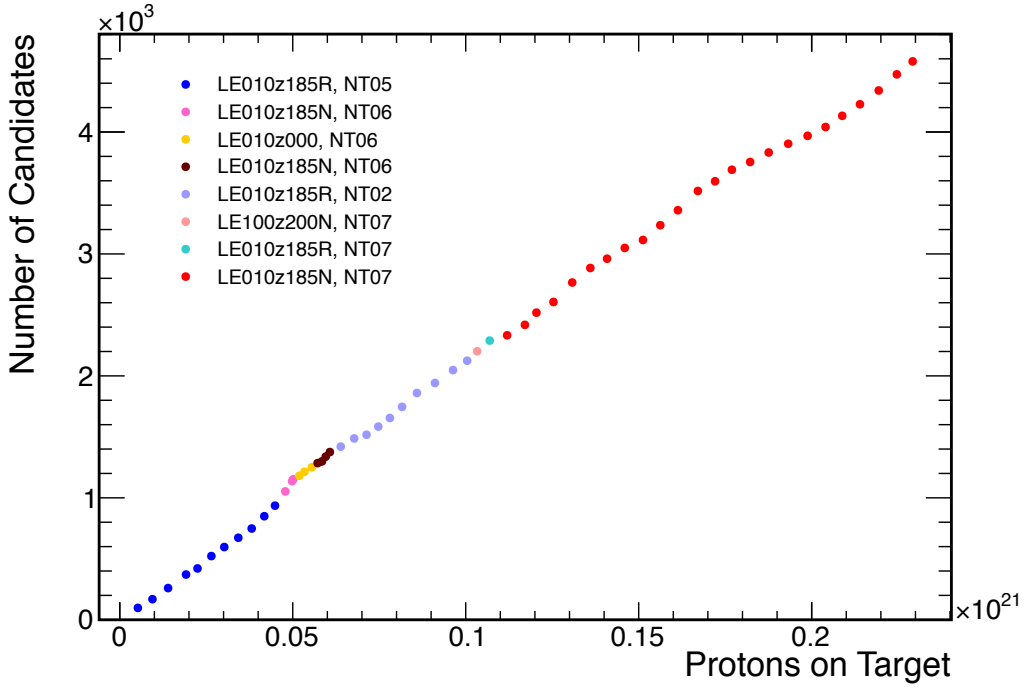

Figure 3.19: Number of candidates as a function of the Protons on Target. Plot taken from [60].

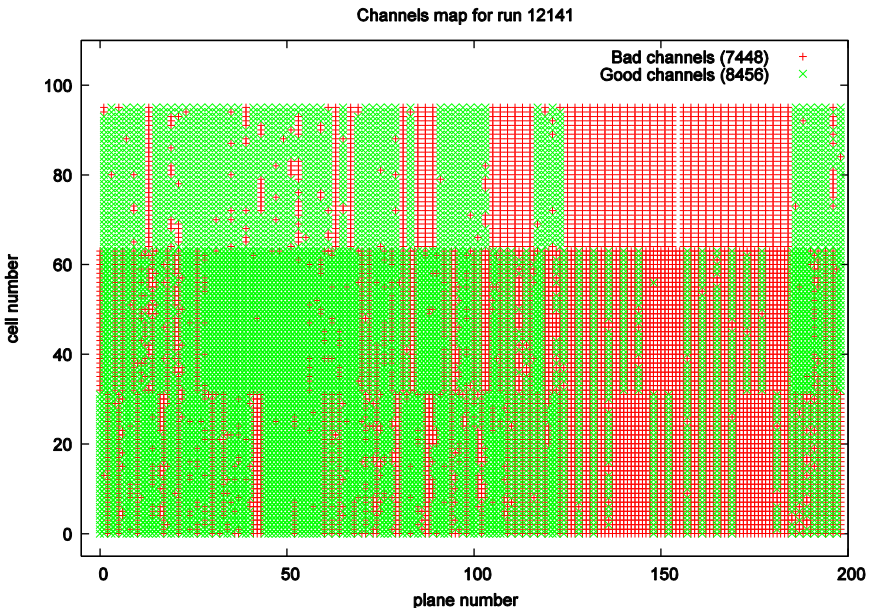

Figure 3.20: Cell number as a function of plane number for run 12141. The red colors show the bad or uninstrumented channels and the green colors shows the good channels.

Chapter 4

Simulation, Reconstruction and Detector Calibration

4.1 Monte Carlo Simulations

Monte Carlo simulations provide predictions for the different processes that produce the quasi-elastic interactions in the detector. The simulations start with the creation of the beam of neutrinos, interact the neutrinos in the detector and propagate the particles resulting from the neutrino interaction through the detector. Finally the simulations provide the tools to develop the analysis. A summary of the different simulations used in the NOνA experiment is presented below

1. The first step of the simulations is the production of the neutrino flux for the NuMI beamline as was described in Chapter 3. This simulation includes the production of hadrons by 120 GeV/c protons interacting with the NuMI target and the propagation of those hadrons through the magnetic horns, along the decay pipe. NOνA uses Flugg (FLUGG 2009.4)[61], a combination of Fluka and Geant4. Fluka performs proton scattering on the carbon target and interaction of secondary particles within the target and writes an output file containing all of the produced particles and their kinematics. This output is taken by Geant4 which propagates the particles through the horns and decay pipe. The resulting flux simulation saves the particle decays which produce the neutrinos passing through the detector and this flux file is used as input for the neutrino event generation in GENIE.

2. The second step is the generation of neutrino interactions in the NOνA detector. This is done using the GENIE simulation, (GENIE stand for Generates Events for Neutrino Interactions Experiments, version GENIE 3665). GENIE uses the output flux

from the Flugg simulation and pre calculated neutrino cross sections to determine if individual neutrino rays pulled from the flux interact in the detector geometry. The neutrino interaction modeling is made in three steps; the first primary interaction inside nucleus, second; the hadronization and finally the intranuclear hadron transport[63].

3. Final states of the neutrino interactions are used by Geant4. This simulation propagates the final state particles through the detector. Geant4 simulates the physics of energy loss, particle scattering, decays, etc. This step is in charge of the particles energy deposition and decays.

4. The final step in the simulation is the light propagation and DAQ electronics. This simulation does the photon production by charged particles traversing liquid scintillator and the transport, capture and transmission of photons through the fibers as well as the conversion of photons to photoelectrons in the APDs.

These simulations save the information about each interaction. For example GENIE preserves the true information about the neutrino as well as the energy, the vertex position, the type of interaction of each neutrino interaction. Geant4 stores the true energy deposited in each cell and the trajectory of each of the particles produced. And the final step in the simulation provides the energy deposited in the detector registered by an APD in unity of ADC value. We will explain later how the calibration calibration data is used to convert the signal from APD to energy.
The next sections describe the topology of neutrino interactions in the Near Detector Prototype, the reconstruction used for the quasi-elastic analysis and the detector calibration.

4.2 Neutrino Interactions in the NOνA Detector Prototype

The NOνA Detectors are designed to study electron neutrino, muon neutrino interactions. The initial step to reconstruct and identify the quasi elastic interactions was done using human scanning of the Monte Carlo simulations. This section provides a description of the event topology in the NOνA detector.

4.2.1 Event Topologies

Initially, simulated events were scanned by hand for each type of neutrino interaction in the Detector Prototype. Using the true information from the Monte Carlo for charged current and neutral current interactions of muon neutrinos we scanned about 100 events from each

type of interaction (QE, RES, DIS and COH). The summary of the scanning is presented below.

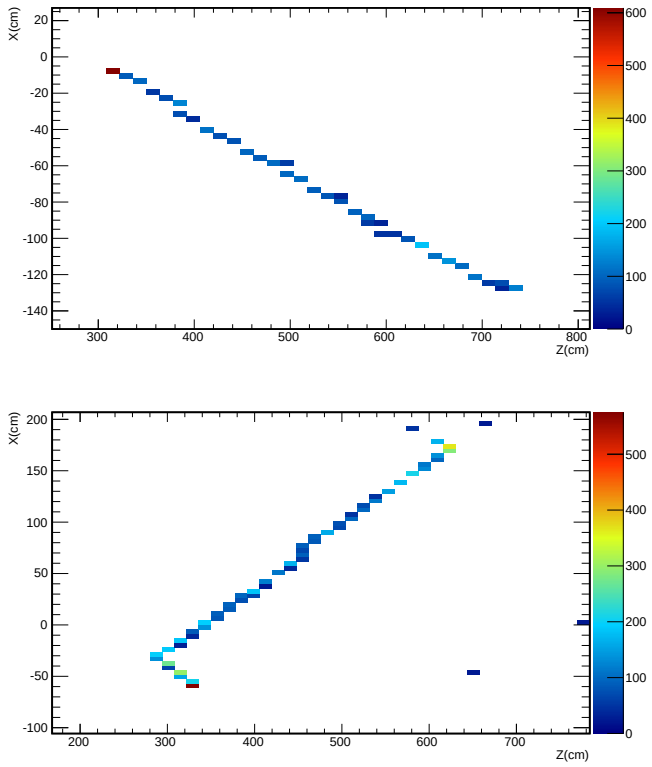

Figure 4.1: Quasi elastic events. The top plot shows a simulated quasi elastic event with a non-visible proton at the vertex ($\nu_\mu[1.9GeV/c] + C \rightarrow \mu[1.7GeV/c] + n[0.4GeV/c] + p[0.4GeV/c]$). The bottom plot shows a true quasi elastic event with a muon and a visible proton track ($\nu_\mu[1.3GeV/c] + C \rightarrow \mu[0.9GeV/c] + p[0.8Gev/c] + X_{200000101}$).

1. Quasi-elastic interactions: Scanning studies showed 5% of events have 2 visible tracks, about 75% of those events have a detectable muon and proton at the vertex and 21% of the quasi-elastic events have some activity around the vertex. The activity is defined as one or two cells hit around the vertex. The figure 4.1 shows two examples of quasi elastic events. This figure shows one view of the track (the x or horizontal direction) as it progresses longitudinally through the detector planes (the z direction). The color of the hits shows the relative amount of energy deposited in a cell. Two topologies for the quasi elastic interactions are shown, the top shows a single track from a muon with a proton at vertex position, but the proton does not have a visible track, although it deposits energy around the vertex. The second topology on the bottom shows a long track from a muon and a visible proton track.

2. Resonance interactions: 20% of the events have a single track, 17% of the events have

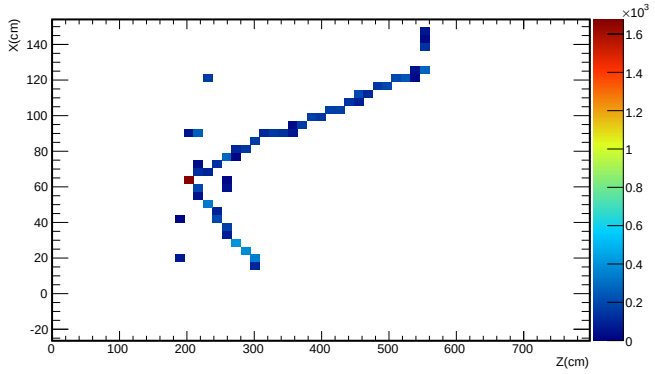

Figure 4.2: Resonance event. A long track from a muon and a second proton track, there is also additional activity around the vertex ($\nu_\mu[1.9GeV/c]+C \rightarrow \mu[0.9GeV/c]+p[1.1GeV/c]+p[0.4GeV/c]+n[0.2GeV/c]+n[0.3GeV/c]+n[0.5GeV]+n[0.3GeV]$)

2 clean tracks and the rest of the events have activity around the vertex or more than 2 tracks. Figure 4.2 shows a simulated CC RES event, which has a long track from a muon and a short track from a proton. There is also additional visible vertex activity.

3. Deep Inelastic interactions: 35% of these events have a track from the muon and activity around the vertex. 65% of these events have more than 3 tracks. Figure 4.3 shows a CC DIS interaction. It is a multi-track event with a long track from a muon and a π^0.

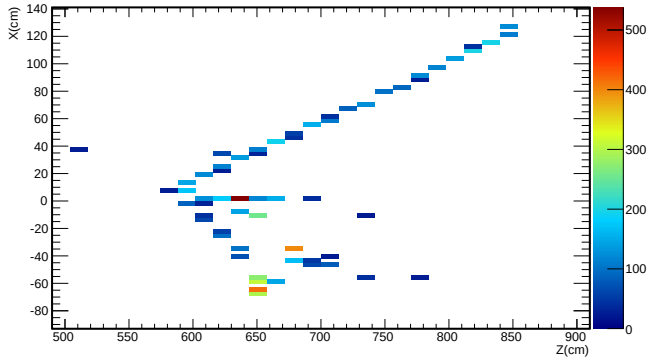

Figure 4.3: Deep Inelastic. A long track from a muon and a pion zero ($\nu_\mu[3.7GeV/c]+C \rightarrow \mu[2.1GeV/c]+p[1.8GeV/c]+n[0.2GeV/c]+\pi^0[0.5GeV/c]$).

4. Neutral current interactions in the NOνA detector are diffuse. Charged pions travel short distances and a π^0 showers in the detector. Figure 4.4 shows a NC interaction with a visible π^0 in the final state.

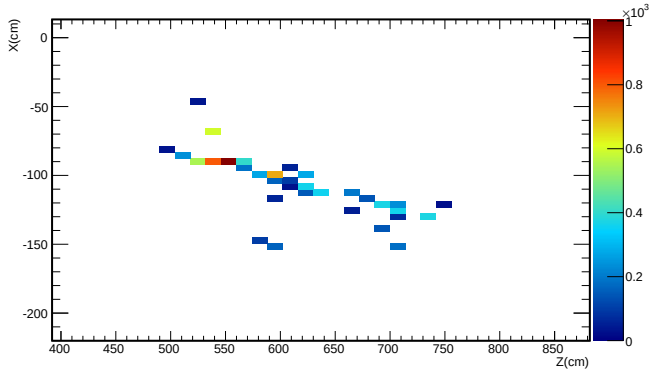

Figure 4.4: Neutral current event with a π^0 in the final state ($\bar{\nu}_\mu[2.7GeV/c] + C \rightarrow \bar{\nu}_\mu[1.1GeV/c] + n[0.4GeV/c] + p[0.1GeV/c] + \pi^0[1.5GeV/c]$).

Table 4.1: Number of prongs for 300 neutrino candidates for the FHC data with configuration 1

Number of prongs	Events	Activity	Fully contained events	Partially contained events
1	185	78	94	91
2	111	70	45	66
3	4	0	2	2

We also scanned the data events within the fiducial region that were not identified as cosmic ray background to study the topology of the real events in the Detector Prototype. Table 4.1 gives a summary of the number of events with one, two and three prongs. We found for configuration 1 that 62% of these events have a single prong with 57% having an identified clean muon. Events with 2 prongs account for about 37% of the total sample and 1% of events have more than 2 prongs. Furthermore, we found that 50% of events are fully contained. We scanned MC simulation events and found similar results, about 50% are fully contained. We found agreement between the data and MC simulation.

Also, we scanned the selected charged current quasi elastic events for configuration 2, details of evaluations are reported at [64].

4.3 Event Reconstruction

This section contains a brief review of the reconstruction used for the quasi-elastic analysis. The first step in the reconstruction chain is called the slicer. This algorithm obtains a list of cell hits sorted by time for each event and groups all the hits that are contiguous in time to form a physics slice. Other hits are grouped into a noise slice[65].
The Kalman Filter reconstruction uses the non noise slice hits for each of the detector views.

This algorithm finds the tracks for each view separately as described below. Once the tracks are found in the 2D views, the algorithm matches the 2D tracks into 3D tracks and save them [66]. Figure 4.5 shows a diagram of the steps used to reconstructed the tracks.
The Kalman Filter starts with a seed track and add hits to the track by projecting the

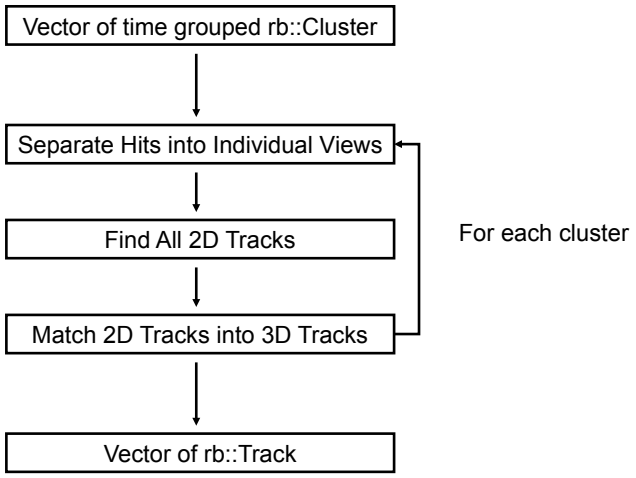

Figure 4.5: Architecture of the Kalman Filter, figure taken from [66].

trajectory to the next hit and including it in the fitted track if it is within the track's uncertainty range.
The Kalman Filter uses a track state at point k represented by

$$\vec{x}_k = viewposition, slope. \tag{4.1}$$

Then the change in the track state from plane k-1 to k is

$$\vec{x}_k = A\vec{x}_{k-1} + \vec{w}_{k-1} \tag{4.2}$$

where A is a matrix that extrapolates the state vector from k-1 to point k and $\vec{w}_k$ represents the process noise that corrupts the state vector. In this case, most of the process noise is due to multiple scattering. More details about the Kalman Filter reconstruction can be found [66].
The tracks in each view are made projecting the track direction plane by plane. Then, if hits are close to the projection they are added to the track. If the projection goes through a maximum gap of 3 cells without adding a hit, the track is terminated. Having the tracks from each view (2D tracks), the final step is to merge those tracks into 3D tracks [66]. These 3D tracks are used for the quasi-elastic analysis. An example of a reconstructed muon with multiple scattering is shown in figure 4.6. The reconstructed trajectory along the muon

track is shown together with the cell hits. Note that the track reconstruction algorithm can follow the particle trajectory even through large amounts of multiple scattering.
We use the Kalman Filter reconstruction for both the Monte Carlo simulations and the data

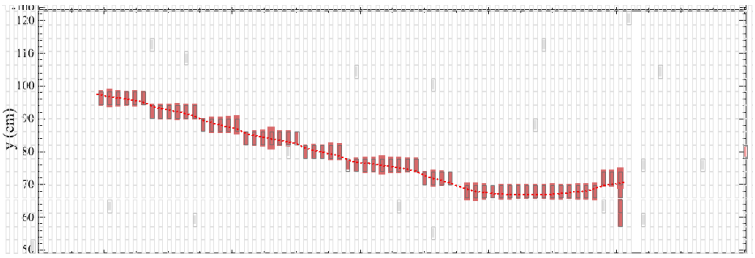

Figure 4.6: Example of reconstructed muon, figure taken from [67].

collected in the Detector Prototype. The next section compares Data and MC distributions in the detector.

4.4 Comparison between Data and Simulations

This section presents a comparison of Data and MC simulations for the Detector Prototype. We compare Data and MC simulations using the preselection criteria for both samples corresponding to the detector configuration from April to May 2011 for which there were 9.6×10^{18} protons on target. The preselections criteria used are the following:

1. Data quality selection: Several cuts are used to select the good runs for the analysis, details about the data quality can be found in [71].

2. Timing selection: Reconstructed events in the beam time window ($t > 217\mu s$ and $t < 227\mu s$).

3. Fiducial cuts: Require the reconstructed vertex positions $|x1| < 115$ cm, $|y1| < 150$ cm and $50cm < z_1 < 770$ cm.

4. cosmic raycut: The cosmic raymuons are removed using the inverse of the slope of the tracks. Require $\frac{z2-z1}{y2-y1} < -1$ or $\frac{z2-z1}{y2-y1} > 1$.

Figure 4.7 compares the data and Monte Carlo simulation for the track length of all the tracks in an event (left plot) and the angle of the tracks with respect to the beam direction $\cos\theta_{NuMI}$ (right plot). The data is cosmic ray background subtracted by using the out of time data (out of time is the data outside the spill window) to predict the in time background. This is done by using all the pre-selection cuts on the out of time data and scaling by the ratio of out of time window to the in time window. The MC simulation has been

scaled to the amount of protons on target (POT) for the data. These distribution shows good agreement between data and MC.

The track vertices for data and Monte Carlo simulations are shown in figure 4.8. The figure

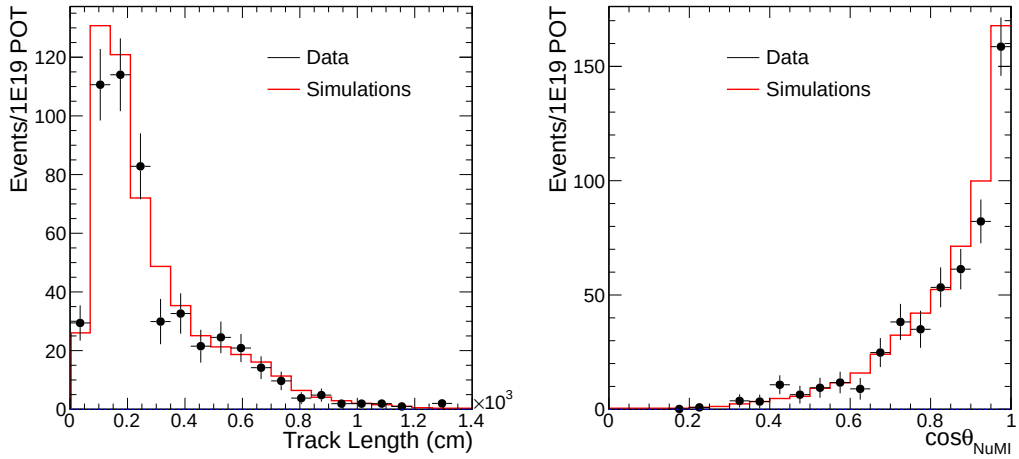

Figure 4.7: Left: track length for the reconstructed tracks. Right: reconstructed track angle with respect to the beam direction. Black points are the data and the red histogram is the simulation.

shows the track vertex X coordinate, the track vertex Y coordinate and the track vertex Z coordinate in centimeter. These distributions shows good agreement between data and MC.

4.4.1 Detector Calibration

We review the calibration used for the quasi-elastic analysis. Details about the calibration chain and the status can be found [68].

Calibration

Cosmic ray muons reconstructed in the Detector Prototype are used to calibrate the detector.

The energy units used in this discussion are the following:

1. ADC: The ADC is the pulse height for a cell as recorded by the analog to digital converter (ADC).

2. PE: PE is the number of photoelectrons detected by the APDs calculated using the ADC ($ADC/1.43$).

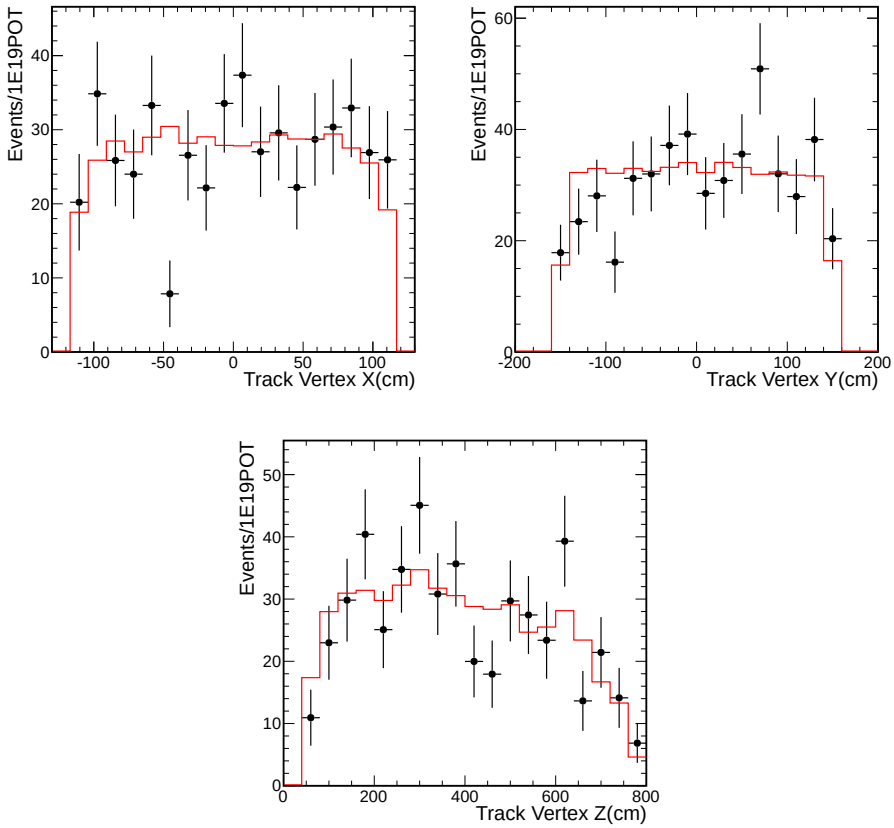

Figure 4.8: Vertex positions of the reconstructed tracks. The black points are the data and the red histogram is the simulation.

3. PECorr: PECorr is the calibrated energy deposited correcting for the attenuation length of the fiber.

4. MIP: MIP is the energy deposited by a minimum ionizing particle traveling along the z direction through the depth of one cell.

5. GeV: Energy in GeV. This energy is obtained using the MIP times a constant[69].

Through going cosmic rayray muons are used to measure and correct the variation in light caused by the attenuation along the WLS fiber in a scintillator cell.
The attenuation fits are done on a channel by channel basis. The fits use the following assumptions: First, the channel response is stable in time. Second, the energy spectrum of cosmic rayrays is uniform in space. Third, the APD response to arriving photons is linear. The pulse hight or (ADC/cm) of the cell crossed from a cell is plotted as a function of the distance from the center of the detector. This distance is called W. The data is fit to a double exponential

$$y = C + A(exp(\frac{x}{X}) + exp(-\frac{3L/2 + x}{X})) \tag{4.3}$$

where y is the response and x is the W position.

Figure 4.9 shows an example of a fit of the cosmic ray data for a single vertical and for a horizontal cell. These plots show a pronounced rolloff on the edges of the ADC/cm as a function of the distance from the center distribution. These rolloffs follow an x^4 polynomial. This was determined empirically [69]. An extra term is used in the fit

$$y = \begin{cases} 1 - \alpha_R(x = x_R)^4 & x > +x_R \\ 1 & \text{otherwise} \\ 1 - \alpha_L(x - x_L)^4 & x < -x_L \end{cases} \tag{4.4}$$

Finally the product of equation 4.3 and 4.4 was used to make the fit. The attenuation and rolloffs are shown in figure 4.9. The plots shows the mean ADC/cm as a function of the distance from center, the left plot is for a vertical cell and the right for a horizontal cell. The roll off is caused by the absorption of light by the dark plastic at each end of the module. Since the light captured by the fiber has been reflected by about 1 m of the plastic of the cell, the distribution should roll off as it approaches the end of the module where there is internal structure supporting the fiber.

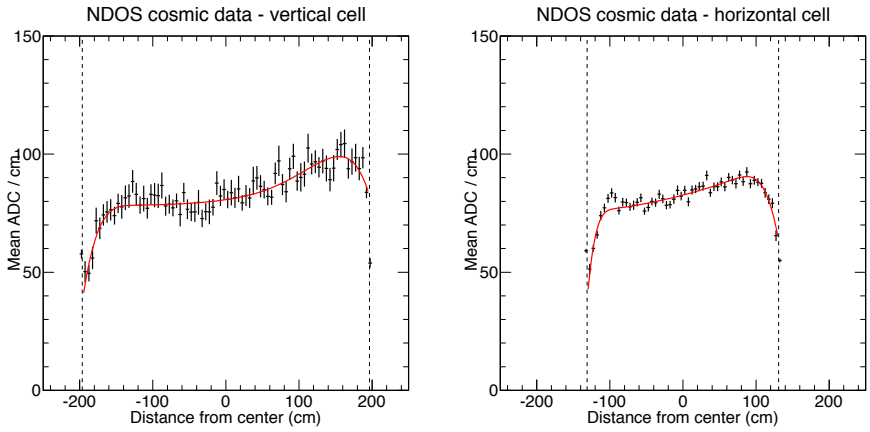

Figure 4.9: Detector response (ADC/cm) of liquid scintillator traversed in the cell as function of the distance from the center of the module for a vertical cell. Left: a vertical cell. Right: a horizontal cell, plots taken from [69]. The dashed lines represent the edges of the detector.

An example of the calibrated visible energy for the NuMI neutrino events in the Detector Prototype is shown in figure 4.10. The total observed energy in the event is shown for Data after the cosmic ray background subtraction and for Monte Carlo simulations. The red distribution is the Monte Carlo and the black is the Data after pre-selection cuts.

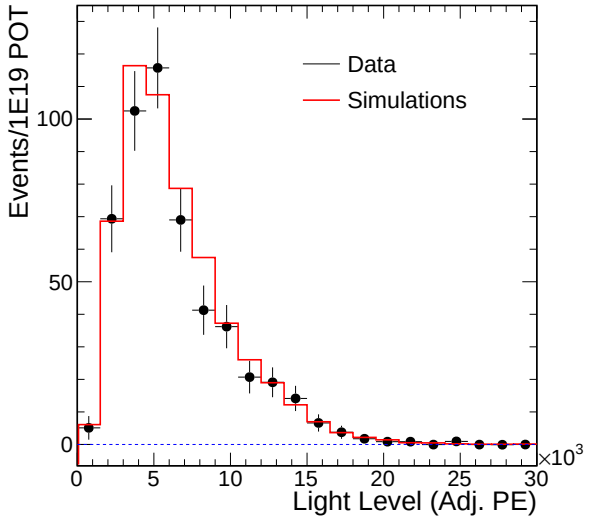

Figure 4.10: Visible energy in the events for the neutrino events. The red is the total MC after pre-selection cuts and the black is the data after pre-selection cuts and cosmic raybackground subtracted events.

Momentum calibration

The muon momentum is obtained using the range of the muons. We use fully contained events and 3D tracks from the Kalman Filter reconstruction. This section describes the technique used to determine the momentum.

A Monte Carlo sample of quasi-elastic interactions is used to calibrate the muon momentum. We fit the muon momentum as a function of the track length. This fit provides values of fit parameters which are used in the MC and the Data to determine the momentum of the tracks.

The Detector Prototype is made of about 12 meters of scintillator and about 2 meters with alternative planes of scintillator and steel in the muon catcher. We use two fits to determine the momentum of the tracks, one fit for the events in the scintillator and a second fit for the events stopping in the muon catcher.

The distributions in the figure 4.11 show range of the muons as a function of their momentum for simulated events in the part of the detector made only of detector modules and also the muon catcher. The top distribution is a scatter plot of the momentum versus the track length and the bottom is the profile of that plot as a function of muon momentum.

The momentum in the scintillator is found fitting the momentum as a function of the track length to a straight line equation $P = aL + b$. The parameters from the fit from the left plot of figure 4.11 are: $a = (0.12182 \pm 0.00164)$GeV/cm and $b = (0.002008 \pm 0.000003)$GeV.

For the events stopping in the muon catcher, we split the tracks into two sections and use

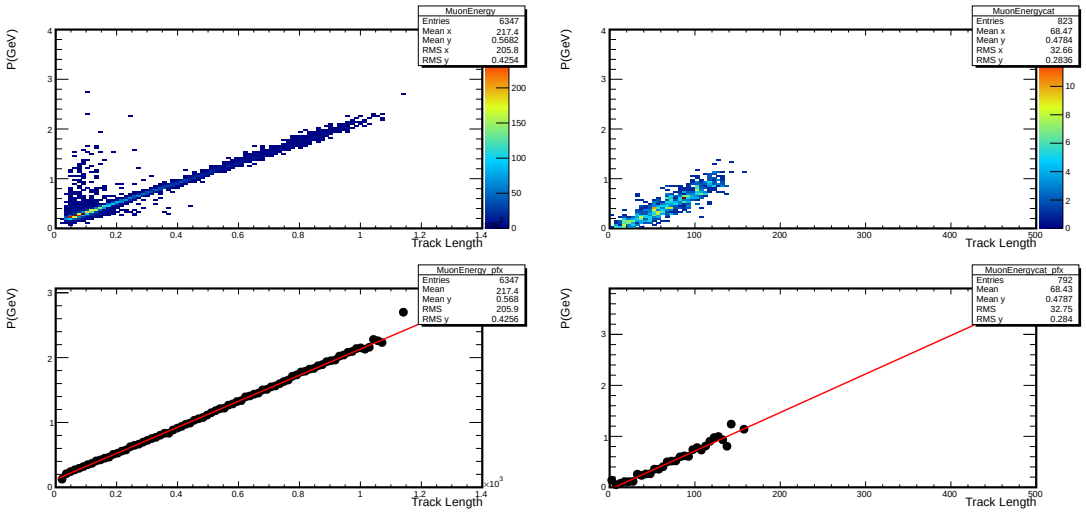

Figure 4.11: Momentum versus track length for simulated CC QE events. We divide the track in two parts: the first part for tracks in the scintillator and the second part for tracks in the muon catcher. The left plots are for the track only in the scintillator modules and the right plots are for the tracks only in the muon catcher. On each side, the top plot is the momentum vs the track length and the bottom is the profile on the top plot fitted to a straight line.

the prediction of the momentum in the modules for the first part of the track and the muon catcher fit for the second part. The muon catcher fit is also a straight line equation with the following parameters $a = (-0.043 \pm 0.006)$GeV/cm, $b = (0.00755 \pm 0.00009)$GeV for the right distribution of figure 4.11.

The length and momentum contained in the muon catcher is predicted as follow

$$\begin{aligned} P_{catcher} &= P(total) - P(modules) \\ L_{catcher} &= L(total) - L(modules) \end{aligned} \tag{4.5}$$

The right distributions in figure 4.11 shows the fit of muon momentum as a function of the track length for the length contained in the muon catcher. The top distribution is the momentum $P_{\mu_{cather}}$ as function of the $L_{\mu_{catcher}}$ and the bottom is the profile and fit.
Finally, we compare the true momentum and the reconstructed momentum for simulated events. Figure 4.12 shows the resolution distribution, where resolution is defined as $(P_\mu(true) - P_\mu(reco))/P_\mu(true)$. The resolution for the momentum is 13% for configuration 1. This distribution shows a tail, because dead channels cause some muons to have a shorter reconstructed track length than their true track length.

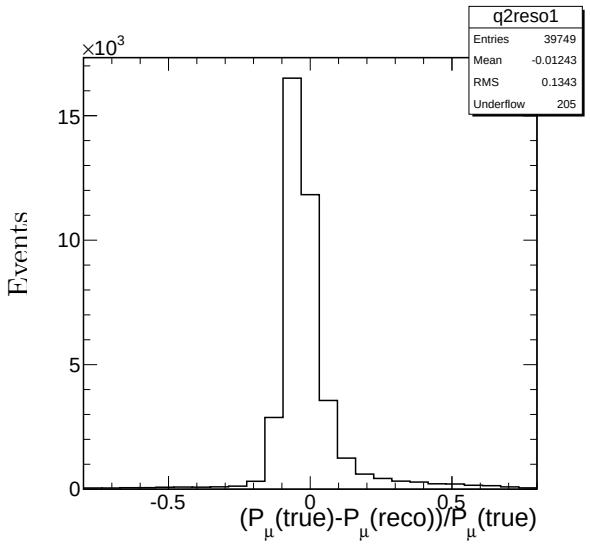

Figure 4.12: Muon resolution, where the resolution is defined as $[P_\mu(true) - P_\mu(reco)]/P_\mu(true)$. The Mean of the resolution is -0.01243 and the RMS is 13%.

Chapter 5

Event Selection

5.1 Charge Current Quasi-elastic selection

This section describes the ν_μ Charged Current Quasi-Elastic (CC QE) interaction selection. This interaction produces a long muon track. In addition to the muon, some CC QE interactions contain a short track associated with a proton. However, the number of CC QE interactions with a visible and reconstructed second track from proton is small. Using scanning we found about 4% of the CC QE interactions have a second visible track from proton, with at least four hits in each view. Four hits is the minimal requirement for the Kalman Filter to reconstruct a track. Since the number of ν_μ CC QE events with a second visible track from proton is small we make a selection for the CC QE using one and only one reconstructed track, (3D reconstructed tracks).
The CC QE selection is made using two steps: first we apply pre-selection cuts to remove events at the edge of the detector and remove cosmic ray background events; then we use a kNN algorithm to select the CC QE interactions.

5.1.1 Pre-selection Cuts

The pre-selection cuts are defined as follows:

- Event passing Data quality checks[71] and within the 10 microsecond beam spill between $217\mu s > t < 227\mu s$.
- Interaction fiducial cuts: Interaction point 50cm from the edge of the detector

$$|x_1| < 115cm, \quad |y_1| < 150cm, \quad 50cm > z_1 < 770cm, \tag{5.1}$$

  where the (x_1, y_1, z_1) are the reconstructed vertex positions, considering the smallest value of z for the track as the vertex position. For configuration 2 we adjust the z

coordinate cuts to $300cm > z_1 < 500cm$, since the instrumentation was moved to a fiducial region around these coordinates . Figure 5.1 shows an event display with the coordinate system.

- Cosmic ray background rejection: The inverse of the slope of the tracks in the y view is used to remove the cosmic ray background.

$$C3 = \frac{Z_2 - Z_1}{Y_2 - Y_1}. \tag{5.2}$$

  where 1 and 2 refers to the beginning (most upstream z) and end of the reconstructed track. A detail study was made to determine the cuts on this variable. Appendix C shows a summary of the study. Cosmic ray muons tracks are rejected using $-1 < C3 < 1$.

- One and only one reconstructed track, (3D reconstructed track).

- Events with track length greater than 60 cm.

- Containment fiducial cut: $|x_2| < 115cm, \quad |y_2| < 150cm; \quad and \quad z_2 < 1350cm$, where x_2, y_2 and z_2 are the end positions of the reconstructed tracks. The containment cuts are the same for both configurations.

- Events exiting the detector from the side: This is done extrapolating the tracks in both detector views, vertical (Y) and horizontal (X), and rejecting those tracks that are likely to exit the detector. This cut is only used for configuration 2, since this configuration has fewer active planes.

In addition to the pre-selection cuts, a k-Nearest Neighbour (kNN) classifier is used to select the final sample of CC QE interactions. The motivation for using this algorithm is to separate quasi elastic signal events from the neutral current, charged current resonance and charged current deep inelastic background events with a single reconstructed track. The pre-selection cuts remove a significant amount of background events with multi prongs, but the background events with a single pion or proton track are still there. The Table 5.1 shows the percent of events remaining after each pre-selection cut, after the fiducial cuts.

5.1.2 Using a k-Nearest Neighbour Classifier (kNN)

The kNN is one of the standard algorithms used in high energy physics to separate signal from background. The kNN method is part of the TMVA ROOT classes. A summary of the method is taken from [72].

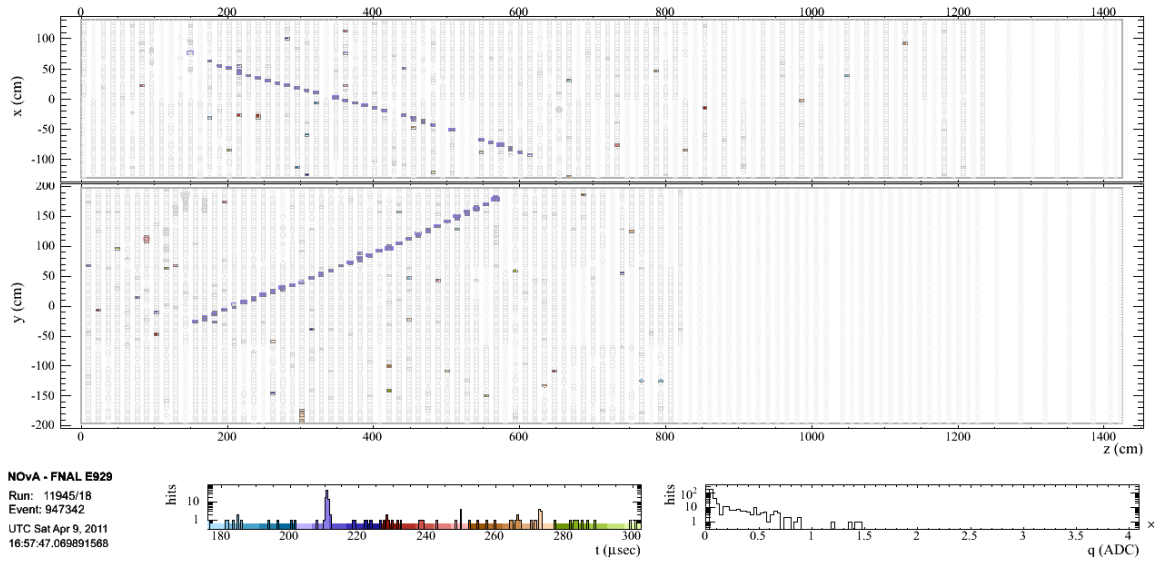

Figure 5.1: Event display to show the coordinate system used in the analysis. For the x coordinates $|x_1| < 115cm$, for the y coordinate $|y_1| < 150cm$; and the z coordinate changes for each detector configuration, for configuration 1 we use $50cm > z_1 < 770cm$ and for configuration 2 we use $300cm > z_1 < 500cm$.

Interactions	QE	RES	DIS	NC
Fiducial cut	100%	100%	100%	100%
Cosmic cut	86%	85%	82%	72%
One track	78%	46%	21%	42%
Fully contained	30%	20%	8%	30%

Table 5.1: Percent of the events after each pre-selection cut.

This algorithm estimates a multidimensional probability density function by counting the number of signal and background events from a set of simulated training events in the parameter space near the event. The kNN finds the k nearest events from the training set for each test event:

$$k = k_S + k_B, \tag{5.3}$$

where k_S is the number of the signal events, and k_B is the number of the background events in the training sample. The relative probability that a test event is of signal type is given by

$$P_S = \frac{k_S}{k_S + k_B} = \frac{k_S}{k}. \tag{5.4}$$

The kNN searches for k events that are closest in a defined set of parameters to the test event. The closeness is measured using the Euclidean distance

$$R = (\sum_{i=1}^{n_{var}} |x_i - y_i|^2)^{\frac{1}{2}}, \tag{5.5}$$

where n_{var} is the number of input parameters used for the classification, x_i are the parameters of an event from a training sample and y_i are parameters of an observed test event [72]. The k events with the smallest values of R are the k-nearest neighbors. A value of k determines the average size of the neighborhood over which probability density functions are evaluated.

Figure 5.2 illustrates event classification with the k-nearest neighbor algorithm. The number of training events has been reduced to illustrate the principle of the algorithm.

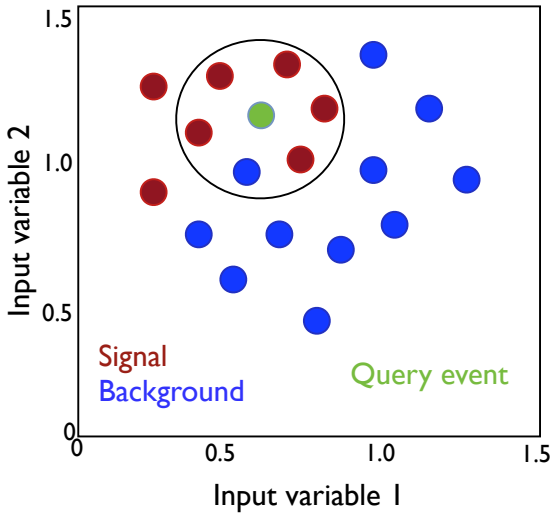

Figure 5.2: Example of KNN classification. Signal is shown in red and background is shown in blue and the query event with green. A neighborhood enclosing the 6 nearest neighbors is shown with the black circle. The KNN searches for 6 nearest points in the nearest neighborhood (circle) of the query event. The nearest neighborhood counts 5 signal and 1 background points so that query event may be classified as a signal candidate.

We use three different parameters as an input to the kNN: (1) number of planes that the track crosses, (2) ratio of mean energy (PECorr) per plane to track length in plane and (3) the energy (PECorr) within a 50 cm radius of the vertex, including muon track hits.

We use simulated $(\nu_\mu + \bar{\nu}_\mu)$CC QE events as the signal sample while we use the simulated CC resonance, deep inelastic, electron neutrino $(\nu_e + \bar{\nu}_e)$, and NC interactions as the background sample. We train the kNN using the three input parameters and later evaluate the kNN using a different MC sample and the Near Detector Prototype Data.

5.1.3 Training Sample for kNN

Events used for the kNN training and testing sample are subjected to the pre-selection cuts given in section 2.1. In addition, we include additional cuts in the training sample to include short track length events with a single proton track in the final state as background events. The additional cuts are used to classify those events as background in the training sample. The cuts include the following:

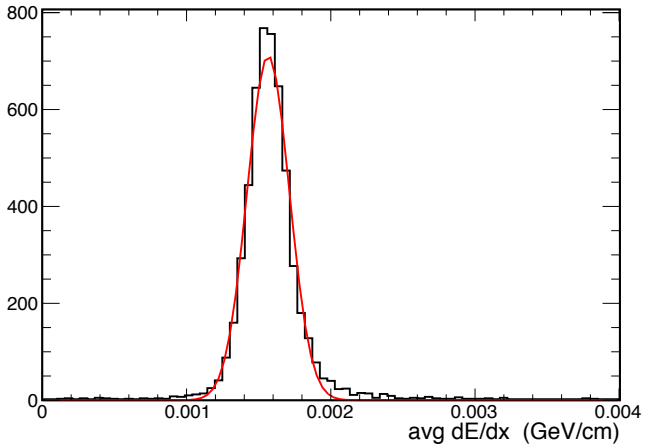

Figure 5.3: Average of $\frac{dE}{dx}$ for muons, black is simulation and red is a curve from a fit. Plot taken from [73]

1. For the training we selected events with a bragg peak at the end of the track as background. The variable is made using the energy deposited as a function of the length dx at the end of the track. The threshold used is $dE/dx > 52MeV$. This threshold is set to avoid the rejection of muons with a Michel electron.

2. Require the $\frac{dE}{dx}$ to be consistent with a minimum ionizing particle for any track. The threshold is determined using the average of $\frac{dE}{dx}$ for muons. Figure 5.3 shows the average $\frac{dE}{dx}$ for muons using simulations. We cut events outside of $\frac{dE}{dx} \pm 3\sigma$, $(0.001 < \frac{dE}{dx} < 0.0025)GeV/cm$.

The justifications for the event parameters used to build the kNN are:

- Number of planes in the reconstructed track. This separates neutral current events from charged current events. Figure 5.4 shows the difference between neutral current events and charged current events. The pions from neutral current events tend to travel through fewer planes than muons from charged current interactions.

- Mean energy deposition per plane (PECorr) in the reconstructed track normalized by the track length. Neutral current events tend to deposit more energy per plane than charged current events. The distribution is shown in figure 5.4. The motivation for this variable come from $< dE/dx >$ but we found Data-MC discrepancies for this variable and found the $< dE/dx > /(tracklength)$ have better Data-MC agreement.

- Energy around the vertex, the PECorr energy is added for all the cells around the vertex using a radius of 50 cm from the reconstructed vertex position. The figure 5.4 shows the PECorr energy around the vertex. The CC QE events have less energy around the vertex compared with other type of neutrino interactions.

After training and testing the kNN with different MC samples, the output kNN is shown in figure 5.5. The signal and each component of the background are shown. The red curve is from CC QE interactions, the blue CC resonance interactions, the pink CC deep inelastic interactions and the green the NC interactions.
To optimize the cut for the kNN, we chose the maximum figure of merit (FOM) defined as:

$$FOM = \frac{Signal}{\sqrt{Signal + Background}}. \tag{5.6}$$

The figure 5.6 shows the signal purity, signal efficiency, the signal times the purity and the significance (value of the FOM) as a function of each value of the kNN output. The maximum significance and signal times purity is shown in this plot. The optimized kNN cut was chosen to be $kNN > 0.35$, using the criterion of having the maximum FOM . This selection produces a signal efficiency of 85% and a purity of about 60%.

Now, having the algorithm trained to select the CC QE events using the MC, we apply the same techniques in the Data collected from the Near Detector Prototype. The next section shows the Data input variables and the kNN selector used to select the CC QE events. In addition, we will show the scattering angle and momentum prediction that will be used to compute the neutrino energy for the selected CC QE events.

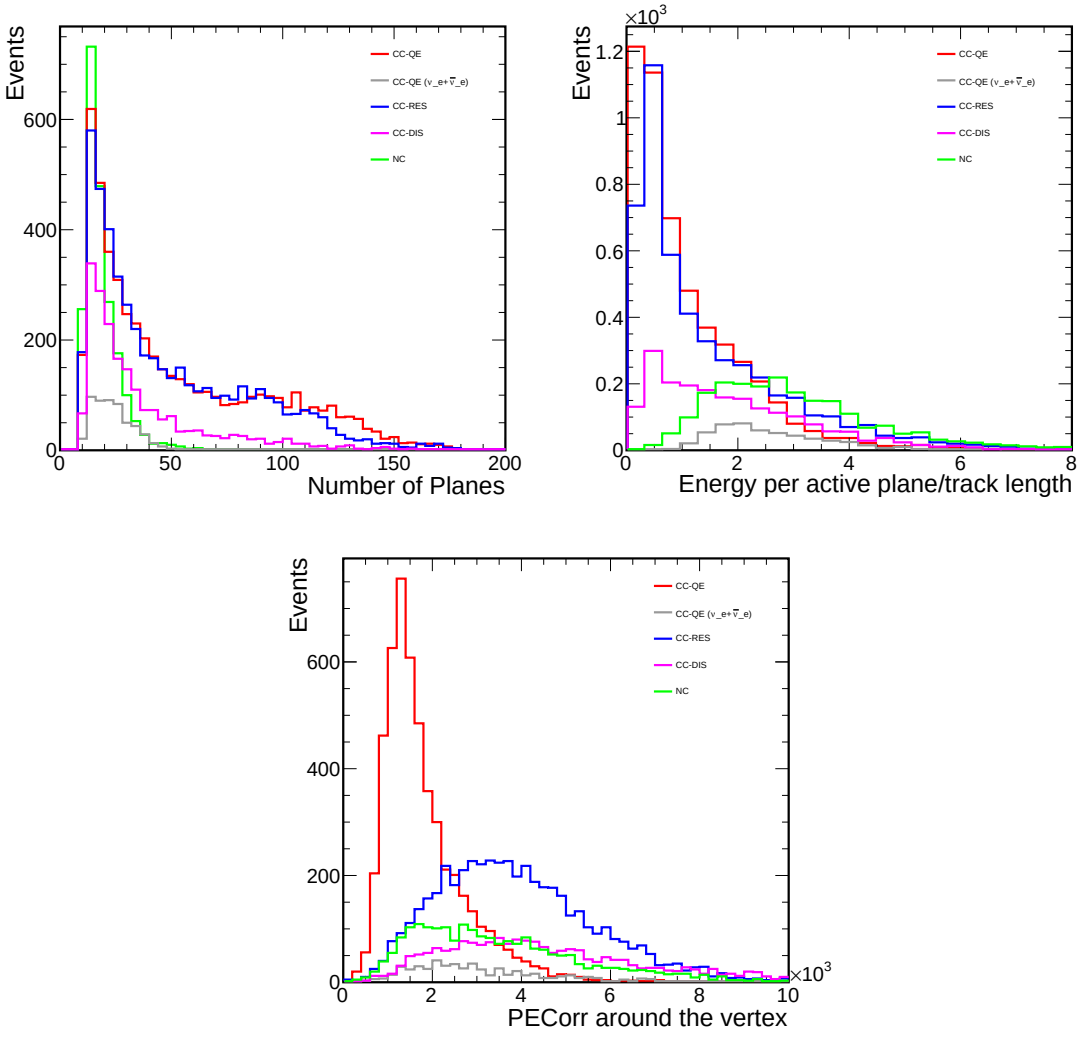

Figure 5.4: Number of planes in the reconstructed track, ratio of mean energy per active plane to track length (PECorr)/cm, and PECorr energy around the vertex, taking a radius of 50 cm around the vertex. The red represent the CC QE interactions, the blue the CC RES interactions , the pink the CC DIS interactions and the green the NC interactions.

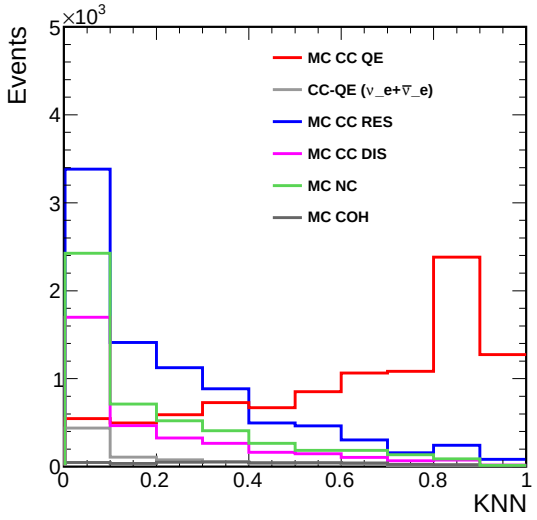

Figure 5.5: kNN output for a different Monte Carlo sample than that used to train the kNN. The different curves represent each interaction type using the truth from the simulations. The red represent the CC QE interactions, the blue the CC RES interactions , the pink the CC DIS interactions and the green the NC interactions. The horizontal axis is the kNN result and the vertical axis is the number of events in the sample

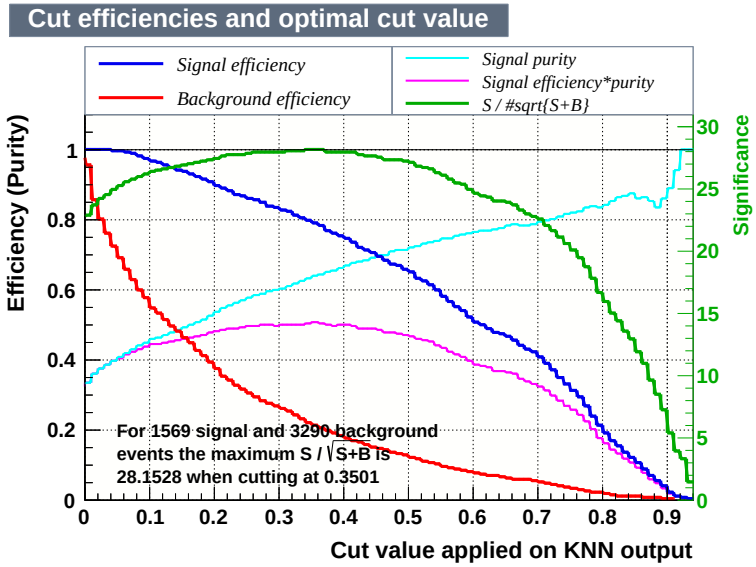

Figure 5.6: Efficiency for the signal and background as a function of the kNN output. The dark blue represent the signal efficiency, the red the background efficiency and the purity for signal is shown in light blue color. In addition the significance (FOM) is shown in green color and the signal efficiency times purity is shown in pink color.

5.2 Events after Pre-selection and Cosmic Ray Background

Using the preselection cuts over the Data, we find a sample of beam events plus cosmic ray background. Since the beam MC simulation does not contain the cosmic ray background, we make a prediction for the cosmic ray background using the out of time Data and subtract this background from the total sample.

The cosmic ray background prediction is determined using the events outside the spill window. We use the pre-selection cuts for these events and time normalized the distributions. This Data is outside the spill beam window from 0 to $217\mu s$ and from $227\mu s$ to $500\mu s$. Figure 5.7 shows events within 50 cm radius of the vertex, number of planes and ratio of mean energy per plane to track length for the beam candidates and cosmic ray background for preselected events.

5.3 Data-MC Selection

Figure 5.8 shows the input parameters to the kNN in Data and MC simulations for the events after pre-selection cuts for the configuration 2. This Data set correspond to 1.7×10^{20}POT. The distributions show Data after cosmic ray background subtraction.

Evaluating the input parameters: number of planes, ratio of mean energy per active plane to track length and the energy around the vertex for Data and MC a kNN selector is built. Figures 5.8 shows the comparisons of the Data and with the MC simulations. In the distributions on the left, the Monte Carlo has been normalized to the Data (area normalized) while on the right it has been normalized to have the same POT as the Data. For the POT normalized plots the statistical errors are calculated from Gaussian, if the bin contains less than 10 events, Poisson statistics. The shapes of the Data and Monte Carlo distributions are generally in good agreement but there is a discrepancy in absolute normalization. The χ^2 and NDF is shown in table 5.2 for the area and POT normalized plots.

Figure 5.9 shows the kNN output used to select events.

	χ^2/NDF (Area normalized)	χ^2/NDF (POT normalized)
Number of planes	11.6/14	44.1/14
Mean energy	10.7/19	42.9/19
Vertex energy	10.9/9	41.5/9

Table 5.2: χ^2 and NDF for area and POT normalized plots from figure 5.8

The CC QE selection requires both the pre-selection cuts and the PID selector, ($kNN > 0.35$).

Data-MC distributions of parameters not directly used in the selection process are shown

in figure 5.11 for events selected as QE events and the cosmic ray background prediction. The Figure 5.12 shows the scattering angle of the tracks with respect to the beam direction compared to the Monte Carlo prediction. The left distribution is area normalized and right distribution is POT normalized. Figure 5.13 shows the momentum of the CC QE selected events for Data and MC, where the momentum is determined from the length of the tracks. Again, figures 5.12 and 5.13 show that the behavior of these parameters is consistent with the Monte Carlo but the absolute normalization is not. A study of POT accounting was made using the Monte Carlo simulations to fix the POT accounting [74]. This correction is used in this analysis. Table 5.3 shows a summary of the events after each cut for Data, cosmic ray background and MC events. The MC events have been scaled by POT.

	In time Data	Cosmic Data	Subtracted-Data	MC
Fiducial cut	11459	9194	2265	3679
Cosmic ray cut	2845	757	2088	3066
One track	1841	612	1229	1769
Track Length $>$ 60 cm	1715	558	1157	1661
Fully contained	513	64	449	642
PID cut ($kNN > 0.35$)	214	24	190	263

Table 5.3: Events after each pre-selection cut and PID cut in Data and MC.

The kNN distribution, figure 5.9, shows good agreement between Data and MC, except perhaps for the first bin. A study was made using scanning to determine the origin of this discrepancy and we found those events are coming from short track length NC events. The Monte Carlo predicts more short track length than Data. We plot a comparison of Data and MC including the systematic uncertainties in figure 5.10. The systematic uncertainties for the background events will be discussed in Section 9. We note that the same disagreement between Data and Monte Carlo occurs in configuration 1 as shown in Appendix A.

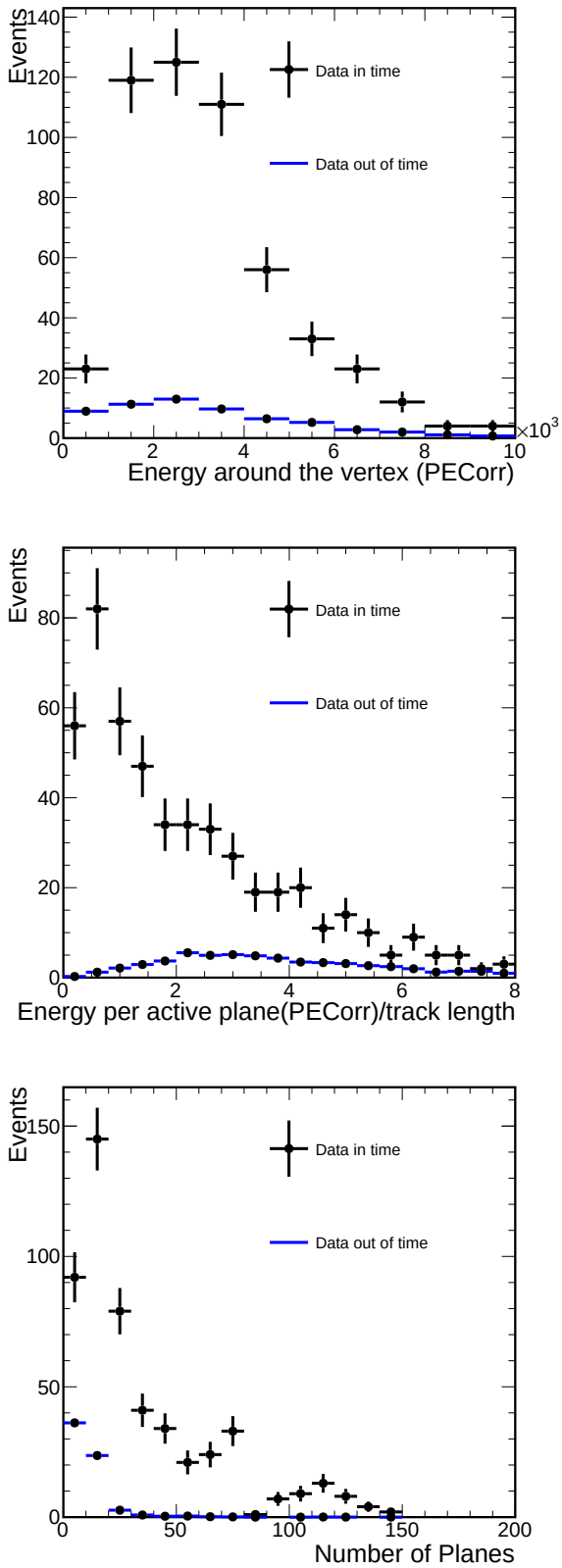

Figure 5.7: Top: Energy within a 50 cm radius from the vertex (PECorr). Middle: ratio of energy per active plane to track length. Bottom number of planes. Distributions show the beam candidates in black and cosmic ray background in blue for preselected events in configuration 2.

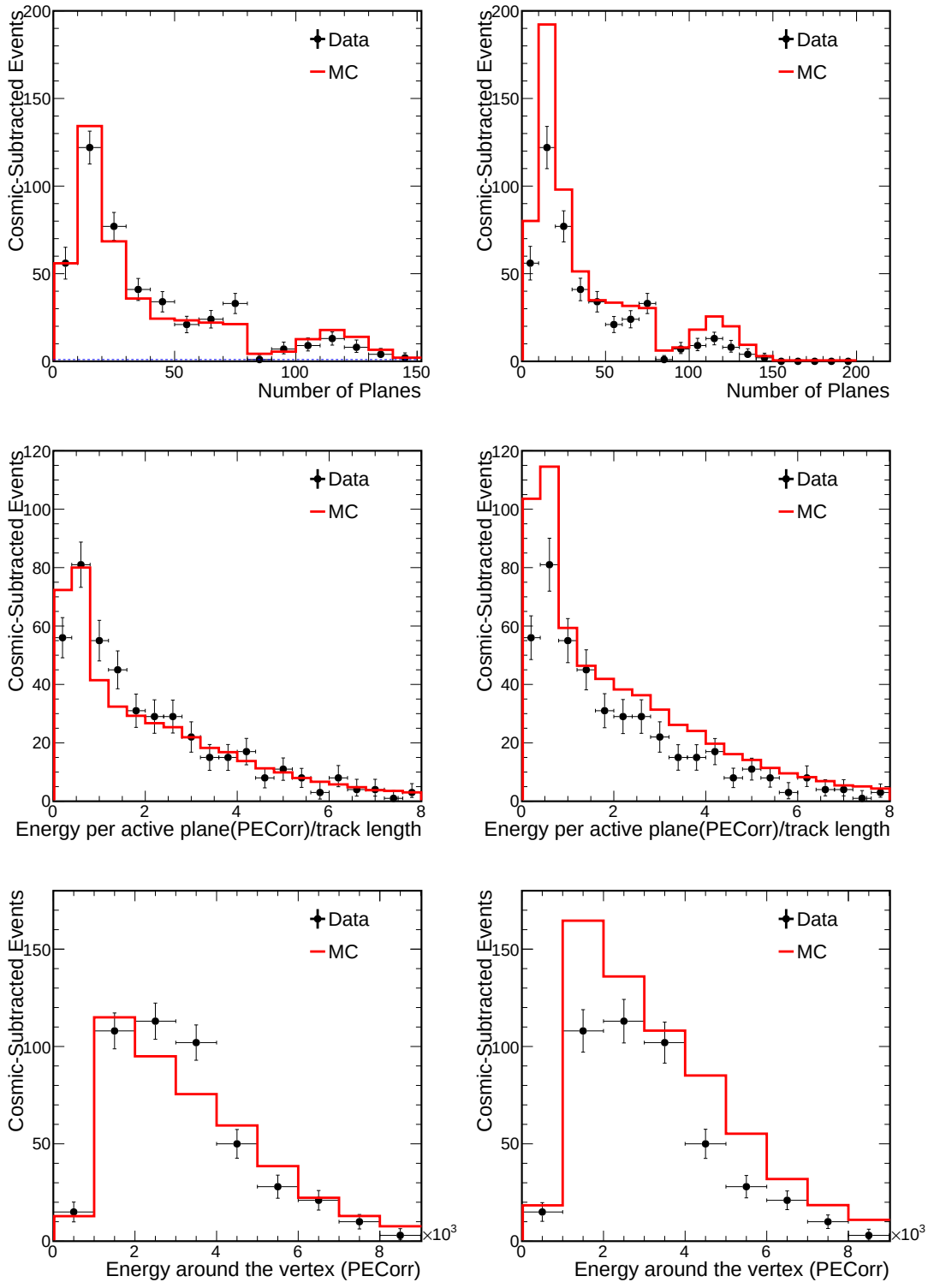

Figure 5.8: The top plots show the comparison of number of planes. Middle plots show comparison of the ratio of mean energy per active plane to track length and bottom plot the comparison of the energy around the vertex. All plots show a comparison of the Data for pre selected events (black) to the Monte Carlo (red) of QE plus background subjected to the same selection criteria as the Data for each parameter used in the kNN event selector. The left hand set of graphs are area normalized and the right hand set are normalized to protons on target (POT). All distributions are for configuration 2.

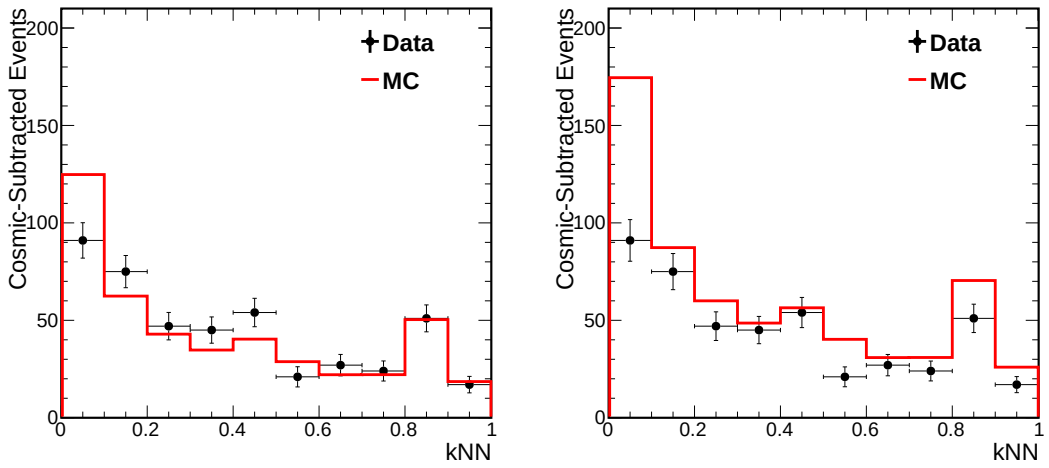

Figure 5.9: k-Nearest Neighbour classifier (kNN) for Data and Simulations for configuration 2. Left: kNN area normalized. Right: kNN POT normalized.

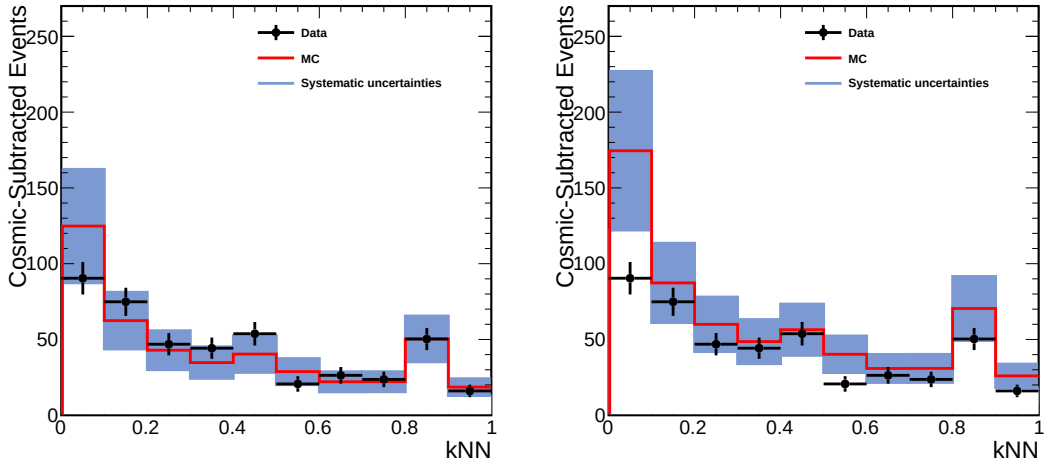

Figure 5.10: Comparison of k-Nearest Neighbour classifier for the beam candidates after cosmic ray background subtraction and Monte Carlo simulations for pre-selected events in configuration 2. The error band in blue corresponds to the systematic uncertainty from the background, flux and other systematics evaluated in the analysis.

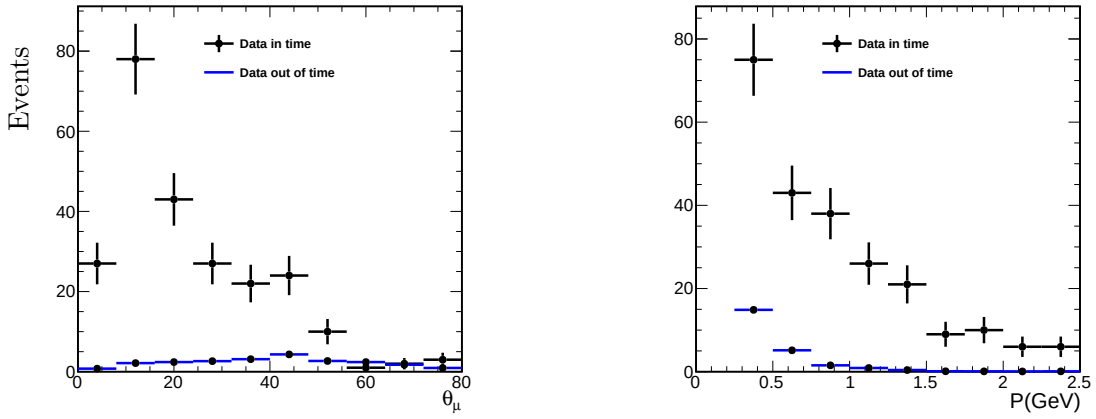

Figure 5.11: Neutrino candidates and cosmic ray background prediction for configuration 2. Data in time is the beam plus cosmic ray background and out of time is cosmic ray only.

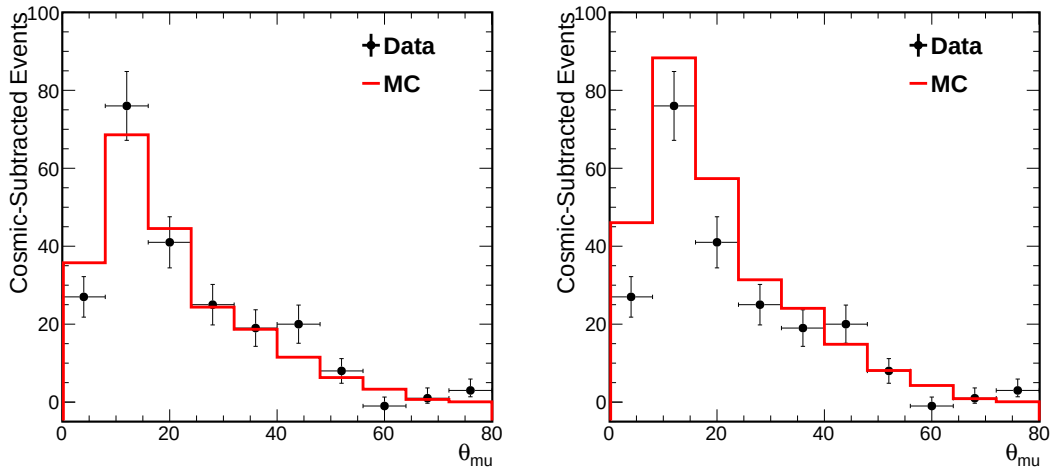

Figure 5.12: Comparison of the scattering angle for ν_μ CC QE selected events after cosmic ray background subtraction and MC simulation. Left: MC normalized to Data. Right: POT normalized.

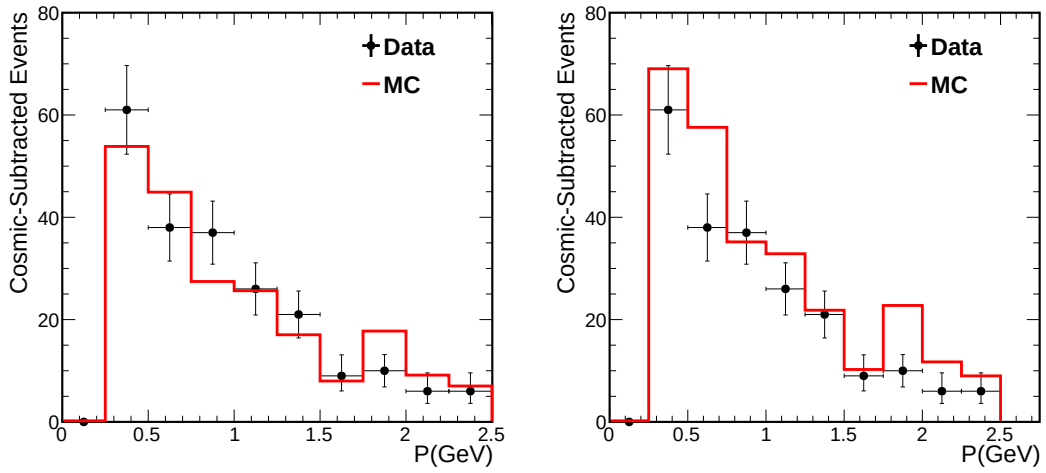

Figure 5.13: Comparison of momentum for ν_μ CC QE selected events after cosmic background subtraction and MC simulation. Left: MC normalized to Data. Right: POT normalized.

5.3.1 Background Study

To study background, we used the same pre-selection cuts as the Data except we required events to have two 3D reconstructed tracks. Figure 5.14 shows the MC for each of the background contributions. Note that the fraction of QE signal events in this sample is less than 5%. We use the longest track to determine the energy and compute the four momentum transfer.

Figure 5.15 shows the neutrino energy and figure 5.16 shows the four momentum transfer distributions from Data and MC simulations.

This two track sample is background dominated, the biggest background contribution is from resonance interactions. The plot in figure 5.16 shows the comparison of Data and MC simulation for two track events. The MC has been normalized to the number of events from Data. The Data-MC area normalized comparison shows the two track Data is statistically consistent with MC simulation which is background dominated.

We have studied the two track selected sample to explore the possibility of constraining the background in the single track selection sample. Using the two track sample as follows

$$N_{background}(1track) = \frac{N_{MC-1track}}{N_{MC-2track}} N_{Data(2tracks)}. \tag{5.7}$$

To evaluate if the two track sample could be used to estimate the background, we determine the systematic uncertainty for this sample. The figure 5.18 shows the ratios of each of the systematic uncertainties to the nominal MC, in the left distribution for the one track sample (CC QE selection) and the right distribution for the two track selected sample. We use

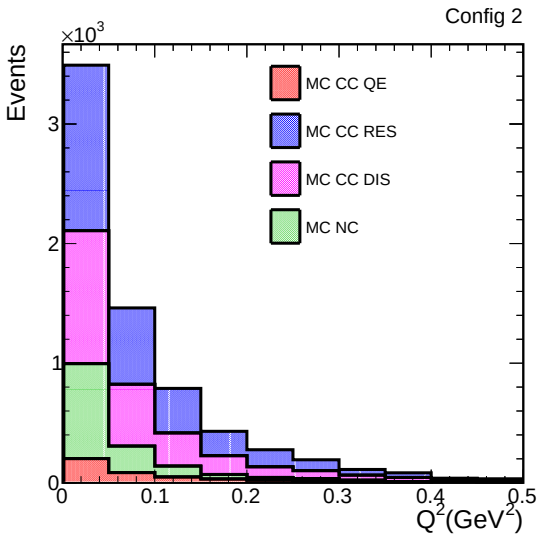

Figure 5.14: Square four momentum transfer for events with 2 reconstructed tracks. The plot shows the Monte Carlo prediction of the event composition

the GENIE reweighting tools to find the cross section model uncertainties for each of the background RES, DIS, NC and COH [94]. Also, we determine the uncertainties from the intranuke parameters.

The total systematic uncertainty for the two track sample is obtained adding each of the uncertainty in quadrature for each bin. Figure 5.17 shows the total systematic uncertainty for the two track selected sample. Since the total systematic uncertainty is much bigger than the systematic uncertainty for the CC QE selected sample, (section 7.3 shows details about the systematic for the selected CC QE events). The physics modeling of the two-track selected sample is different compared with the one track sample and cannot be used to predict the background in the CC QE selected sample. However, we find Data-MC simulations has good shape agreement for the two track selected sample and use this sample to check our MC simulation.

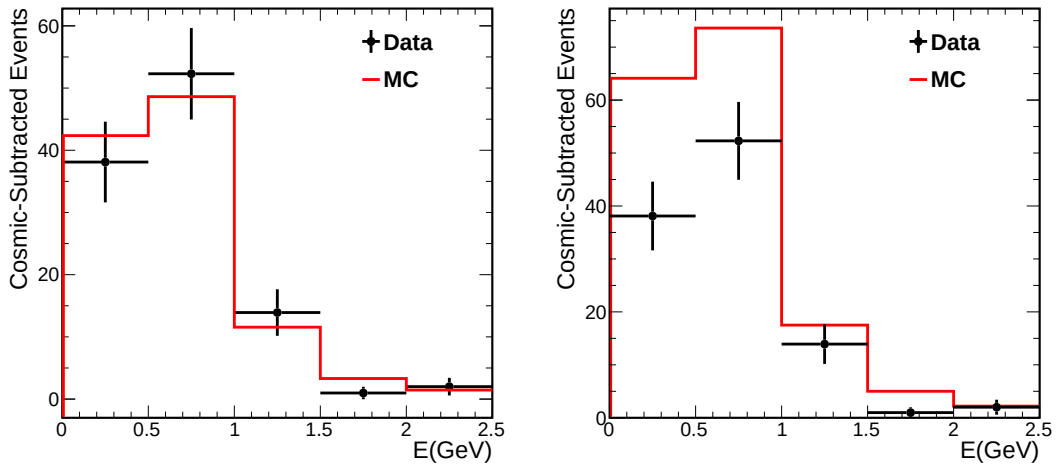

Figure 5.15: Neutrino Energy for events with two 3D reconstructed tracks. Left: Data and Monte Carlo simulation comparison area normalized. Right: POT normalized.

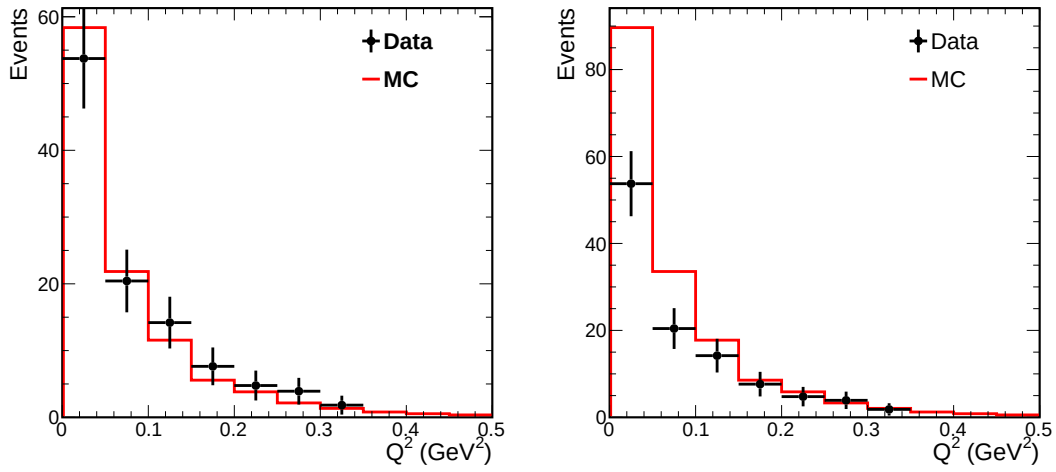

Figure 5.16: Square four momentum transfer for events with 2 reconstructed tracks. Left: The distribution shows Data and Monte Carlo simulation comparison area normalized. Right: POT normalized.

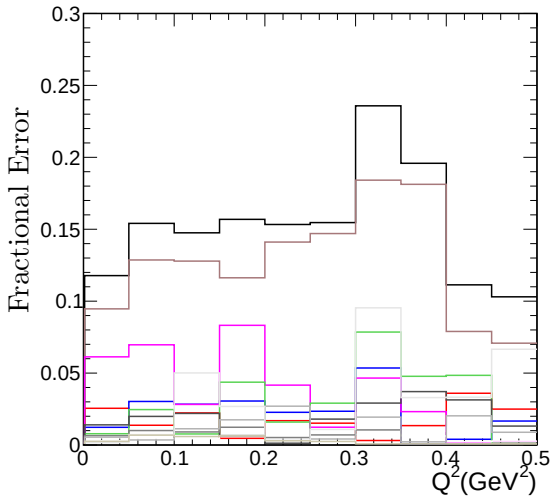

Figure 5.17: Fractional uncertainty as a function of the Q^2 distribution. Black is the total uncertainty, individual uncertainties have been added in quadrature bin by bin.

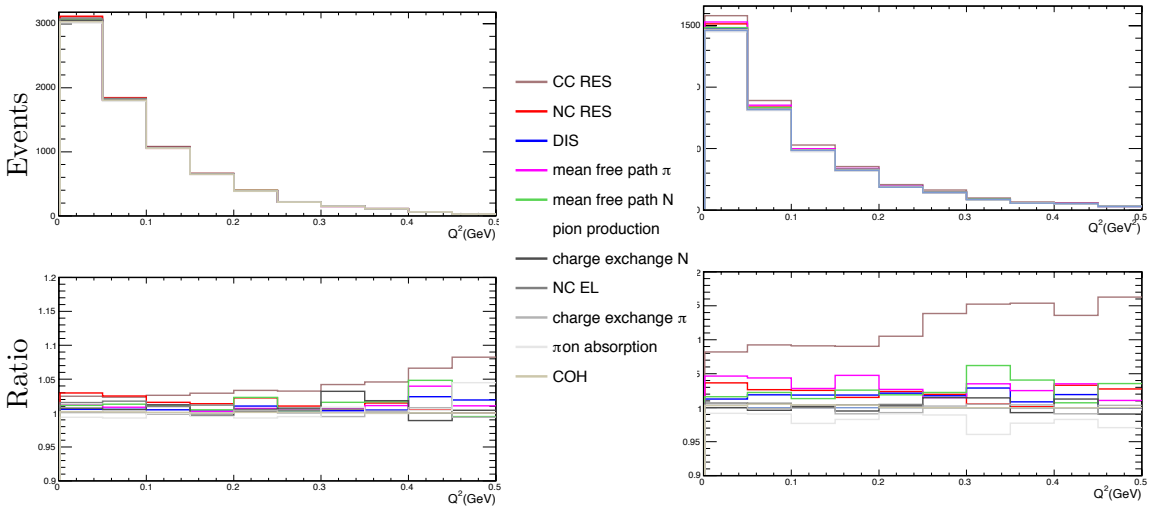

Figure 5.18: Left :Ratios of the one sigma prediction to nominal MC simulation for each of the systematic for the CC QE selected events. Right: Ratios of the one sigma prediction to nominal MC for the two track selected sample.

5.4 Neutrino Energy and Four Momentum Transfer Reconstruction

The neutrino energy is reconstructed using the kinematics of the event, the scattering angle and momentum prediction, where the momentum is determined from the length of the track, Appendix B describes the method to obtain the momentum. These variables are shown in figures 5.12 and 5.13. The neutrino energy is obtained using

$$E_\nu = \frac{2(M_n^{'})E_\mu - ((M_n^{'})^2 + m_\mu^2 - M_p^2)}{2[(M_n^{'}) - E_\mu + \sqrt{E_\mu^2 - m_\mu^2}\cos\theta_\mu]} \tag{5.8}$$

where $E_\mu = T_\mu + m_\mu$ is the total muon energy, M_p is the proton mass, m_μ is the muon mass and $M_n^{'}$ is the adjusted neutron mass: $M_n^{'} = M_n - E_B$, where E_B is the binding energy $(E_B = 25MeV)$[95].

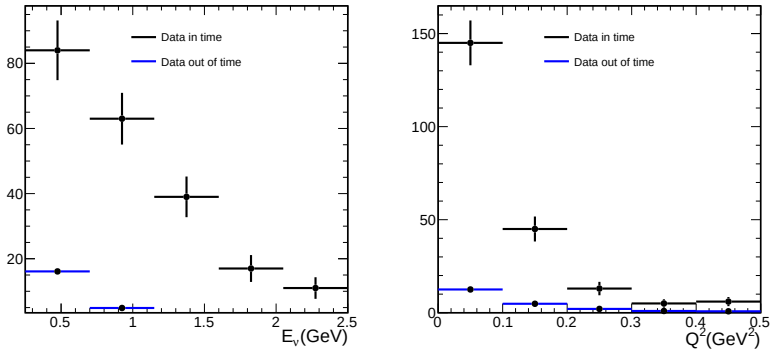

Figure 5.19: Left: Neutrino energy for the ν_μ CC QE selection. Right: Q^2 for the ν_μ CC QE selection. Data in time is the beam plus cosmic ray background and out of time is the cosmic ray only for configuration 2.

Four momentum transfer is obtained using:

$$Q^2 = -m_\mu^2 + 2E_\nu(E_\mu - \sqrt{E_\mu^2 - m_\mu^2}\cos\theta_\mu) \tag{5.9}$$

Figure 5.19 shows the neutrino energy and the four momentum transfer for the Data in time and Data out of time. In addition, figures 5.20 and 5.21 show Data-MC simulation comparisons for the neutrino energy and the four momentum transfer for the Data collected from the configuration 2 forward horn current neutrino run. Distributions shown in figures 5.20 and 5.21 are area normalized on the left and POT normalized on the right. Doing a χ^2 test for the neutrino energy distribution in figure 5.20 for the area normalized distributions we obtain $\chi^2 = 3.7, NDF = 2$. Now doing the χ^2 test for the POT normalized plot we obtain $\chi^2 = 13.5, NDF = 3$.

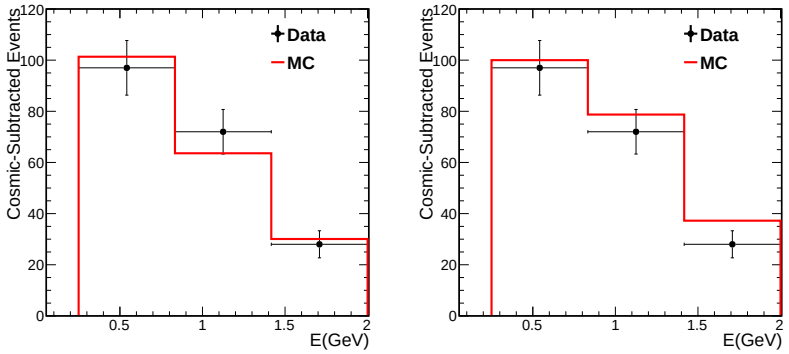

Figure 5.20: Comparison of reconstructed neutrino energy for ν_μ CC QE selected events after cosmic ray background subtraction from data and MC simulation, that includes both QE signal and background. Left: MC normalized to Data. Right: POT normalized.

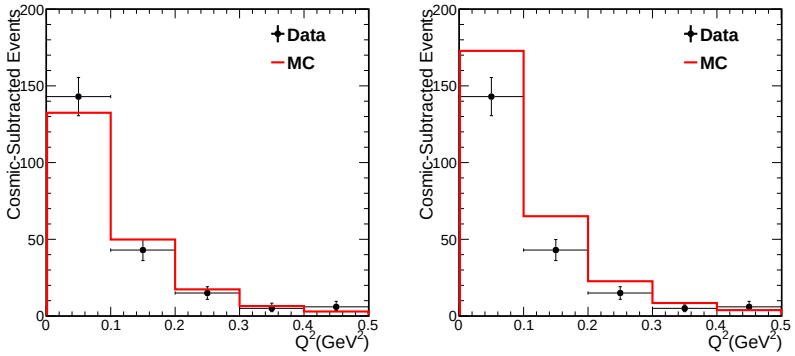

Figure 5.21: Comparison of square four momentum transfer for ν_μ CC QE selected events after cosmic ray background subtraction for data and MC simulation. Left: Four momentum transfer area normalized. Right: Four momentum transfer POT normalized for configuration 2.

Table 5.4: Expected signal and background events from the MC simulations.

configuration	CC-QE ν_μ	CC-QE $\bar{\nu}_\mu$	CC RES	CC DIS	NC	COH	CC-QE ν_e	Total
configuration 1	27	11	11	4	5	1	2	59
configuration 2	131	49	49	16	25	5	4	280

5.4.1 Irreducible Background

The CC QE selection for the Near Detector Prototype detector contains irreducible background. The components of this background are shown in figure 5.22 and 5.23 for configuration 2. Using the MC simulations, the expected number of signal and background events are shown in table 5.4 for both configurations. The current Data selection criteria give 230 neutrino candidates with 20 cosmic ray background events for configuration 2 and 55 neutrino candidates with 11 cosmic ray background events for configuration 1. The distributions for configuration 1 are shown in appendix B.

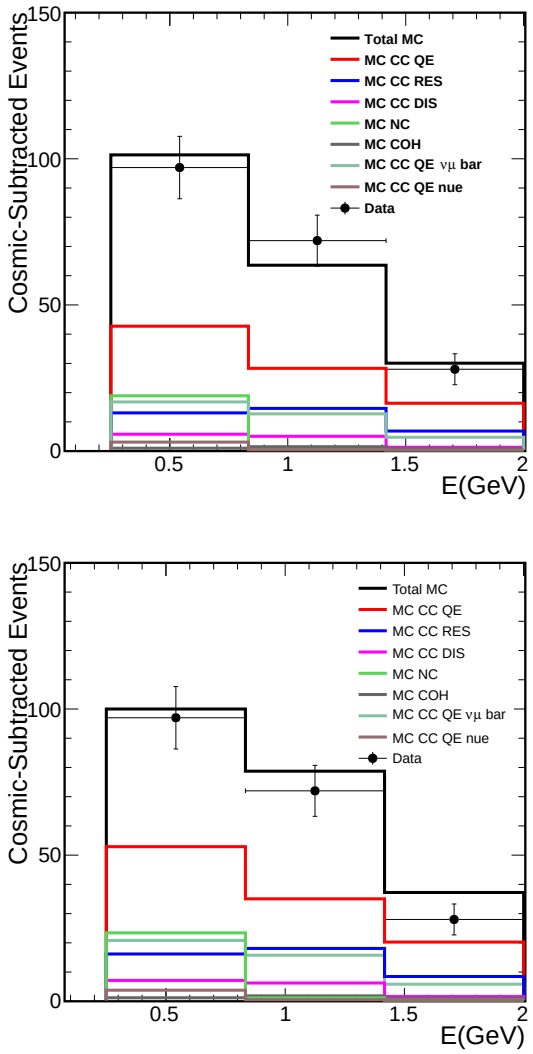

Figure 5.22: Comparison of reconstructed neutrino energy for ν_μ CC QE selected events after cosmic ray background subtraction and the MC simulation that includes non cosmic background. The background contribution for each type of interaction is shown. Top: area normalized, Bottom: POT normalized.

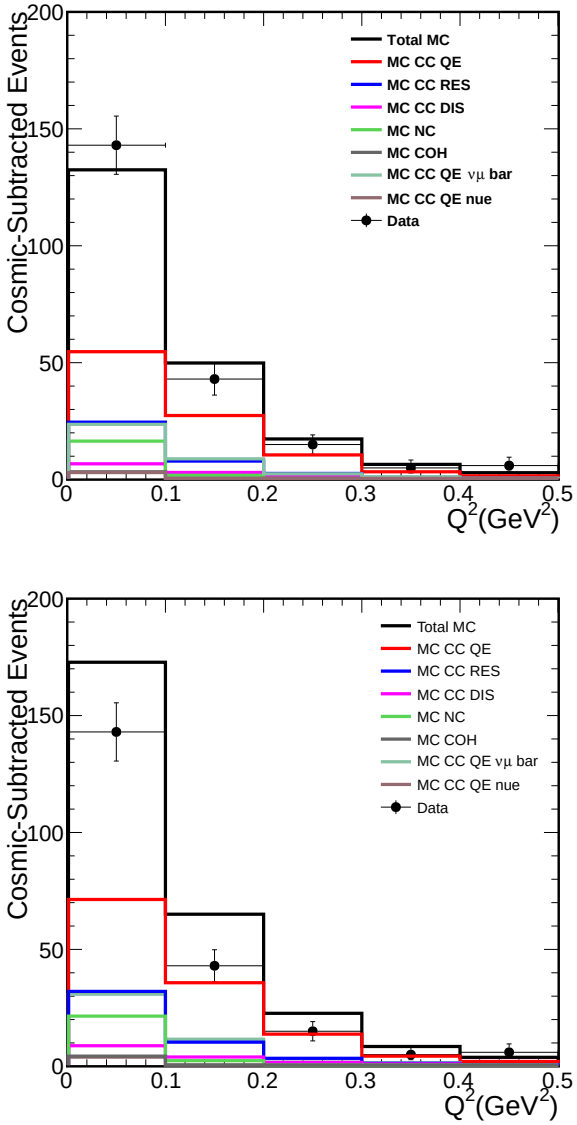

Figure 5.23: Comparison of the four momentum transfer square for ν_μ CC QE selected events after cosmic ray background subtraction with the simulation which includes all backgrounds. Also shown is the MC simulation for each of the interaction contributions. The top distribution is area normalized to the Data and the bottom distribution is POT normalized.

Chapter 6

Analysis

6.1 Cross Section definition

Consider a target, at rest, with a given number of target nucleons. Aim at this target a beam of neutrinos with a flux ϕ. Then we expect the total number of scattering events N^{int} to be proportional to the effective cross-sectional area of each target, the number of targets T and the flux ϕ as

$$dN^{int} = T\sigma d\phi. \tag{6.1}$$

The cross section measurement can be made as a function of any quantity that affects either the interaction, such as the neutrino energy, or the consequences of the interaction such as the muon momentum. Review taken from [96]. We can write equation 6.1 as a function of the initial quantities $\vec{a} = a_1..a_L$ and the final quantities $\vec{b} = b_1..b_N$. The total number of interactions is then just the integral over all of those quantities.

$$N^{int} = T \int_{a_1} .. \int_{a_M} \int_{b_1} .. \int_{b_N} \frac{\partial^N \sigma(\vec{a},\vec{b})}{\partial b_1..\partial b_N} db_1..db_N \frac{\partial^M \phi(\vec{a})}{\partial a_1..\partial a_M} da_1..da_M \tag{6.2}$$

If one desires to express the cross-section in terms of the final state variables, we need to integrate over all the initial states.
For simplicity, consider only a single initial state variable a and final state b. By definition, the flux averaged cross section is given by integrating over the range of the variable a:

$$< \sigma >_\phi = \frac{1}{\phi} \int_a \sigma(a,b) \frac{\partial \phi}{\partial a} da. \tag{6.3}$$

The total number of interactions in bin j of the final state variable b becomes

$$N_j^{int} = T\phi \int_{b_j} < \frac{\partial \sigma}{\partial b} >_\phi db \tag{6.4}$$

where 6.1 has been applied to $\frac{\partial\sigma}{\partial b}$. The flux averaging is independent of the final state derivatives , and equation 6.1 is equivalent to

$$N_j^{int} = T\phi \int_{b_j} \frac{\partial < \sigma >_\phi}{\partial b} db. \tag{6.5}$$

The flux average differential cross section is then given by

$$< \frac{\partial\sigma}{\partial b} >_j = \frac{N_j^{int}}{T\phi\Delta b_j} \tag{6.6}$$

where Δb_j is the bin width and $\sigma =< \sigma >_\phi$. Using this definition we can compute the flux average differential cross-section for the four momentum transfer, angle and momentum as

$$< \frac{\partial\sigma}{\partial Q^2} >_j = \frac{N_j^{int}}{T\phi\Delta Q^2}, \quad < \frac{\partial\sigma}{\partial T_\mu} >_j = \frac{N_j^{int}}{T\phi\Delta T_\mu}, \quad < \frac{\partial\sigma}{\partial \cos\theta} >_j = \frac{N_j^{int}}{T\phi\Delta\cos\theta}. \tag{6.7}$$

The flux average total cross section per nucleon is given by

$$< \sigma >_\phi = \frac{N^{int}}{T\phi}. \tag{6.8}$$

In the next section we will use these definitions.

6.2 Cross section calculation

The cross section is calculated using the experimental definition:

$$\sigma_i = \frac{\sum_j U_{ij} N_{QEi}}{\varepsilon_i \phi_i T}, \tag{6.9}$$

where U is the unfolding matrix to account for the resolution of reconstructed events as a function of energy and four momentum transfer. N_{QE} are the selected CC QE events, ε is the efficiency and T is the number of targets.

For the cross section as a function of energy $\sigma(E)$, the flux is divided into energy bins and for the flux integrated cross section $\frac{d\sigma}{dQ^2}$ the flux is integrated across all bins $\phi = \sum_i \phi_i$.

The following sections describe the procedures used to calculate the cross section: (6.2.1) number of target neutrons, (6.2.2) background subtraction and efficiencies, (6.2.3) unfolding procedure. It also presents the summary of cross section uncertainties (7) and, finally, the results.

6.2.1 Number of Neutron Targets

We determine the number of target neutrons using the mass of the detector and its composition [75].

The mass is calculated using the total PVC and the total scintillator mass for the detector.

Table 6.1 shows the total mass of the PVC and scintillator. This Data comes from nova-db 1136 [76].

Using the mass and volume of the total detector, the neutrino interaction fiducial mass is calculated:

$$\frac{m_F}{V_F} = \frac{m_T}{V_T}. \tag{6.10}$$

Table 6.2 shows the fiducial mass of PVC and scintillator for both configurations of the Prototype Detector.

Detector mass	(tons)
Total detector PVC mass	38.3
Total detector scintillators mass	91.3
Muon catcher PVC mass	2.7
Muon catcher scintillator mass	6.3
Total steel mass	95.71
Total	225

Table 6.1: Total Detector Mass[76].

	PVC(tons)	scintillator(tons)
Configuration 1	14.9	35.6
Configuration 2	4.1	10.0

Table 6.2: Interaction region fiducial mass for the PVC and scintillator.

The number of neutrons is calculated using:

1. The molar weight of each of the components.
2. Dividing the detector mass by the molar weight.
3. Calculating the number of molecules by multiplying the number of moles by Avogadro's number.
4. Multiplying the molecules by the number of neutrons per molecule.

Using the mass fraction and the procedure described above, the number of neutrons are calculated for each element. Table 6.3 shows the numbers for each element in the NOνA Prototype Detector for configuration 1. The total number of neutrons for this configuration is 1.3566×10^{31} and the total number of neutrons for the configuration 2 is 3.768×10^{30}.

6.2.2 Background Subtraction and CC QE sample

The selected CC QE events contain a background coming from single track events that are not QE. For example, scanning studies show about 20% of the charged current resonance

Table 6.3: Number of Neutrons for each component of the Near Detector Prototype fiducial region for configuration 1.

Composition	Mass Fraction	Mass(ton)	Molecules	# Neutrons
Scintillator				
CH_2	94.64%	33.7	1.4e30	8.7e30
C_9H_{12}	5.23%	1.86	9.3e27	5.0e29
$C_{15}H_{11}NO$	0.139%	0.049	1.3e26	1.4e28
$C_{24}H_{22}$	0.0016	5.7e-4	1.1e24	1.6e26
PVC				
C_2H_3Cl	80%	11.96	1.2e29	3.4e30
TiO_2	15%	2.2	1.7e28	7.1e29
$C_{36}H_{70}O_4Ca$	0.6%	0.09	9e25	2.4e28
$C_{20}H_{42}$	0.9%	0.14	2.9e26	3.4e28
$C_{12}H_{20}O_5$	0.2%	0.03	7.4e25	8.3e27
$C_{21}H_{42}O_4$	0.2%	0.03	5.0e25	7.9e27
$C_5H_8O_2$	3.1%	0.46	2.8e27	1.3e29

interactions have a single muon in the final state. In addition, short track length pions from neutral current background in which the dE/dx information is very similar to short track length muons are part of the background.

We use the MC simulation as described in section 5.4.1 to predict the background from charged current and neutral current interactions. The charged current backgrounds considered are resonance (RES), deep inelastic scattering (DIS), coherent scattering (COH) and ν_e interactions. These events are subtracted from both the Data and MC simulation. Table 5.4 gives the background contributions to the signal.

Neutrino Energy

The reconstructed energy for the CC QE selected events is shown in figure 6.1. This plot shows the background prediction in pink and the total MC in red for signal plus non cosmic background, ($(\nu_\mu + \bar{\nu}_\mu)CCQE$ as well as $\nu_e, \bar{\nu}_e$, RES, DIS and NC interactions). The Data has cosmic ray background, which is not in the MC, subtracted.

Subtracting the background prediction from both the Data and MC simulation produces the reconstructed neutrino energy distribution for the $(\nu_\mu + \bar{\nu}_\mu)CCQE$ events shown in figure 6.2.

Now, we have a sample of $(\nu_\mu + \bar{\nu}_\mu)CCQE$ events. In order to determine a cross section for the ν_μ CC QE events we use the ratio of ν_μ to $(\nu_\mu + \bar{\nu}_\mu)$ obtained from Monte Carlo to determine the contribution from ν_μ

$$R = \frac{\nu_\mu}{\nu_\mu + \bar{\nu}_\mu}, \tag{6.11}$$

where ν_μ and $\bar{\nu}_\mu$ are the events after the CC QE selection. The ratio as a function of

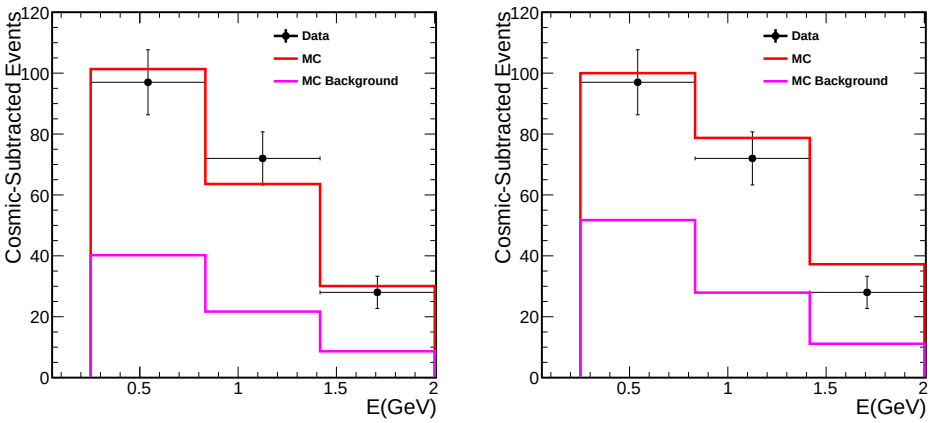

Figure 6.1: Comparison of reconstructed neutrino energy for ν_μ CC QE selected events after cosmic ray background. Data is shown in black and MC simulation is in red for signal plus the background from other neutrino interactions. The pink histogram is the MC background prediction. These distributions are taken from figure 5.20 with the background curve added. The left hand distribution has the MC area normalized to Data. The right hand distributions are POT normalized.

neutrino energy is shown in figure 6.3. The error bands are the systematic uncertainty from the π^+/π^- ratio in hadron production. Details about the systematic uncertainty introduced by this correction can be found in section 7.2.3. Using the ratio in the right hand plot of figure 6.3 and the background subtracted neutrino energy from figure 6.2 we extract the ν_μCC QE sample. Figure 6.2 is POT normalized and shows a discrepancy between Data and MC simulation in some bins.

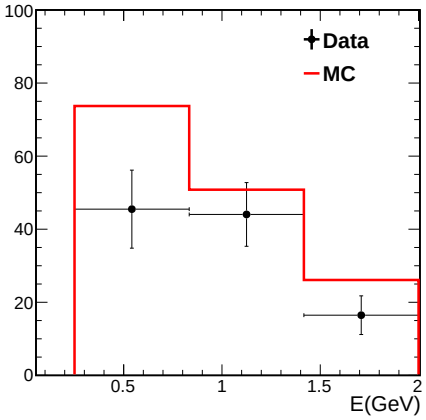

Figure 6.2: Comparison of reconstructed neutrino energy for ν_μ CC QE selected events after cosmic ray background and interactions background subtraction for Data and MC. Data and MC are POT normalized.

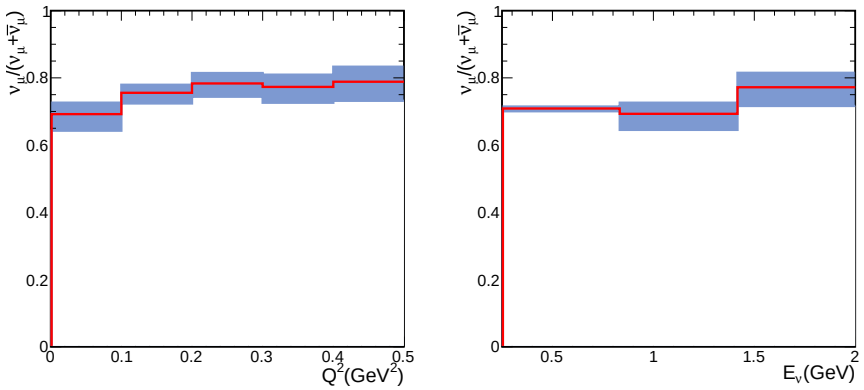

Figure 6.3: Left: Ratio of ν_μ to $(\nu_\mu + \bar{\nu}_\mu)$ as a function of reconstructed neutrino energy for the CC QE selected events from the Monte Carlo simulation. Right: Ratio of ν_μ to $(\nu_\mu + \bar{\nu}_\mu)$ as a function of four momentum transfer for the CC QE selected events. The error bands represent the systematic uncertainty of the $\bar{\nu}_\mu$ contamination, as described in section 7.2.3.

Four Momentum Transfer

We use a similar procedure as above for the background subtraction in the four momentum transfer square (Q^2) distribution. Figure 6.4 shows the four momentum transfer for the data ν_μ CC QE events and the MC simulation prediction. The pink distribution shows the irreducible background, from charged current (RES, DIS and COH) and neutral current interactions. The left hand plot is area normalized and the right hand plot is POT normalized. The POT normalized distribution shows disagreement between the Data and the MC simulations. To check the modeling of the background, a background data enhanced sample was studied in section 5.3.1 and showed good agreement between the shape of the Data and Monte Carlo.

Using the MC simulation prediction we subtracted the background from both the Data and MC simulation, the four momentum transfer after background subtraction is shown in figure 6.5. This figure shows that, although the shape of the distributions agree, there is a normalization disagreement between the Data and MC simulation.

To obtain the ν_μ CC QE component we use the ratio of ν_μ to $(\nu_\mu + \bar{\nu}_\mu)$ and the subtracted background four momentum transfer distribution. The ratio is defined in equation 6.11, but now as a function of Q^2. The ratio as a function of four momentum transfer is shown in the left hand plot of figure 6.3.

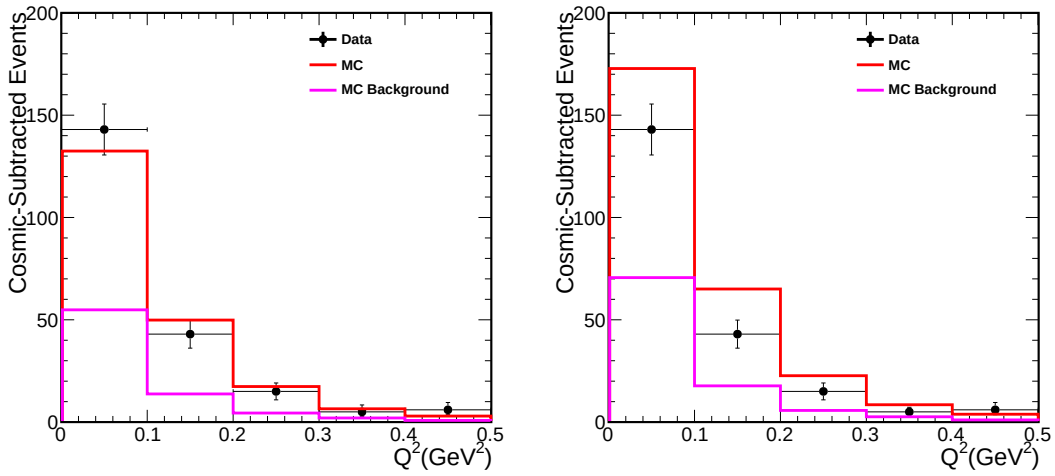

Figure 6.4: Comparison of four momentum transfer square for ν_μ CC QE data events after cosmic ray background subtraction and MC simulation. The red distribution is the MC prediction of signal plus background and the pink curve is the MC background prediction. The black points are the Data. The left hand distribution is area normalized to the Data and the right hand distribution is POT normalized.

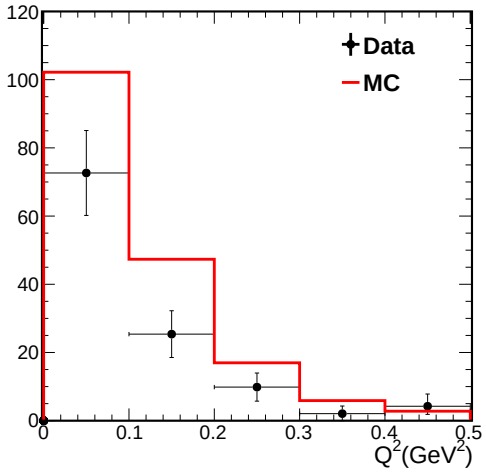

Figure 6.5: Comparison of four momentum transfer for ν_μ CC QE data after cosmic ray background and interaction background subtraction and corrected for anti-neutrino contamination. The MC simulation is POT normalized.

Efficiency as a function of neutrino energy and four momentum transfer

We use the MC simulations to calculate the efficiency of the detector and analysis procedure.

$$\varepsilon = \frac{Selected}{Fiducial}(\quad \nu_\mu CCQE), \tag{6.12}$$

where Selected are the true CC QE events after the CC QE selection and the *Fiducial* are the true CC QE events in the true vertex fiducial volume. The efficiency as a function of true neutrino energy is shown in the left hand plot of figure 6.6. Using the definition for the efficiency from equation 6.12 the efficiency as a function of the true four momentum transfer is shown in the right hand plot of figure 6.6.

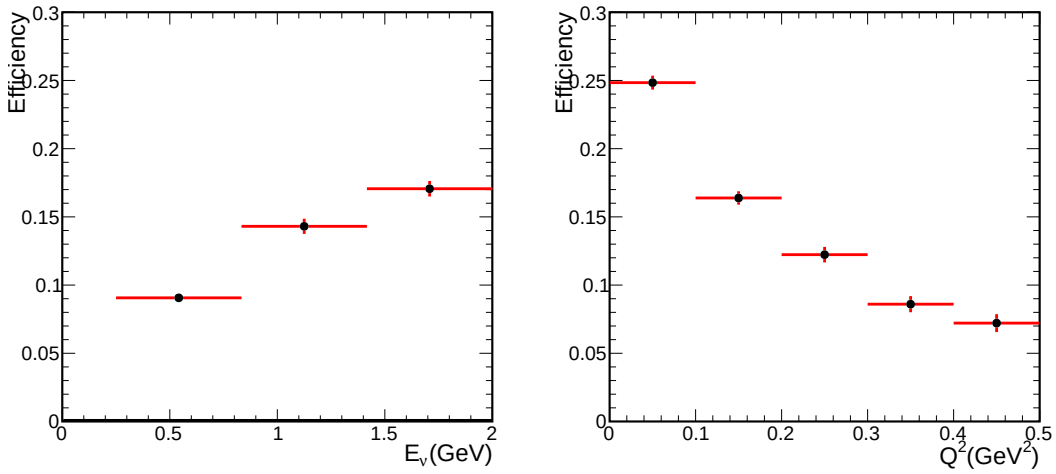

Figure 6.6: Left: Efficiency as a function of true neutrino energy. Right: Efficiency as a function of true four momentum transfer.

6.2.3 Unfolding Procedure

To calculate the CC QE cross section we use a Bayesian unfolding procedure to correct for detector resolution [77]. Starting with the number of events in a set of reconstructed bins $N_{rec,j}$, this procedure gives an estimate for the distributions of true events $N_{true,i}$ in a given bin.

The following review of the unfolding method is taken from [78].

Consider $N_{rec,j}$ events in a reconstructed energy bin j. The number N_{ij} of those events expected in a true energy bin i is

$$N_{i,j} = P(i|j)N_{rec,j} \tag{6.13}$$

where $P(i|j)$ is the conditional probability for an event to be reconstructed in bin j when it is actually in bin i. The total number of events expected to be in true energy bin i is

$$N_{true,i} = \sum_j P(i|j)N_{rec,j}. \tag{6.14}$$

The resolution is unfolded by finding $P(i|j)$. Using the Bayes's theorem for conditional probabilities:

$$P(i|j) = \frac{P(j|i)P(i)}{P(j)} \tag{6.15}$$

where $P(i|j)$ is expressed in terms of the conditional probability and the total prior probabilities i and j. P(j) can be written as the sum over all the probabilities that something in state i is really in state j times the probability that it is in state i in the first place,

$$P(i|j) = \frac{P(j|i)P(i)}{\sum_i P(j|i)P(i)}. \tag{6.16}$$

Inserting this expression into 6.14 we obtain

$$N_{true,i} = \sum_j \frac{P(j|i)P(i)}{\sum_l P(j|l)P(l)} N_{rec,j}. \tag{6.17}$$

Now we have an expression for the unfolding matrix in terms of the prior probabilities $P(i)$ and the conditional probabilities $P(j|i)$. Both can be obtained using the Monte Carlo. The $P(j|i)P(i)$ is the migration matrix $A_{i,j}$. We can write equation 6.17 in terms of the migration matrix as

$$N_{true,i} = \sum_k \frac{A_{i,j}}{\sum_l A_{l,j}} N_{rec,j} \tag{6.18}$$

where $A_{i,j}$ is the probability that a quantity with a true value of i will end up being assigned the value j. To obtain an unfolding matrix, we first bin the MC events in reconstructed and true energy to form the migration matrix A, then calculate the unfolding matrix elements

$$U_{i,j} = \frac{A_{i,j}}{\sum_l A_{l,j}}. \tag{6.19}$$

Here the matrix $A_{i.j}$ is normalized in each bin of reconstructed energy. This procedure is different from the matrix inversion method in which the unfolding matrix is normalized in each bin of true neutrino energy and inverted after the normalization. It is used here because the matrix inversion method is unstable, producing large variations in the unfolded distribution due to small fluctuations in the reconstructed distribution. [79].

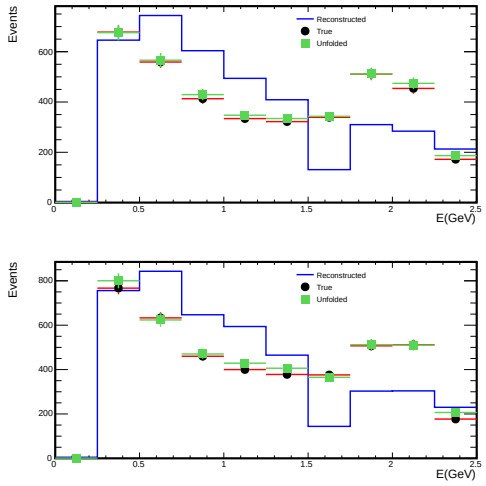

Figure 6.7: Reconstructed Neutrino Energy. The red points correspond to the true neutrino energy, the green is the unfolded neutrino energy and the blue is the reconstructed neutrino energy. The top distributions are made using the same MC simulation used to build the unfolding matrix as a check of the method. The bottom distributions are made using an independent MC sample to test the unfolding.

Figure 6.7 shows a comparison of the true, reconstructed and unfolded neutrino energy spectrum using the MC simulation for configuration 2. The top plots show the unfolding applied to the same MC simulations used to build the unfolding matrix as a procedural check for both energy and momentum transfer distributions. The bottom plots show the unfolding applied to events generated by an independent MC sample, the MC statistic used for training and testing are similar. In addition, we studied a sample of MC with similar statistics as the Data, details can be found in [80]. The 6.8 plots shows the four momentum transfer using the same sample used for the neutrino energy spectrum. In both cases, the unfolding corrects the reconstructed spectrum to better match the true spectrum.

Now, using the Data we perform the unfolding for configuration 2 and the result is shown in figure 6.9. First, we subtract the irreducible background from RES, DIS and NC interactions and correct for the anti neutrino contamination as explained in the previous section. Then apply the unfolding. The black points are the reconstructed Data for neutrino QE events and the blue curve is the unfolded Data as a function of neutrino energy.

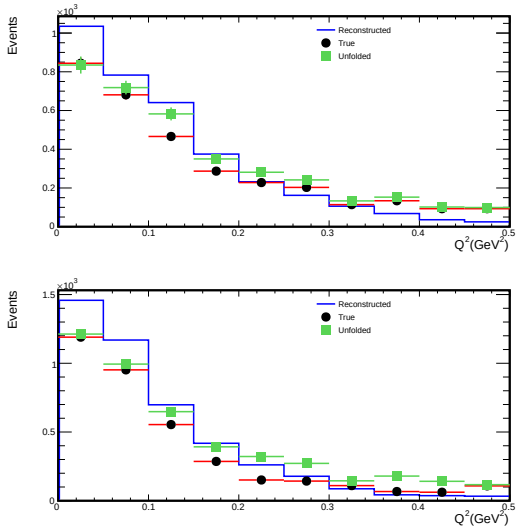

Figure 6.8: Event rate as function of four momentum. The red points give the true four momentum transfer, the green is the unfolded four momentum transfer and the blue is the reconstructed four momentum transfer. The top distributions are made with the same MC events used to build the unfolding matrix. And bottom distributions are made using an independent MC sample to test the unfolding.

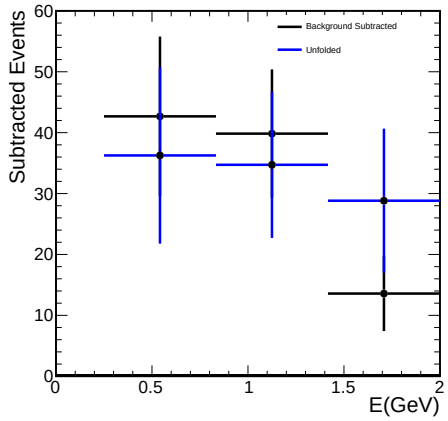

Figure 6.9: Comparison of reconstructed neutrino energy spectrum (black) and unfolded neutrino energy energy spectrum (blue) for configuration 2.

6.2.4 Closure Test

The cross section normalization procedure was checked by comparing the cross-section calculated from simulated MC events to the input GENIE cross-section [95]. We compute the cross-section using

$$\sigma_i = \frac{N_{QE_i}}{\phi_i T} \tag{6.20}$$

where the N_{QE} are the true CC QE events in the true vertex fiducial volume for configuration 2, the number of neutrons ($T = 3.768 \times 10^{30}$) as determined in section 5.1 and the flux ϕ for ν_μ. For the flux we use the gSimple flux[82] which is used as input to the generation events in GENIE. We use the gSimple flux version because it has the best prediction of the neutrino flux. The input distributions for the cross section calculation are shown in figure 6.10, the left hand distribution is the total flux as a function of true neutrino energy and the right hand distribution is the event rates as a function of neutrino energy for events in true vertex fiducial volume. Applying equation 6.20, we divide the neutrino energy distribution by the flux for each bin and normalize it to the number of neutron targets.

Figure 6.11 shows the true cross section in black and the extracted cross section in red

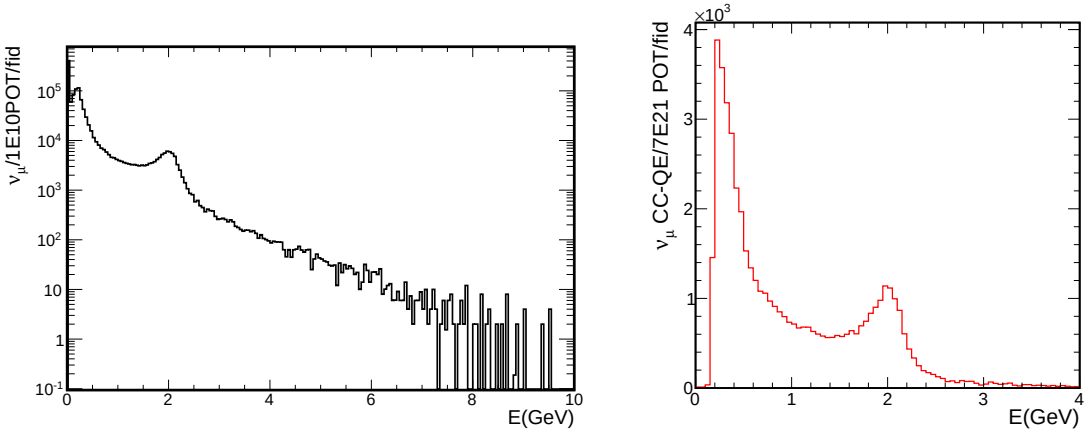

Figure 6.10: Left: Neutrino flux corresponds to $1E10POT$ and events in the true fiducial volume. Right: Neutrino energy distribution for $7E21POT$ and for events interacting in the true fiducial volume.

for the true Monte Carlo. These distributions show good agreement in both normalization and shape.

Furthermore, we compute the cross section using a MC sample and compare with the true cross section, following all the analysis steps used for Data (section 6.2). Figure 6.12 shows the comparison of the true cross section with the calculated cross section, black is the true GENIE cross section, red is the calculated cross section from simulated events using the true information from GENIE and the pink is the extracted cross section using the analysis

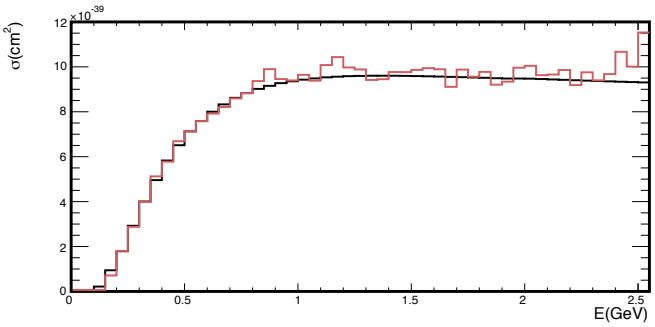

Figure 6.11: Cross-section comparison. Black is the input GENIE cross-section used in the simulation and red is the calculated cross section from the simulated events.

chain. The closure test shows good agreement between the Unfolded MC cross section and the input GENIE cross section within the statistical uncertainties.

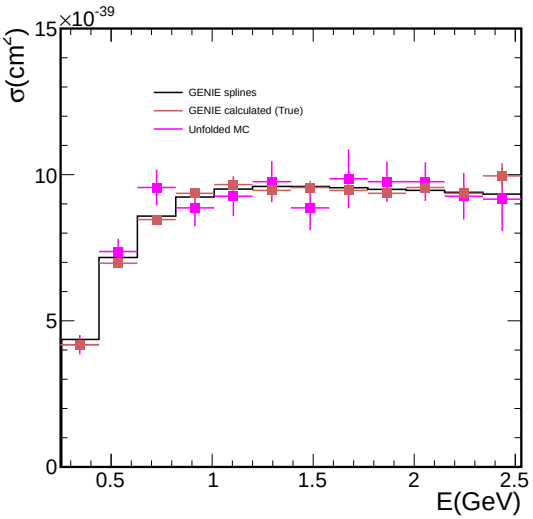

Figure 6.12: Cross-section comparison. Black is the input GENIE cross-section used in the simulation, red is the calculated cross section from the simulated events using the true neutrino energy and pink is the calculated cross section using all steps of the analysis, background subtraction, unfolding and efficiency correction.

6.3 Cross Section Systematic Uncertainty Summary

The cross section uncertainty includes those from both statistics and systematics. This section summarises all the systematics considered for the cross-section calculation. The details about each systematic uncertainty are described in section 7. The systematics considered are:

1. Muon momentum uncertainty. Our prediction of neutrino energy comes from the range of the tracks, converted to momentum. We estimate the muon momentum uncertainty using the track length uncertainty and propagate this error to the neutrino energy prediction. Section 7.1 gives a detailed explanation.

2. Uncertainty in the NuMI beam flux. The uncertainty in the flux is due to the uncertainty of the horn focusing properties together with the uncertainties of hadron production. Section 7.2 explains in detail the procedure used to predict these errors.

3. Neutrino interaction modeling. We use GENIE reweighing tools to vary different parameters in the MC simulation to determine their effect on the cross section. We also studied the intranuke parameters for each background component[95]. Section 7.3 presents the details of this study.

4. Channel configuration modeling. This uncertainty comes from any difference between the actual masked channels for a Data run and the bad channel map used in the MC. Details are given in section 7.3.

5. Energy calibration uncertainty. This uncertainty is obtained by shifting the calibration of the ADC by 10% in the MC simulation and comparing with the nominal MC. Details can be found in section 7.5.

6. Alignment uncertainty. This uncertainty takes into account the uncertainties introduced by positioning errors within the detector and the uncertainty of the angle in the neutrino energy estimate. Section 7.6.

7. Detector mass uncertainty and proton on target uncertainty. Section 7.7.

8. Unfolding uncertainty. Section 7.8.

Assuming that these uncertainties are uncorrelated, we add each systematic uncertainty in quadrature bin by bin. Figure 6.13 shows the contributions to the total systematic uncertainty as a function of neutrino energy and four momentum transfer. The systematic uncertainty is dominated by the flux uncertainty.

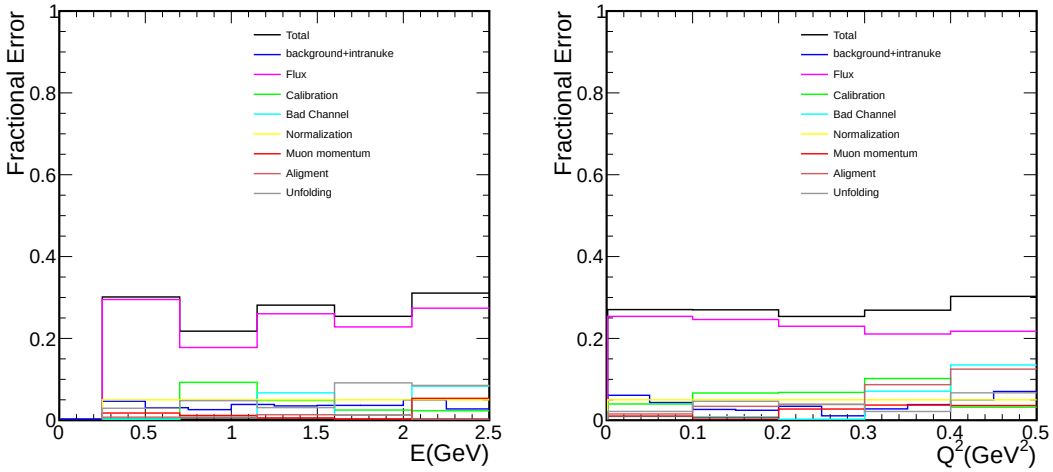

Figure 6.13: Fractional error as a function of neutrino energy and fractional error as a function of four momentum transfer.

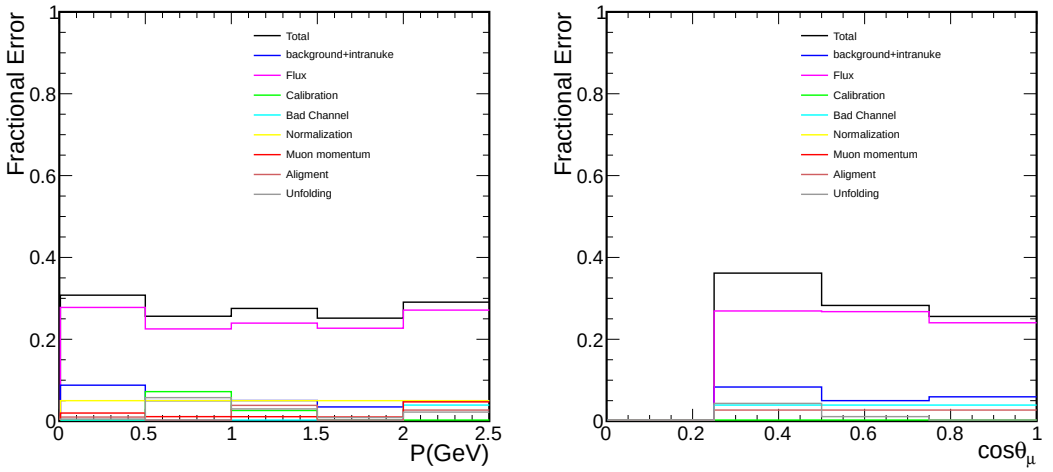

Figure 6.14: Fractional error as a function of momentum and $\cos\theta$.

6.4 Results

6.4.1 Cross section as a function of energy

The cross section as a function of energy is obtained using $\sigma = \frac{\sum_j U_{ij} N_{QE}}{\epsilon \phi T}$ as described in Section 6.2.

Two different normalizations are shown. In the left hand plot, the MC is area normalized to the Data showing good agreement in the behavior of the Data and MC model. In the right hand plot the MC and Data are normalized by POT, showing a possible disagreement between the Data and the model in absolute normalization. Doing a χ^2 test for the left hand area normalized distributions, we obtain $\chi^2 = 0.939, NDF = 2$ and a χ^2 test for the POT normalized distributions, we obtain $\chi^2 = 5.707, NDF = 3$.

Table 6.4 shows the measured cross-section together with the statistical, systematic and the total uncertainties in each energy bin.

Comparison of the measured cross section with the GENIE cross section used in the sim-

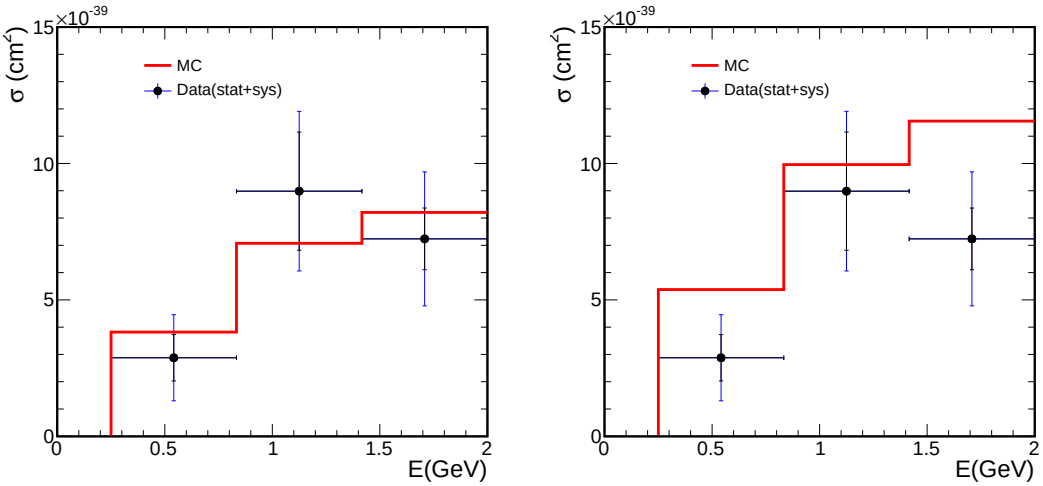

Figure 6.15: Cross-section as a function of energy for configuration 2. The left distribution shows the MC normalized to Data and the right distribution is POT normalized.

ulation is shown in figure 6.16, where the GENIE cross section is extracted directly from GENIE [84]. GENIE uses a dipole form factor approximation with an axial-vector mass equal to $M_A = 0.99 GeV/c^2$.

In addition, we plot the variation of the Quasi-Elastic cross section based on the axial mass M_A. We use GENIE reweighing tools to obtain the $+1\sigma$ and -1σ range for the CC QE interactions, in the MC simulation[95]. This is shown in figure 6.17, where the blue bands represent the axial mass M_A range. This comparison is made to see if the Data is within the M_A uncertainty of the cross section model used in the simulation. The comparison shows

good agreement for Data and MC simulation within the M_A uncertainties.

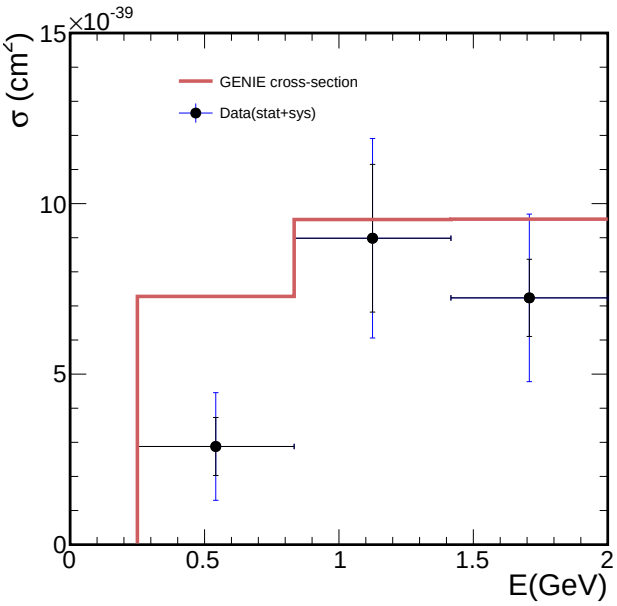

Figure 6.16: Comparison of the measured cross-section and the GENIE cross-section used in the simulation (in red). Black points are Data and the black errors bars are from statistical errors. The blue error bars include systematic errors.

E(GeV)	$\sigma(cm^2)$	$stat(cm^2)$	$sys(cm^2)$	$total \quad error(cm^2)$
0.25-0.8	2.9×10^{-39}	0.9×10^{-39}	1.9×10^{-39}	1.6×10^{-39}
0.8-1.4	8.9×10^{-39}	2.2×10^{-39}	2.9×10^{-39}	2.9×10^{-39}
1.4-2.0	7.2×10^{-39}	1.1×10^{-39}	3.0×10^{-39}	2.5×10^{-39}

Table 6.4: Cross section measurement as a function of E.

6.4.2 Flux Integrated Single Differential Cross Section

The single differential cross sections $\frac{d\sigma}{dP}$, $\frac{d\sigma}{d\cos\theta}$ and $\frac{d\sigma}{dQ^2}$ are computed using the same procedure as for the cross section as a function of energy but binned in muon momentum P, angle of the muon with respect to the beam direction $\cos\theta$ and Q^2.

Figures 6.18 and 6.19 show the single differential cross section as a function of angle and momentum. The left hand plot shows the MC normalized to Data and the right hand plot is the POT normalized distribution. The area normalized distributions show good shape agreement and the POT normalized distributions show a possible disagreement between the Data and MC simulation in absolute normalization. And tables 6.5 and 6.6 gives the measured cross section with systematic and statistical errors for each bin.

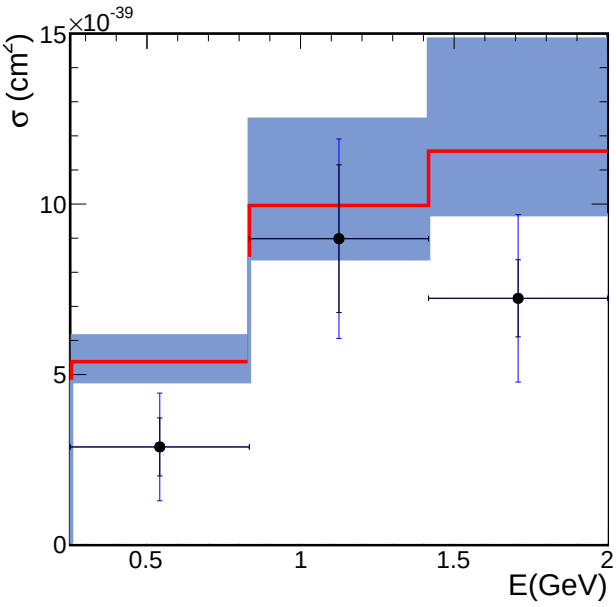

Figure 6.17: Comparison of the measured cross-section and the extracted MC cross-section, both MC and Data has gone through the analysis chain. Black points are Data. The black errors are statistical uncertainties and the blue includes systematic uncertainties. The blue band represent the $+1\sigma$ and -1σ uncertainty from the axial mass M_A.

$P(GeV)$	$\frac{d\sigma}{P_{QE}}(cm^2/GeV)$	$stat(cm^2/GeV)$	$sys(cm^2/GeV)$	$tot \quad error(cm^2/GeV)$
0-0.5	2.4×10^{-39}	0.6×10^{-40}	0.8×10^{-40}	1×10^{-39}
0.5-1.0	0.9×10^{-39}	0.3×10^{-40}	0.2×10^{-40}	0.4×10^{-39}
1.0-1.5	0.6×10^{-39}	0.2×10^{-40}	0.2×10^{-40}	0.2×10^{-39}
1.5-2.0	0.4×10^{-39}	0.1×10^{-40}	0.1×10^{-40}	0.1×10^{-39}
2.0-2.5	0.1×10^{-39}	0.05×10^{-40}	0.03×10^{-40}	0.06×10^{-39}

Table 6.5: Flux integrated single differential cross section as a function of muon momentum P.

$\cos\theta$	$\frac{d\sigma}{\cos\theta}$	$stat$	sys	$tot \quad error$
0.25-0.5	1.0×10^{-39}	3.4×10^{-39}	0.4×10^{-39}	2.6×10^{-39}
0.5-0.75	2.7×10^{-39}	1.1×10^{-39}	0.8×10^{-39}	1.4×10^{-39}
0.75-1	4.8×10^{-39}	0.8×10^{-39}	1.2×10^{-39}	1.4×10^{-39}

Table 6.6: Flux integrated single differential cross section as a function of $\cos\theta$, the angle between the muon and beam direction.

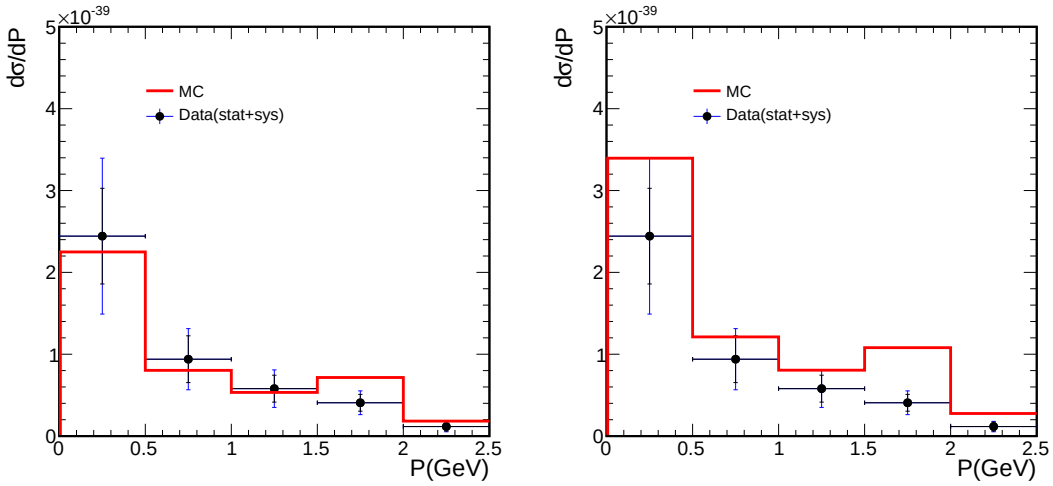

Figure 6.18: Comparison of the measured flux integrated single differential cross section as a function of the muon momentum (P) and the MC simulation. Black points are Data and the black errors are from statistical errors. The blue error bars are from statistical and systematic added in quadrature. Left: MC normalized to Data. Right: distribution is POT normalized.

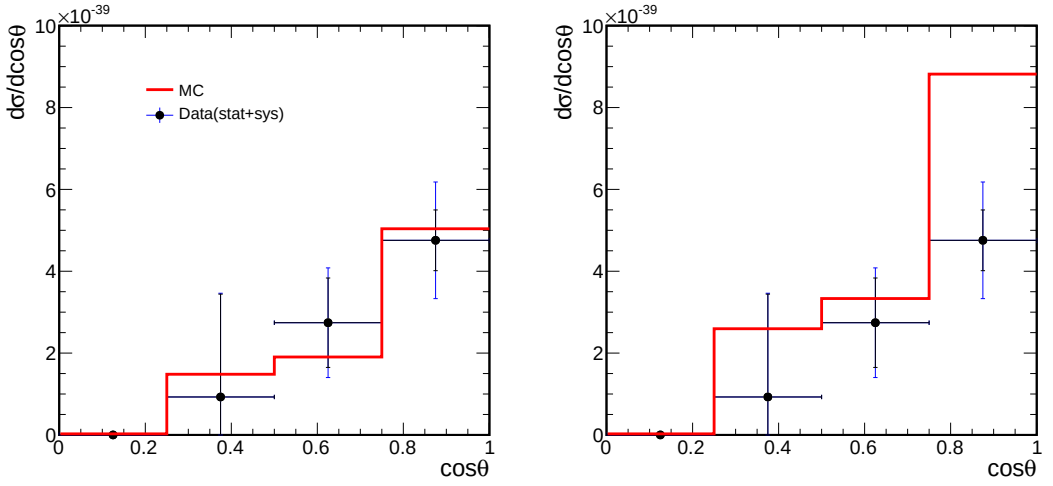

Figure 6.19: Comparison of the measured flux integrated single differential cross section as a function of $\cos\theta$ and the MC simulation. Black points are Data and the black errors is from statistic errors and blue from statistic and systematic added in quadrature bin by bin. Left: MC normalized to Data and right distribution is POT normalized.

The single differential cross section as a function of Q^2 is shown in figure 6.20. The left hand plot shows the MC normalized to Data and the right hand plot is the POT normalized distribution. The area normalized distributions on the left show good agreement between the behavior of the Data and the MC model. Doing a χ^2 test for the left hand area normalized distributions, we obtain $\chi^2 = 1.66, NDF = 4$ and a χ^2 test for the POT normalized distributions, we obtain $\chi^2 = 18.51, NDF = 5$.

We observe a disagreement between the Data and the MC simulation for low Q^2 values ($Q^2 < 0.2GeV^2$). This is shown in the right hand distributions of figure 6.20. Similar disagreements between Data and MC simulation in the Q^2 distribution have been found from MINOS experiment[42] and MiniBooNE experiment[40], where MINOS used NEUGEN and MiniBooNE used NUANCE event generators in their MC simulation.

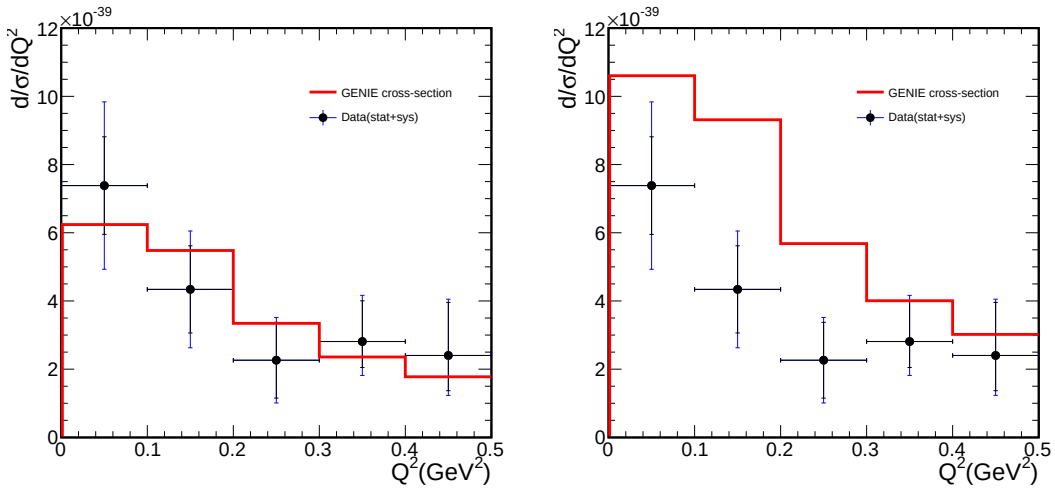

Figure 6.20: Comparison of the measured flux integrated single differential cross section as a function of Q^2 and the MC simulation. Black points are Data and the black errors bars are from statistical errors while blue are from statistic and systematic added in quadrature bin by bin. Left: MC normalized to Data. Right: POT normalized.

$Q^2(GeV^2)$	$\frac{d\sigma}{dQ^2_{QE}}(cm^2/GeV^2)$	$stat(cm^2/GeV^2)$	$sys(cm^2/GeV^2)$	$tot \quad error(cm^2/GeV^2)$
0-0.1	7.2×10^{-39}	1.4×10^{-39}	1.9×10^{-39}	2.4×10^{-39}
0.1-0.2	4.2×10^{-39}	1.2×10^{-39}	1.0×10^{-39}	1.7×10^{-39}
0.2-0.3	2.2×10^{-39}	1.1×10^{-39}	0.5×10^{-39}	1.2×10^{-39}
0.3-0.4	2.7×10^{-39}	1.2×10^{-39}	0.5×10^{-39}	1.2×10^{-39}
0.4-0.5	2.3×10^{-39}	1.5×10^{-39}	0.5×10^{-39}	1.6×10^{-39}

Table 6.7: Flux integrated single differential cross section as a function of Q^2

Chapter 7

Systematic Uncertainties

The systematic uncertainties come from the physics modeling of the neutrino interactions, detector response to the interactions and flux uncertainty. This section describes the determination of each systematic uncertainty.

7.1 Muon Momentum Uncertainty

The muon momentum is calculated from the track length. We fit the muon momentum to a linear function of its track length in the MC simulation. The figure 7.1 shows the muon momentum versus track length and the result from the fit. In addition, the bottom distribution shows the resolution of the momentum, where resolution is defined as $\frac{P_{true}-P_{reco}}{P_{true}}$.

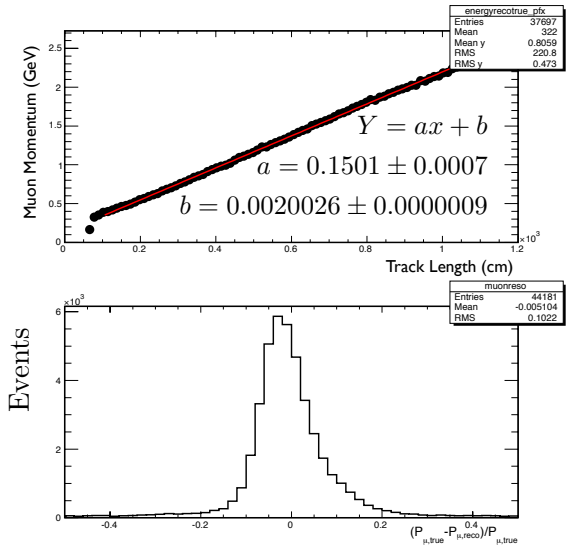

Figure 7.1: Muon momentum as a function of track length from the MC simulation for configuration 2.

The muon momentum uncertainty is calculated using the uncertainty on the length of the track as follow:

$$\frac{\Delta P}{P} = \frac{\Delta L}{L}, \tag{7.1}$$

where ΔL is the uncertainty on the length of the muon track. The uncertainties considered are from dead material uncertainties as follows: the detector cell wall thickness, the glue thickness and from the material in the muon catcher. The uncertainty for the wall thickness is taken from the extrusion manufactures tolerance ± 0.025 cm[85]. The glue thickness is extracted from the MC simulation and we assign a 50% uncertainty (0.033 ± 0.0165) cm. In the muon catcher, the uncertainty per plane is 2%[86] on each 10 cm steel plane.

Using these uncertainties, the fractional error is calculated to be $\frac{\Delta L}{L} = 0.006$, where L is the length of the cell.

We use this fractional error in calculating the neutrino energy and four momentum transfer using equations (5.8) and (5.9) to find the muon momentum uncertainty. This procedure is applied for the neutrino energy and four momentum transfer. Figures 7.2 and 7.3 show the nominal MC, a systematic 1 sigma shift MC, and the ratio of the neutrino energy and four momentum transfer. The ratios show small muon momentum uncertainty. This contributes less than 4% of the fractional error.

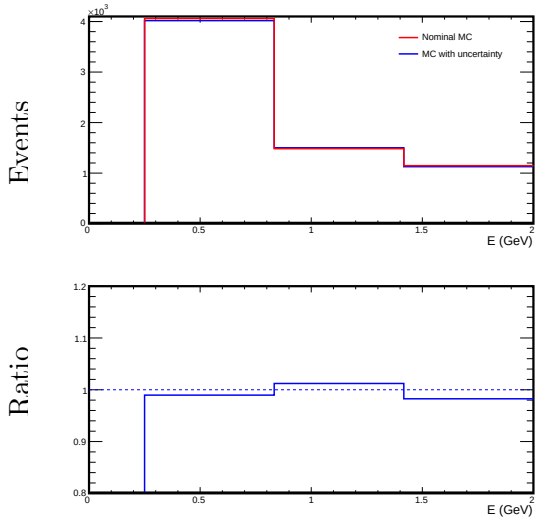

Figure 7.2: Neutrino energy distribution, red is the nominal MC and the blue is the MC with the muon momentum uncertainty applied. Bottom shows the ratio of the distributions.

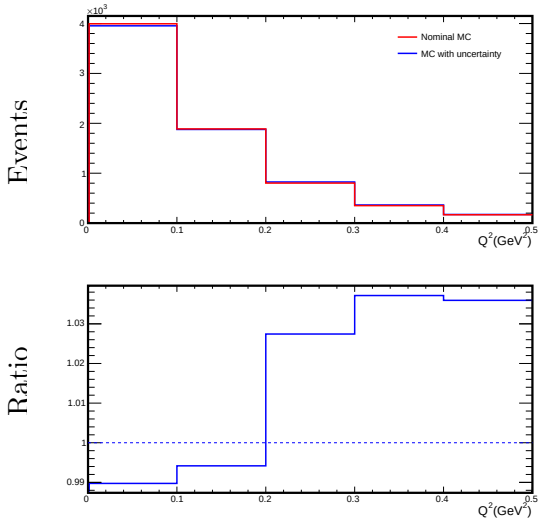

Figure 7.3: Four momentum transfer, red is the nominal MC and the blue distribution is the MC after muon momentum uncertainty is applied. Bottom shows the ratio of the distributions.

7.2 Systematic Uncertainties in the NuMI Beam Flux

Two sources of flux uncertainties were studied. The first is the uncertainty in the flux due to the focusing properties of the horns and the second is from the hadron production model.

7.2.1 Uncertainty due to horn focusing properties

The systematic uncertainty from the horn focusing properties has been studied using the same techniques as the MINOS experiment[88].

The neutrino spectrum at the detector depends on the alignment of the beam line elements. For example changing the horn position has the effect of increasing the focusing for high energy pions. Figure 7.4 shows the horns and some examples of trajectories for pions through the horns. Figure 7.5 shows the nominal alignment of the target and the focusing horn. This figure shows fast pions exiting the target at small angles. These pions can pass through the field free aperture of the horn, while slower pions exit the target at larger angles and enter the horn field region between the two conductors. Therefore, a misalignment of the horns can produce the distortion of the neutrino energy spectrum.

Flux uncertainties due to several beam focusing misalignments are considered. These systematic uncertainties were studied carefully by the MINOS experiment and the Mini-BooNE experiment[88], [89]. We use the same uncertainties used by the MINOS experiment

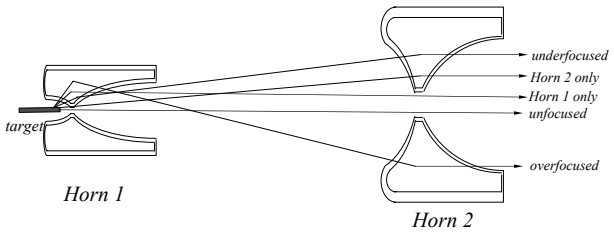

Figure 7.4: Schematic diagram of horns in the LE10 beam, the figure shows 5 categories of pion trajectories through the horns. This figure is from [88].

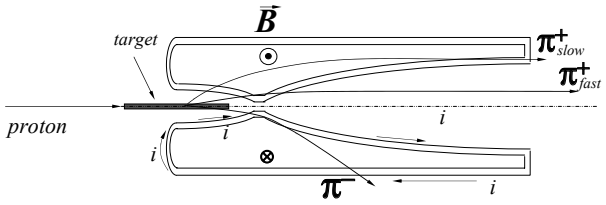

Figure 7.5: Diagram of a low-momentum pion entering horn 1 at large angle and a high-mementum pion entering the horn at small angle. Figure taken from [89].

and consider the following focusing uncertainties:

1. Transverse misalignment of horn 1 and horn 2 by 1 mm.
2. Angular misalignments of horn 1 and horn 2 by 1 mradian.
3. Uncertainty in the chase wall locations by 0.5 inches.
4. Uncertainty (taken to be 1%) in the absolute value of the horn current.
5. Uncertainty in the distribution of the horns current in their inner conductor,[88].
6. Scraping of 1% of the proton beam on the collimating baffle.
7. Target offset.

The focusing effects were simulated in PBEAM [87] and compared to the nominal beam line condition. For each uncertainty, five different configurations were simulated, nominal plus four different misalignments[88]. The nominal configuration is simulated using gnumi-v18. Ratios of the flux with misaligned elements to the nominal flux are taken. Figure 7.6 shows the true neutrino energy spectrum on the left hand plot and the ratios for each of offsets on the right hand plot for the selected quasi-elastic events. For the horn1, four offset were considered 1mm (red histogram), 2mm (blue histogram), 3mm (pink histogram), 4mm (green histogram) and the nominal (black histogram).

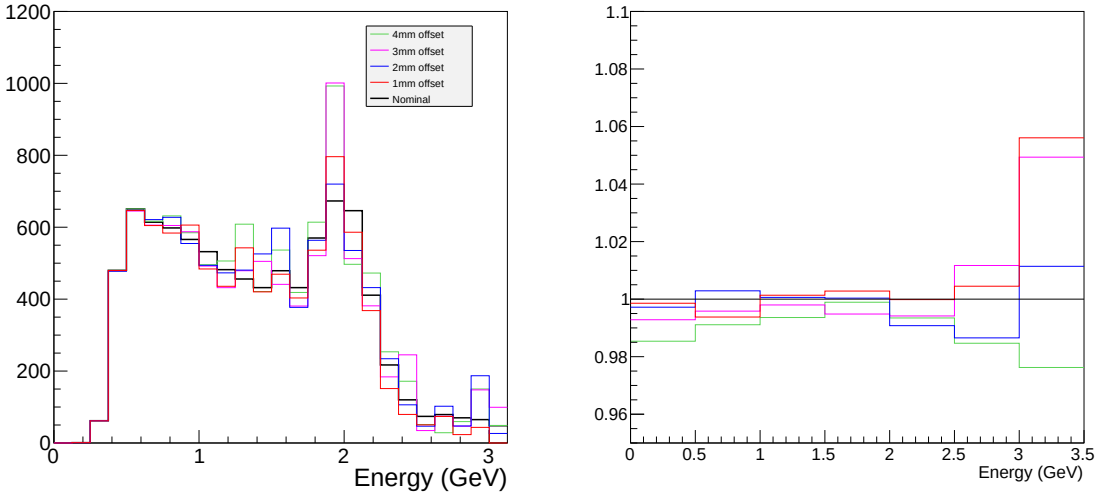

Figure 7.6: Left: True neutrino energy spectrum for the different misalignments positions (1mm, 2mm,3mm,4mm) for the horn 1. Right: Ratio of offset flux to nominal flux.

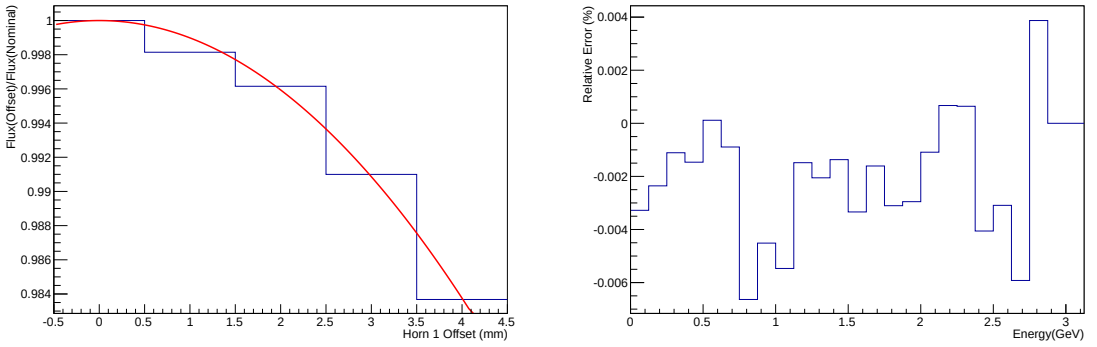

Figure 7.7: Left: Ratio of flux offset to nominal flux as a function of the horn offset for the 2 GeV bin. Right: Relative error for the horn 1 offset.

To determine the error from this misalignment an extrapolation method was used. Using the four offset ratios in figure 7.6, we fitted a second order polynomial to the measured neutrino spectrum distortion as a function of the magnitude of the misalignment for each bin. This is shown in figure 7.7 for one bin in neutrino energy (2 GeV). We repeat this polynomial fit extrapolation for each bin in neutrino energy. Once the fitted polynomial was found for all neutrino energy bins an error was calculated by evaluating the polynomial for a 1.0mm offset. The 1.0mm alignment uncertainty is taken from previous studies [88].

For angular misalignments, four flux histograms were generated using PBEAM for the configurations rotated by 1mrad, 2mrad, 3mrad and 4mrad from the nominal horn 1. The effect of each misalignment is shown as a function of true neutrino energy in the left hand plot of figure 7.8. The right plot shows the ratio of the misaligned flux to nominal flux.

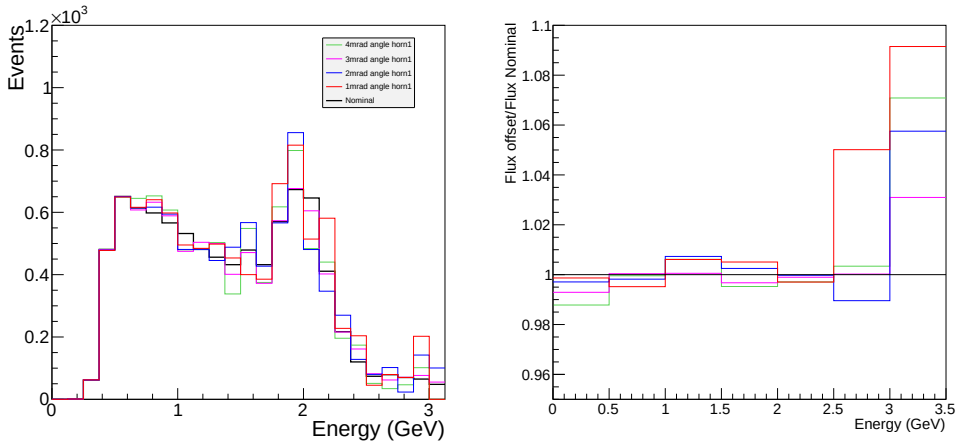

Figure 7.8: Left: True Neutrino energy spectrum for different misalignments in the angle for horn 1. Right: Ratio to the nominal flux.

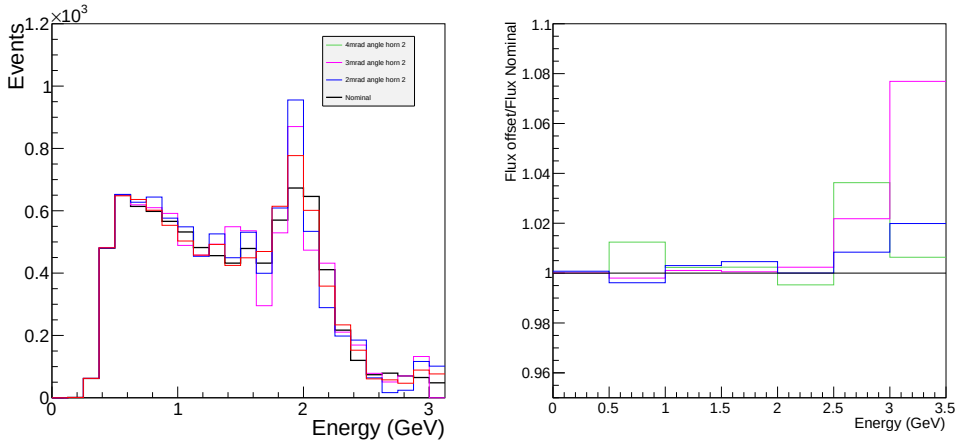

Figure 7.9: Left: True Neutrino energy spectrum for different misalignments in the angle for horn 2. Right: Ratio to the nominal flux.

Figure 7.9 shows the effect of the angular misalignment for the horn 2. This procedure is repeated for the different misalignments, the chase wall locations, the absolute value of the horn current, the distributions of the horns current, and the scraping of the proton beam. The ratios in figures 7.6 and 7.8 show small differences and differences around 3 GeV are from low statistics. The ratio of the offset flux to the nominal flux is found by combining all of these effects and is shown in the left hand plot of figure 7.10.

Using the ratios from figure 7.10 we find the fractional uncertainty for each bin of neutrino energy. The total fractional uncertainty is shown on figure 7.11.

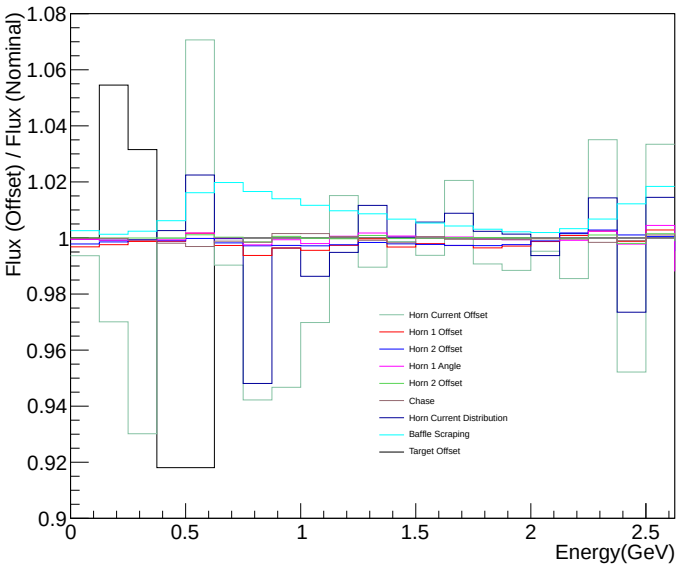

Figure 7.10: Ratios of flux offset to nominal flux for each of the focusing effects, transverse misalignments of horn 1 and 2, angular misalignment of horn 1 and horn 2, the uncertainty in the chase wall locations, the uncertainty in the absolute value of the horn current, the uncertainty in the distribution of the horns current; and the scraping of 1% of the proton beam on the collimating baffle.

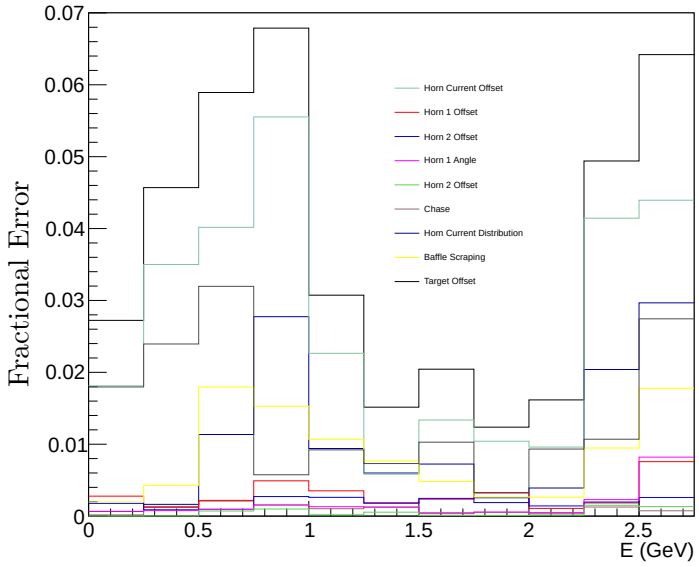

Figure 7.11: Fractional uncertainty of the muon neutrino flux at the Near Detector Prototype for the NuMI LE beam due to focusing effects. The colors represent each of the focusing effects, the horn current offset, horn 1 offset, horn 2 offset, horn 1 angle offset, horn 2 angle offset, chase, horn current distribution, baffle scraping, target offset.

7.2.2 Systematic Uncertainty from hadron production

We estimate the systematic uncertainty from hadron production by comparing the FLUGG and NuMIGeant4 simulations[90][62]. We use the disagreement of the these two simulations to estimate the error from the hadron production. The FLUGG simulation uses Fluka plus Geant4 geometry and NuMIGeant4 uses pure Geant4. Figure 7.12 shows the neutrino energy distributions for both simulations and the ratio between these distributions.
Adding the beam alignment uncertainty and the uncertainty from the hadron production

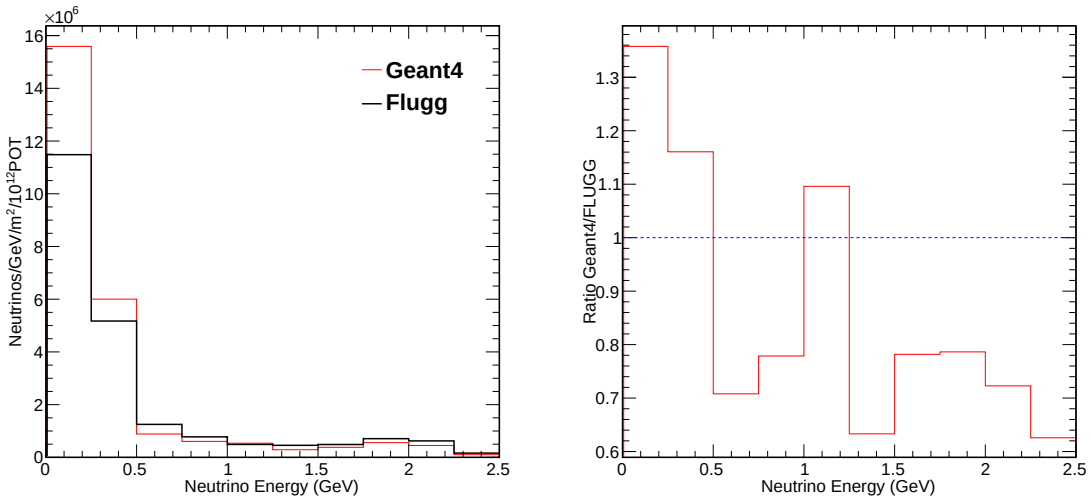

Figure 7.12: Left: True energy spectrum from two flux simulations FLUGG and GEANT4. Right: Ratio of the two simulations.

in quadrature bin by bin gives the fractional error as function of energy and as a function of Q^2 as is shown in figure 7.13. The green distribution is the uncertainty from the horn focusing effects and the pink distribution from the hadron production uncertainty. The black distribution is the total uncertainty. These distributions show the uncertainty is dominated by the flux model.

7.2.3 Systematic Uncertainty from the π^+/π^- ratio in hadron production

The systematic uncertainty from $\bar{\nu}_\mu$ contamination is predicted using the π^+/π^- ratio for Data and MC simulations. We compare data from the CERN NA49 experiment [109] with our FLUGG simulations and use the difference as the systematic uncertainty. Figure 7.14 shows the comparison of the NA49 data (158 GeV proton beam) and our FLUGG simulation, which uses a 120 GeV proton beam. At higher p_T the FLUGG simulation shows a disagreement with the data. However our experiment has essentially no acceptance for pions with a p_T above 0.3 GeV/c and p_z above 15 GeV as shown in figure 7.16. This

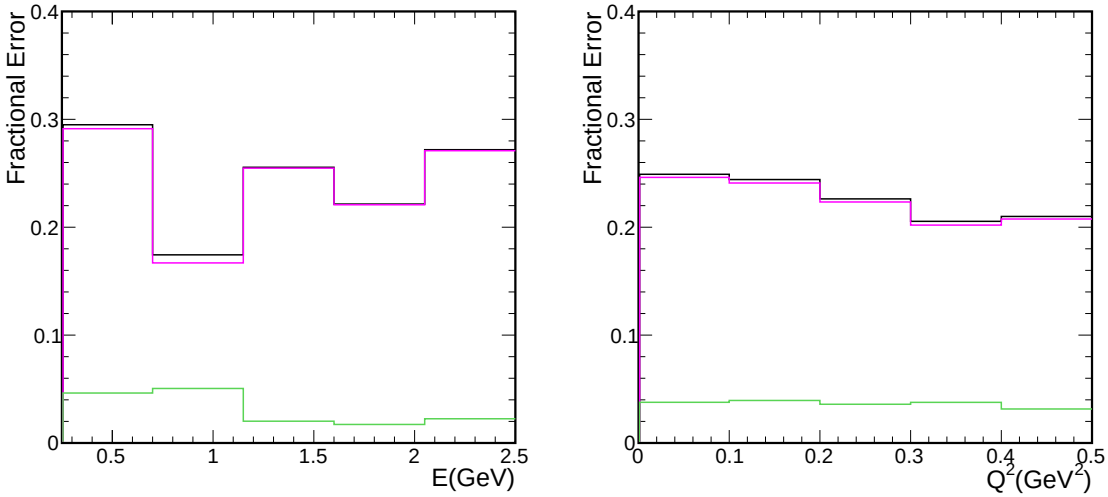

Figure 7.13: Left: Fractional error as a function of reconstructed neutrino energy. Right: Fractional error as a function of reconstructed Q^2. The green distribution is from focusing effects and the pink distribution from the hadron production model.

plot shows that most of our events come from low p_z and low p_T.

Furthermore, figure 7.15 shows the comparison of the NA49 data with the FLUKA simulations from the MINOS experiment [92]. At low p_Z NA49 data and MC simulations (GFLUKA, FLUKA01, FLUKA05) are in good agreement. Note that the MARS simulation does not agree with the others. The ratio π^+/π^- Data-MC comparison in figure [**?**] has less than 10% of difference at low p_z, excluding the MARS simulation. We use 10% as an estimation of the systematic uncertainty.

Figure 7.17 shows the ratio of $\nu_\mu/(\nu_\mu+\bar{\nu}_\mu)$ as a function of neutrino energy for our simulation with and error bands from the range of the NA49 data. To determine the error bands, we applied an additional weight to each neutrino event depending on its parent hadron [93]. This systematic uncertainty is used in the cross section systematic uncertainty (section 8).

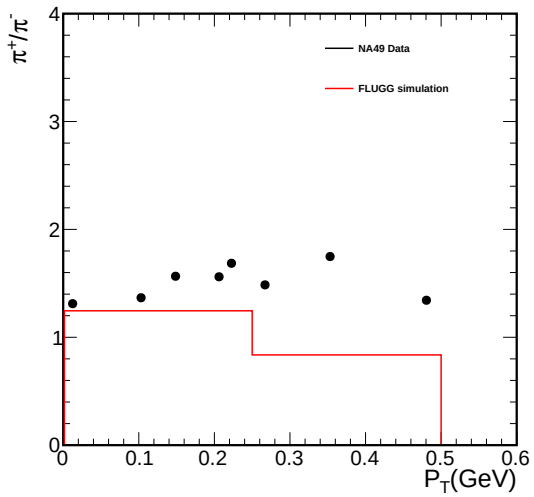

Figure 7.14: Ratio of π^+/π^- as a function of p_T for the NA49 data and our FLUGG MC simulations. The plot is taken from [109].

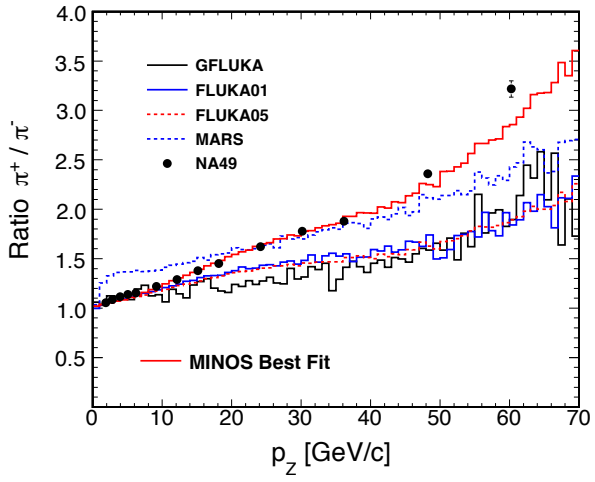

Figure 7.15: Ratio of π^+/π^- as a function of p_z for the NA49 data and MC simulations, plot taken from [75]. For our simulation we use FLUKA.

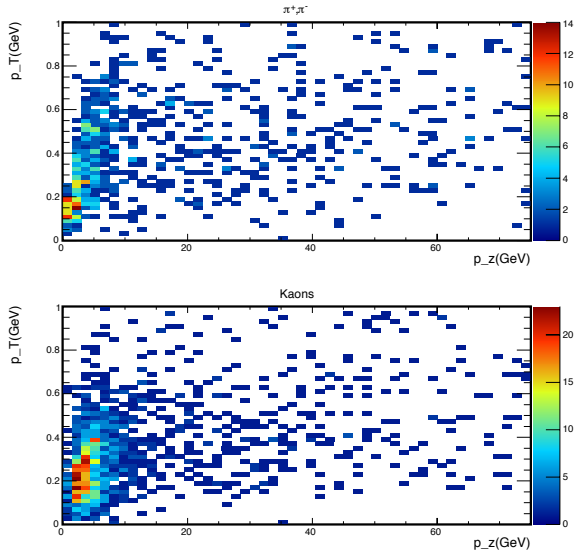

Figure 7.16: p_T versus p_z for the ν_μ of our CC QE events for simulated truth MC.

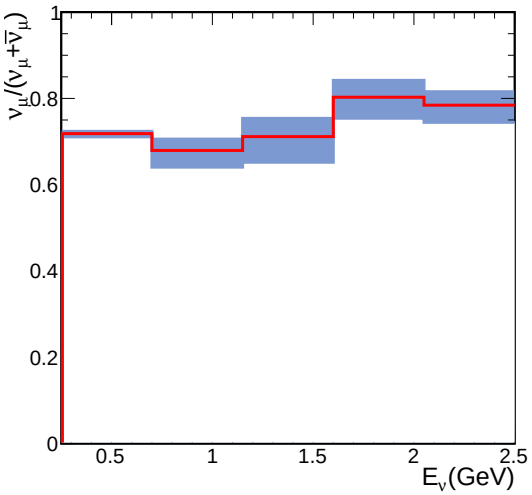

Figure 7.17: Ratio $\nu_\mu/(\nu_\mu + \bar{\nu}_\mu)$ as a function of neutrino energy. Error bands give the systematic uncertainty prediction from the π^+/π^- ratio in hadron production.

7.3 Background Uncertainties

The CC QE selection for the Near Detector Prototype contains some irreducible background from other charged current interactions (RES, DIS and COH) and from neutral current interactions. To determine the uncertainty from the background in the quasi elastic selection, we use the GENIE reweighting tools [94] to find one sigma variation in each of the parameters for the corresponding background.

Two source of systematics are investigated in this analysis. The first is from uncertainties in the neutrino cross section and the second from uncertainties in the intranuclear hadron transport. GENIE uses Intranuke for modeling final state interations (FSI) effects and its reweighing tool provides a list of physics parameters that can be adjusted in the model [95].

The table 7.1 shows the different parameters changed in the MC to study the background uncertainties.

The plot in figure 7.18 shows the fractional errors for each of the backgrounds as a function of the four momentum transfer for a 1σ variation of the parameters in table 7.1. The plot of figure 7.19 shows the uncertainties coming from the Intranuke parameters.

Although the fractional errors from figure 7.19 are not necessarily independent, they have been added in quadrature bin by bin. The total result is shown in figure 7.20.

Uncertainty	Description	1σ
Ma Elastic scattering	Adjust M_A in elastic scattering cross section	$\pm 25\%$
CC Resonance Production	Adjust M_A in Rein-Sehgal CC cross section affecting shape and normalization	$\pm 20\%$
NC Resonance Production	Adjust M_A in Rein-Sehgal NC cross section affecting shape and normalization	$\pm 20\%$
Coherent model M_A	Adjust M_A in the Rein-Sehgal Coherent model	$\pm 40\%$
Non resonant interactions	Affects NC and CC production of single pion final states	$\pm 50\%$

Table 7.1: Cross section model uncertainties. Table taken from H. Gallagher [103]

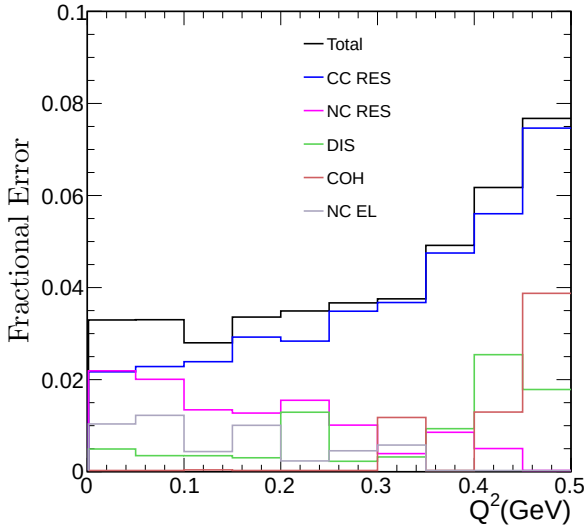

Figure 7.18: Fractional uncertainty for each of the background components as a function of Q^2, for each of the background (CC RES, CC DIS, CC COH, NC RES and NC EL). The black curve represents the total uncertainty due to the background. This total uncertainty is calculated adding the component uncertainty in quadrature bin by bin.

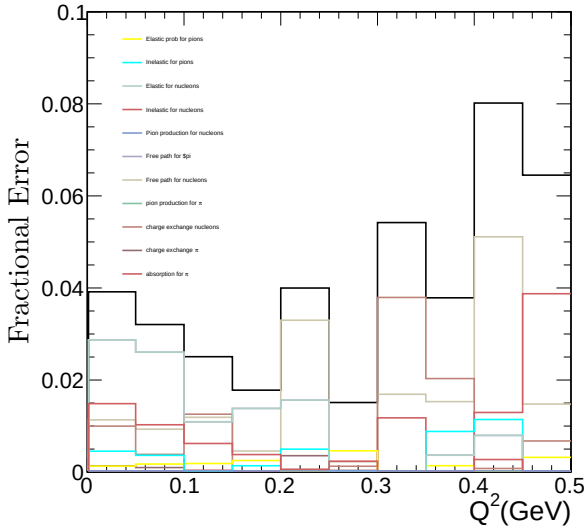

Figure 7.19: Fractional uncertainty from Intranuke as a function of Q^2, the following parameters has been studied: elastic probability for pions, inelastic for pions, elastic for nucleons, inelastic for nucleons, pion production for nucleons, free path for π, free path for nucleons, pion production, charge exchange nucleons, charge exchange π and absorption for π.

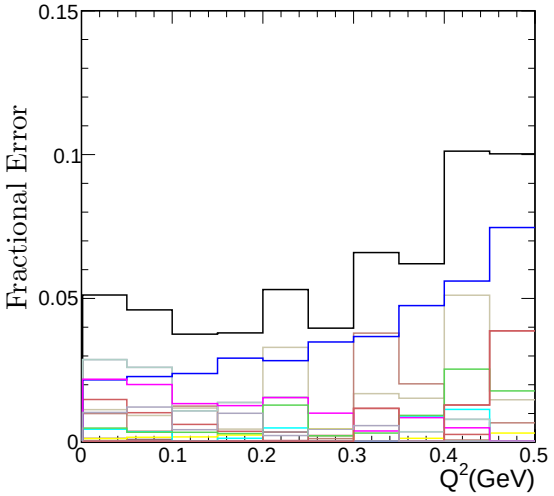

Figure 7.20: Total background and cross section uncertainties from figures 7.18 and 7.19. This total uncertainty is calculated adding the errors in quadrature bin by bin.

Uncertainty	Description	1σ
Pion mean free path	mean free path for poins	±20%
Nucleon mean free path	mean free path for nucleons	±20%
Pion fates pion production	charge exchange probability for poins	±20%
Pion fates absorption	absorption probability for pions	±30%
Nucleon fates charge exchange	charge exchange probability for nucleons	±50%
Nucleon fates Elastic	elastic probability for nucleons	±30%
Nucleon fates charge Inelastic	inelastic probability for nucleons	±40%
Nucleon fates absorption	absorption probability for nucleons	±20%
Nucleon fates pion production	pion production probability for nucleons	±20%
Pion fates Elastic	elastic probability for pions	±10%
Pion fates charge exchange	charge exchange probability	±50%
Pion fates Inelastic	inelastic probability for pions	±40%

Table 7.2: Cross section model uncertainties. Table taken from H. Gallagher [103]

7.4 Bad Channels Uncertainty

The bad channel uncertainty comes from malfunctioning detector channels that are not removed from the analysis using the regular analysis package (standard bad channels removed). To determine the bad channel uncertainty, we use two samples of MC, one with the standard bad channels removed [59] and another MC sample with standard bad channels plus any extra bad channels remaining which were found using the efficiency for reconstructing cosmic muon tracks. We removed the any additional bad channels found from the analysis and ran the reconstruction for the same MC sample. The comparison of the regular MC and the additional bad channel removed MC gives us the uncertainty.
An example of the bad channels detected using the cosmic rays by the occupancy plot is shown in figure 7.21. Occupancy is defined as $Log(\#Hits/Event)$. The black distribution is the occupancy for all the channels used in the analysis and the red distribution shows the bad channels detected by the cosmic ray efficiency. Details about the determination of bad channels from both methods can be found in [97][99].

The comparison between the nominal MC and the cosmic ray bad channel removed MC is shown in figure 7.22. The top plot shows the neutrino energy distributions and the bottom the ratio. The second set of plots on the bottom shows the four momentum transfer distributions and their ratio. The bad channel uncertainty is small less than 1% where there is a significant amount of data.

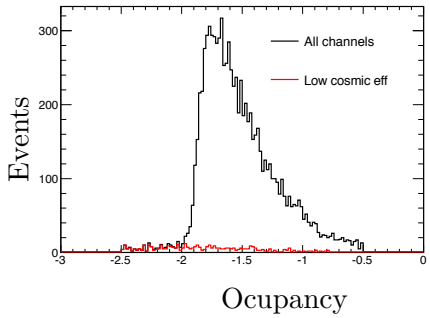

Figure 7.21: Occupancy distribution. The black distribution correspond to all the channels and the red the low cosmic efficiency for cosmic ray data. Plot taken from [99]

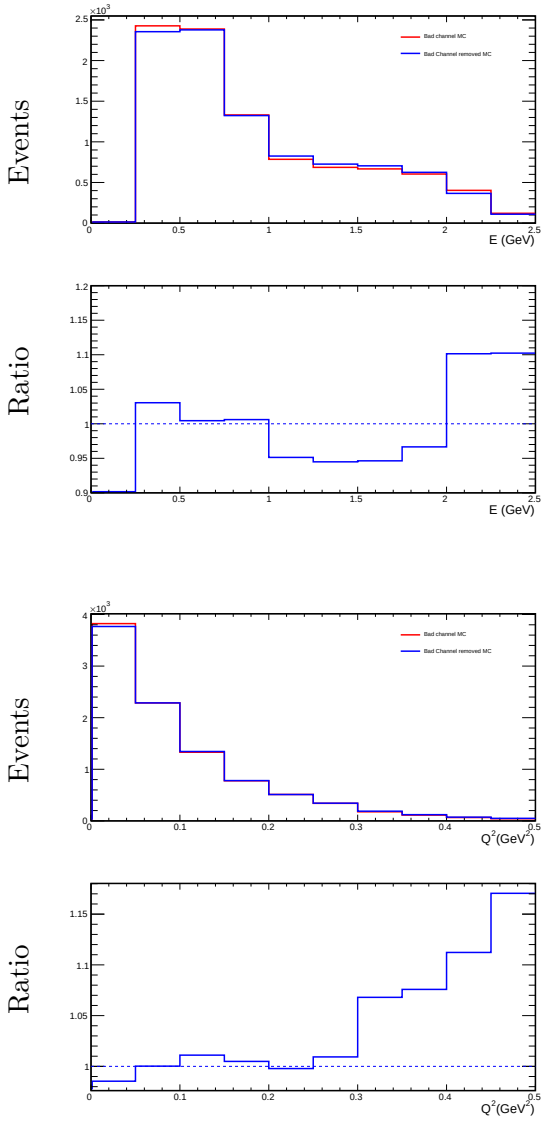

Figure 7.22: Neutrino energy for MC and four momentum transfer for the MC. The red distribution is the MC with the nominal bad channel maps and the blue is the MC altered by removing the extra bad channels. Bottom distributions shows the ratio of nominal MC to altered MC.

7.5 Calibration Uncertainty

The calibration uncertainty come from the two input variables used in the KNN in the CC QE selection. Those variables are directly related with the pulse height, the energy around the vertex (PECorr) and the mean energy per active plane to track length(chapter 5).

The calibration uncertainty was studied by changing the pulse height to photoelectron conversion by 10%. We use conservative estimate of the calibration uncertainty (10%)[98]. Two samples of MC were produced for this study, one with the nominal calibration constant and a second set of MC was produced by shifting the calibration of the ADC by 10%. Figure 7.23 and 7.24 shows the neutrino energy and four momentum transfer distributions for the nominal MC and for the altered MC with 10% change in the PE. The bottom plots are the ratios. These ratios show the calibration uncertainty is small within 5%.

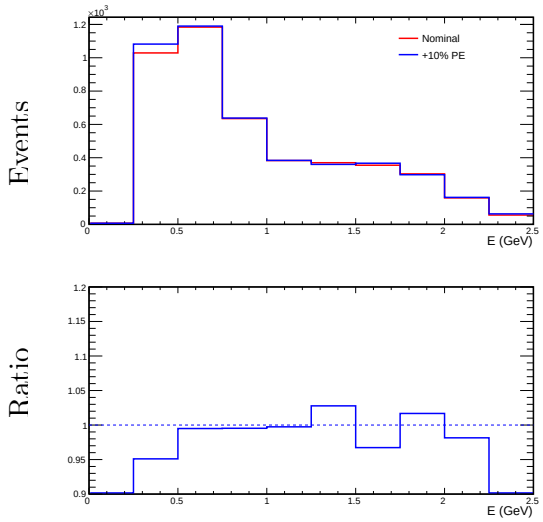

Figure 7.23: Neutrino energy and four momentum transfer distributions. The blue distribution is made by shifting the calibration of the ADC by 10% in MC and the red is the nominal MC. The bottom plot shows the ratio of these two distribution

7.6 Alignment Uncertainty

The alignment uncertainty was studied by applying random shifts to each of detector cells. We used 1 cm random shift between the nominal Monte Carlo and a shifted Monte Carlo. We did constrain the cells to be contiguous while doing the shifts. Details about the Alignment procedure can be found at [101]. Figure 7.25 and 7.26 shows the neutrino energy and four momentum transfer distributions for the nominal Monte Carlo in red and the shifted Monte

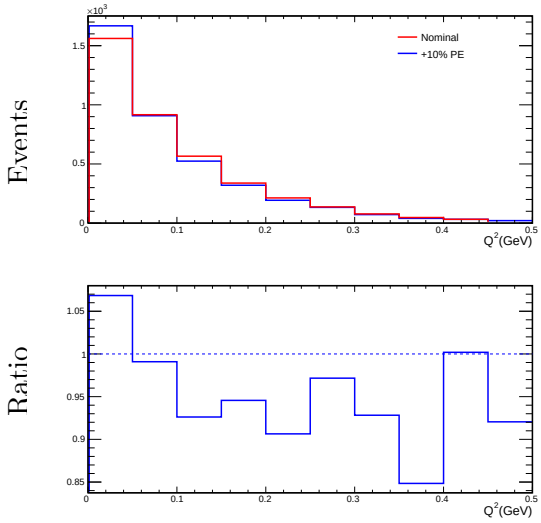

Figure 7.24: Neutrino energy and four momentum transfer distributions. The blue distribution is made by shifting the calibration of the ADC by 10% in MC and the red is the nominal MC. The bottom plot shows the ratio of these two distribution

Carlo after the misalignment as well as the ratios of those distributions. These ratios show the alignment uncertainty is less than 2%.

7.7 Mass Uncertainty

The mass used in the MC was compared with the mass calculated data table (6.2) and they differ by less than 5%. We use this difference as a systematic uncertainty for the mass calculation and also corrected the cross section normalization in the closure test (section 6.2.4) and in the final calculation (section 6.4.1).

The total mass from data: PVC mass is 38.3 tons, scintillator mass is 91.3 tons[76] and using the function from the Geometry (GeometryBase::TotalMass), we found the PVC mass used in the MC to be 39.9 tons and for the scintillator mass to be 90.9 tons. This produces a difference on the order less than 5%, which is taken as uncertainty in the mass.

Now for the POT uncertainty, we use the same POT counting as the MINOS experiment, the uncertainty is 2% [102]. We take 5% for total normalization uncertainty.

7.8 Unfolding Uncertainty

This systematic uncertainty is determined using several unfolding matrices based on different cross section models. We change the axial mass M_A $(+1\sigma, -1\sigma, +2\sigma, -2\sigma)$ and make the

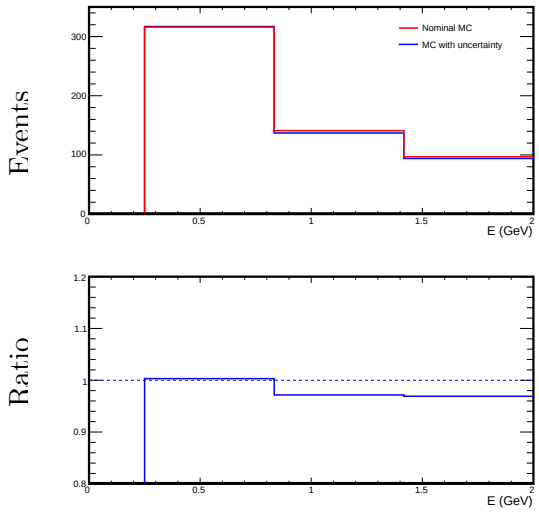

Figure 7.25: Neutrino energy distributions for nominal and one centimeter random shift to each plane. The red distribution is the nominal Monte Carlo and the blue is the shifted Monte Carlo. The bottom distributions are the ratio of nominal to shift distribution.

ratio of unfolded neutrino energy to the true energy for each model to estimate the extent to which the uncertainty from unfolding depends on the neutrino spectrum. In addition, we use the difference between the initial (1) and the final (4) iterations of the unfolding algorithm. A similar procedure was used in recent cross section measurements from the MiniBooNE experiment [100]. Figure 7.27 shows the fractional uncertainty as a function of energy and Q^2. The uncertainty is below 10%.

The differences between the true and the unfolded distribution gives the closure test (section 6.2.4). We have some differences for the closure test. We use the differences between true and unfolded as an additional systematic uncertainty.

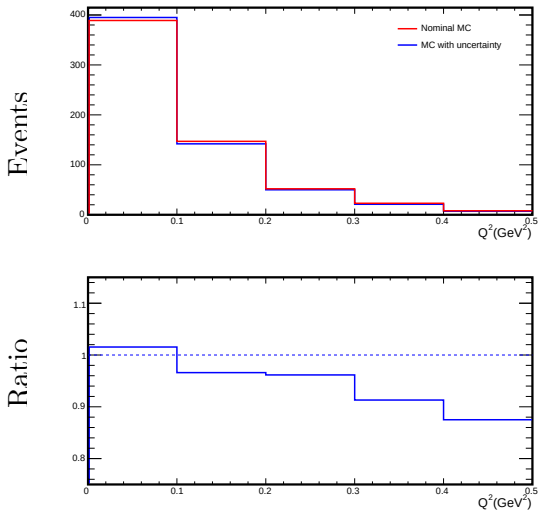

Figure 7.26: Four momentum transfer distributions for nominal and one centimeter random shift to each plane. The red distribution is the nominal Monte Carlo and the blue is the shifted Monte Carlo. The bottom distributions is the ratio of nominal to shifted distribution.

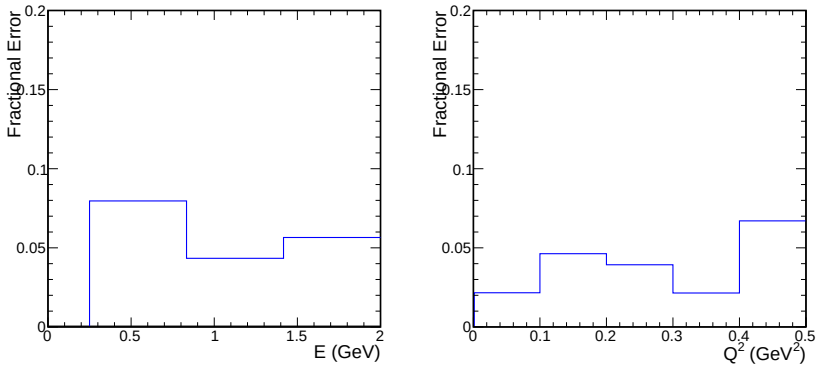

Figure 7.27: Fractional error for the unfolding as a function of neutrino energy and four momentum transfer.

7.9 Propagation of Systematic Uncertainties into the Cross Section

Previous sections described each of the uncertainties for the reconstructed energy and reconstructed four momentum transfer, however the extracted cross section is obtained for the true neutrino energy and true four momentum transfer after the unfolding. Using the systematic uncertainties we build unfolding matrices for each uncertainty, except for the normalization and the background systematic, since unfolding is made after background subtraction. These unfolding matrices are used to unfolded the nominal neutrino energy reconstructed distribution and each of the reconstructed neutrino energy shifted by the uncertainty.

The ratio of the shifted unfolded neutrino energy distribution to the nominal unfolded neutrino energy distribution gives each of the systematic and the final systematic is obtained adding each of the systematic in quadrature bin by bin.

Chapter 8

Summary, Discussion and Future Prospects

We have studied charged current quasi-elastic events induced by neutrinos from the NuMI beam in the NOνA Prototype Detector. Because this was a prototype, the number and position of active channels was constantly changing and two different major configurations of the detector instrumentation were used in this analysis. Section 3.3 described each of the configurations and commissioning. The results presented in this thesis comprise the first study of neutrinos interactions in the NOνA type of detector. Chapter 4 described the simulation, reconstruction and detector calibration. Chapter 5 showed details about the event selection process for muon neutrino quasi-elastic scattering and Chapter 6 described the analysis procedure to measure the cross section.

8.1 Performance of the Prototype Detector

The Prototype Detector was used to test all detector systems: including the structure and operation of the detector, its effectiveness for measuring neutrino and cosmic ray events, the procedures for installation and commissioning, the functioning of the data acquisition system, the fidelity of the simulation program, and the effectiveness of the analysis software. The knowledge learned from the Prototype has been applied to the construction and installation of the NOvA Near and Far detectors currently under construction. For example, some changes that have arisen from the operation of the prototype: (1) new installation procedures, (2) new design of manifold cover parts for the Far Detector, (3) a surface coating for the photodetector was developed to protect their surface, (4) addition of air drying system to guard against the condensation on the photodetector, (5) new mounting for the photodetector. In addition, the Near Detector size has been modified for better containment

of events. Section 3.3.1 and 3.3.2 gave details about the detector performance.

Muon neutrino data from two detector configurations have been studied to understand the response of the detector, the details are presented in chapter 5. We found the Prototype Detector performed well and we were able to analyze the charged current quasi-elastic events from muon neutrino scattering. Each detector configurations perform differently, the momentum resolution ($\frac{P_{true}-P_{reco}}{P_{true}}$) for configuration 1 was 18% and for configuration 2 was 24%.

Both detector configurations had small data sets. The CC QE analysis gave 230 CC QE selected events with 20 cosmic ray background events for detector configuration 2 and 55 events with 11 cosmic ray background for detector configuration 1. From GENIE simulations the CC QE selection in the Prototype Detector contains 47% CC QE ν_μ, 17% CC QE $\bar{\nu}_\mu$, 17% RES, 6% DIS, 9% NC, 2% COH and 2% ν_e interactions.

8.2 The Physics Result

The charged current quasi-elastic (CC QE) cross section is not well understood in the energy range of the NOνA experiment. Section 2.2 presented a review of quasi-elastic cross section measurements.

The measured cross section as function of energy $\sigma(E)$ and the single differential cross sections for $\frac{d\sigma}{d\cos\theta}$, $\frac{d\sigma}{dP}$ and $\frac{d\sigma}{dQ^2}$ are reported in, section 6.4.

The average cross sections for each configuration for the mean energy of the neutrino flux (0.58 GeV) are given in Table 8.1

Configurations	$\sigma(cm^2)$
Configuration 1	$(0.54 \pm 0.18(stat) \pm 0.16(syst)) \times 10^{-38} cm^2$
Configuration 2	$(0.64 \pm 0.14(stat) \pm 0.11(syst)) \times 10^{-38} cm^2$

Table 8.1: Quasi-elastic cross section measurements for both detector configurations at mean energy of 0.58 GeV.

The uncertainty of the energy has been found using the criterium of one sigma deviation from the mean corresponding to 68% of the area of the neutrino energy distribution.

Table 8.1 shows the measured cross section is the same within the uncertainties for both configurations.

Figure 8.1 shows the comparison of the measured cross section for both detector configurations and the data from the MiniBooNE experiment (carbon target), ANL experiment (deuterium target). BNL experiment (deuterium target) and NOMAD experiment (mainly carbon target) [111]. In addition, the GENIE MC prediction from the simulation used in this experiment is shown. The GENIE MC uses the Llewellyn Smith formalism for the quasi-elastic interactions, chapter 2 presented a description of the model.

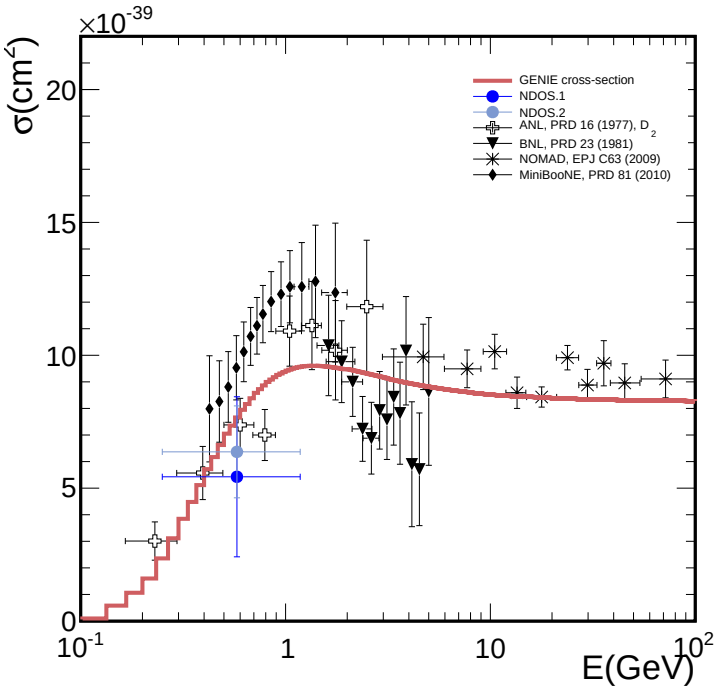

Figure 8.1: ν_μ CC QE cross section measurement as a function of energy for the NOνA Prototype detector for both detector configurations in blue color (configuration 1 and configuration 2) compared with MiniBooNE, ANL, BNL and NOMAD experiments. The red curve shows the MC simulation prediction for GENIE with $M_A = 0.99GeV$

Figure 8.2 shows the comparison of the combined cross section from both detector configurations and the external data. The combine cross section is $(0.60 \pm 0.17(stat) \pm 0.16(syst)) \times 10^{-38} cm^2$. We observe our data agrees with the GENIE simulations within the uncertainties. The GENIE model used for the simulation of this experiment has $\sigma = 0.7 \times 10^{-38} cm^2$ at 0.58 GeV.

The total uncertainty has approximately equal contributions from statistical errors and the systematic uncertainties. The systematic uncertainties are dominated by the uncertainty in the incident neutrino spectrum. Section 7.2 presented details about the determination of this flux uncertainty.

8.3 Future Prospects for the Near Detector

The higher neutrino flux will allow NOνA Near Detector will collect high neutrino event rates to study CC QE interactions, specifically the measurements of cross section and axial mass parameter M_A. The primary differences between the prototype detector and the Near Detector are: the neutrino beam, the detector homogeneity and detector dimensions.

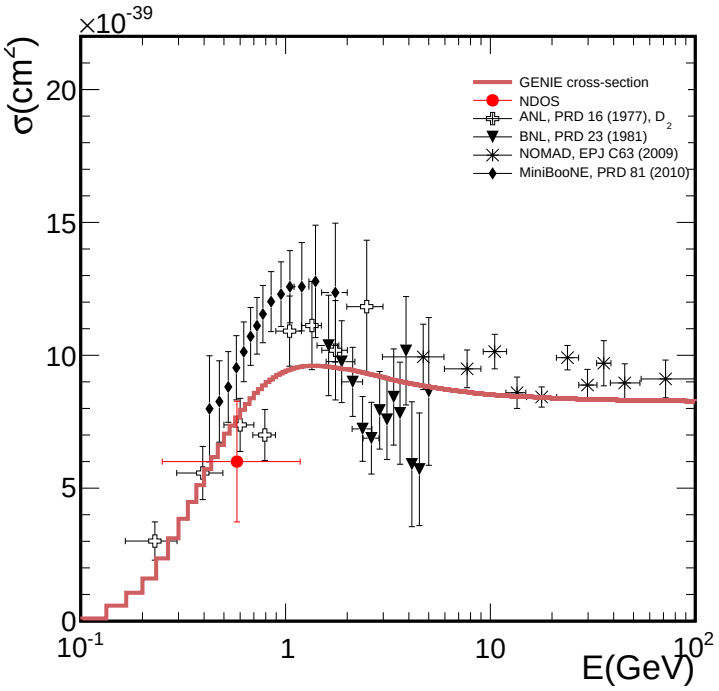

Figure 8.2: ν_μ CC QE cross section measurement as a function of energy for the NOνA Prototype Detector (red point) compared with the MiniBooNE, ANL, BNL and NOMAD experiments. The red curve shows the MC simulation prediction from GENIE with $M_A = 0.99GeV$

The Near Detector energy spectra is different from the Detector Prototype energy spectra, the Prototype Detector is 110 mrad off axis and Near Detector is 14 mrad off-axis. The spectrum of the Near Detector contain a larger contamination of RES, DIS interactions, many of these interactions are irreducible background. For example, we found about 20% of the resonance interactions have a single visible muon in the final state and very small activity around the vertex. Therefore, understanding the background and the modeling will be very important for the study of CC QE events in the NOνA detectors.

Building on this analysis technique, improvements in event selection and systematic uncertainties could be made. The measurement CC QE cross section is difficult to make because of the background coupled with the uncertainties of the background modeling. High statistics allow understanding of the background events. For Example, data driven methods could be used to constraint the background. Since the Near Detector will have higher average energy around 2 GeV, the beam will contain more Neutral Current interactions, that can be studied to refine the separation of pions and muons. This will improve the background rejection. Most importantly, the systematic uncertainty for the CC QE analysis in the Near Detector Prototype is dominated by the flux uncertainty, this systematic error

on the flux needs to be decreased by using external data.

Furthermore, including events with a reconstructed proton track, could increase the knowledge of the CC QE interaction. Because of the low statistics the CC QE analysis in the Detector Prototype had very few events with a second track, we found 5% of the CC QE events had a second reconstructed track. The neutrino beam in the Near Detector contains more CC QE events with a second proton track. An improvement will be to include events with a second visible track, to study CC QE events with a proton track in the final state. This will allow to measure the entire sample of QE scattering and improve the accuracy of the measurement.

References

[1] V. Lyubushkin, *et al.*, [NOMAD collaboration], Eur. Phys. J. **C 63**, 355 (2009). A. A. Aguilar-Arevalo, *et al.*, Phys. Rev. D **81**, 092005 (2010).

[2] F. Reines and C. L. Cowan, Detection of the free neutrino, Phys. Rev. **92**, (1953).

[3] G. Danby et al., Observation of high-energy neutrino reactions and the existence of two kinds of neutrinos, Phys. Rev. Lett. **9**,(1962).

[4] F.J. Hasert et al, Observation of neutrino-like interactions without muon or electron in the Gargamelle neutrino ex- periment, Phys. Lett. B **46** 138 (1973).

[5] K. Kodama et al., Observation of tau-neutrino, Phys. Lett. B **504**, (2001).

[6] Kwon, H., F. Boehm, A. A. Hahn, H. E. Henrikson, J. L.Vuilleumier, J. F. Cavaignac, D. H. Koang, B. Vignon, F. v. Feilitzsch, and R.L. Mo?ssbauer, Phys. Rev. D **24**, 1097, (1981). Hoummada, A., S. L. Mikou, M. Avenier, G. Bagieu, J. F. Cavaignac, and D. H. Koang, Appl. Radiat. Isot. 46, 449, (1995). Zacek, G., et al., Phys. Rev. D 34, 2621. Kuvshinnikov, A. A., et al., 1991, JETP Lett. 54, 253, (1986). Vidyakin, G. S., et al., JETP 93, 424, (1987).

[7] Declais, Y., et al., Phys. Lett. B **338**, 383, (1994).

[8] J. A. Formaggio, G. P Zeller, From eV to Eev: Neutrino cross sections across energy scales, Revies of Modern Physics, **84**, (2012).

[9] Willis, S. E., et al., 1980, Phys. Rev. Lett. **44**, 522.

[10] Reines, F., H. S. Gurr, and H. W. Sobel, Phys. Rev. Lett. 37, 315, (1976). Vershinsky, A. G., et al., JETP Lett. 53, 513, (1991). Kozlov, Y., et al., Phys. At. Nucl. 63, 1016, (2000). Riley, S., et al., Phys. Rev. C 59, 1780, (1999).

[11] M. Maki, M. Nakagawa, and S. Sakata, Remarks on the unified model of elementary particles, Prog. Theor. Phys. **28**,870(1962).

[12] Raymond Davis Jr., Don S. Harmer, and Kenneth C. Hoffman (1968). Search for Neutrinos from the Sun. Phys. Rev. Lett. 20: 1205.

[13] Fukuda, Y., et al. Evidence for oscillation of atmospheric neutrinos. Physical Review Letters 81 (8): 15621567.

[14] Y. Fukuda, Study of the atmospheric neutrino flux in the multi-GeV energy range, Phys. B **436** (1998)p.33.

[15] B. Aharmim et al., Measurement of the ν_e and the total B-8 solar neutrino fluxes with the Sudbury Neutrino Observatory phase I data set, Phys. Rev. C75, 045502(2007). B. Aharmin el al., [SNO collaboration], Phys. Rev. C72, 055502(2005).

[16] K. Eguchi et al., First result from KamLAND: Evidence for reactor anti-neutrino disapearance, Phys. Rev. D74, 094009(2006).

[17] B. Aharmim et al., Measurement of the ν_e and the total B-8 solar neutrino fluxes with the Sudbury Neutrino Observatory phase I data set, Phys. Rev. C75, 045502(2007). B. Aharmin el al., [SNO collaboration], Phys. Rev. C72, 055502(2005), Eguchi et al., First result from KamLAND: Evidence for reactor anti-neutrino disapearance, Phys. Rev. D74, 094009(2006).

[18] Y. Ashie *et al.* [Super-Kamiokande Collaboration], Phys. Rev. D **71**, 112005 (2005) [hep-ex/0501064], P. Adamson *et al.* [MINOS Collaboration], Phys. Rev. D **77**, 072002 (2008) [arXiv:0711.0769 [hep-ex]].

[19] P. Adamson *et al.* [MINOS Collaboration], arXiv:1301.4581. K. Abe et al. (T2K Collaboration) , PRL 107. 041801(2011).

[20] J. K. Ahn *et al.* [RENO Collaboration], Phys. Rev. Lett. **108**, 191802 (2012) [arXiv:1204.0626 [hep-ex]], F. P. An *et al.* [DAYA-BAY Collaboration], Phys. Rev. Lett. **108**, 171803 (2012) [arXiv:1203.1669 [hep-ex]].

[21] M. Goldhaber, L. Grodzins, and A. W. Sunyar, Helicity of Neutrinos, Physical Review 109, 10151017 (1958) doi:10.1103/PhysRev.109.1015

[22] Tingjun Yang, A Study of Muon Neutrino to Electron Neutrino Oscillations in the MINOS Experiment, Ph.D Thesis (2009).

[23] Makoto Kobayashi and Toshihide Maskawa. CP Violation in the Renormal- izable Theory of Weak Interaction. Prog. Theor. Phys., 49:652657, (1973). Nicola Cabibbo. Unitary Symmetry and Leptonic Decays. Phys. Rev. Lett., 10:531533, (1963).

[24] B. Kayser, arXiv:hep-ph/0211134.

[25] D. Griffiths, Introduction to Elementary Particles, 1987.

[26] Quang Ho-Kim, Elementary Particles and Their Interactions, 1998.

[27] D.B. McFarlane et al. (CCFRR), Z.Phys.C 26,1 (1984). N.J.Baker et al. Phys.Rev.D 25, 617 (1982). Reference to other low energy experiments can be found in S.J. Barish et al., Phys.Rev.D 19, 2521 (1979). S.J. Barish et al., Phys.Rev.D 16, 3103 (1977). Nakamura, K., et al., 2010, J. Phys. G 37, 075021, (2010).

[28] C. H. Llewellyn Smith, Phys. Rept. **3**, 261 (1972).

[29] P. E. Bosted, Phys. Rev. C **51**, 409 (1995), H. Budd, A. Bodek, and J. Arrington, hep-ex/0308005.

[30] Nathan Mayer, Measurement of the QE Axial Mass, Ph.D Thesis (2012).

[31] R.A. Smith and E.J. Moniz. NEUTRINO REACTIONS ON NUCLEAR TARGETS. Nucl. Phys., B43:605, (1972).

[32] K. L. Miller, *et al.*, Phys. Rev. D **26**, 537 (1982).

[33] V. Bernard, L. Elouadrhiri, U.G. Meissner, J. Phys. G 28, R1 (2002). arXiv:hep-ph/0107088

[34] T. Kitagaki, *et al.*, Phys. Rev. D **28**, 436 (1983).

[35] T. Kitagaki, *et al.*, Phys. Rev. D **42**, 1331 (1990).

[36] S. Bonetti, *et al.*, Nuevo Cimiento A 38, 260 (1977).

[37] J. Brunner, *et al.*, Z. Phys. C **45**, 551 (1990).

[38] R. Kustom, *et al.*, Phys. Rev. Lett.**22**, 1014 (1969).

[39] R. Gran, *et al.*, Phys. Rev. D **74**, 052002 (2006).

[40] A. A. Aguilar-Arevalo, *et al.*, Phys. Rev. Lett. **100**, 032301 (2008). A. A. Aguilar-Arevalo, *et al.*, Phys. Rev. D **81**, 092005 (2010).

[41] V. Lyubushkin, *et al.*, [NOMAD collaboration], Eur. Phys. J. **C 63**, 355 (2009).

[42] M. Dorman and MINOS Collaboration, AIP Conf. Proc. 1189, pp. 133-13, (2009).

[43] Laura Fields, CC QE Results from MINERνA, Nuint 2012 proceedings (2012).

[44] M. Martini, M. Ericson and G. Chanfray, Phys. Rev. D **85**, 093012 (2012) [arXiv:1202.4745 [hep-ph]].

[45] Rein, D., Z. Phys. C **35** 43 (1987). Rein, D., and L. M. Sehgal, Ann. Phys. (N.Y.) **133**,79 (1981).

[46] V.V. Lynbushkin, K.S. Kuzmin, and V.A. Naumov, Mod. Phys. Lett. A **19**, 2815 (2004), C. Berger and L.M. Sehgal, Phys. Rev. D **76**, 113004 (2007)., C. Berger and L.M. Sehgal, Phys. Rev. D **77**, 059901 (2008).

[47] Jesus Orduna, Observation of the doubly strange b-Baryon Ω_b^-, Ph.D Thesis (2011).

[48] D. S. Ayres et al. [NOvA Collaboration], The NOvA Technical Design Report, FERMILAB-DESIGN-2007- 01.

[49] Minerba Betancourt, Quasi-elastic Studies in NDOS, NOVA-doc 6597.

[50] Susan M. Kasahara, NOνA Data Acquisition System, Technology and Instrumentation in Particle Physics 2011 proceedings and NOνA doc-db 6455.

[51] Leon M. Mualem, NOVA-doc-6346, NOVA-doc-4775.

[52] Thomas Chase, Documentation of Cracks on the Inside of NOνA Manifold Covers, NOVA-doc 5146.

[53] Nicholas Raddatz, Track Reconstruction in the NOνA Experiment, Proceedings of the DPF-2011 Conference, (2011).

[54] G. S. Davies. Cosmic Rate Plots for Blessing. NOVA-doc 7207-v2.

[55] Timothy Kutnink, Detector response calibration for the NOvA quasi-elastic cross-section measurement, M. Sc. Thesis (2012).

[56] Mark Messier, NOVA-doc-5809, The Cana Commissioning Tools, NOVA-doc 5480.

[57] Mathew Muther, NDOS APD Status and Plans, NOVA-doc 6564. Leon M. Mualem, Electronics, NOVA-doc 4775, 7340.

[58] Timthy Kutnik, Status of the NOvA Near Detector Prototype, NOνA-doc 7932.

[59] Minerba Betancourt, NOVA-doc 6559, A note to summary the application of bad channels on the offline files.

[60] Jan Zirnstein *et al.*, NOVA-doc- 7155, Neutrino Candidates and Run Configurations in NDOS.

[61] Alexander I. Himmel, the NuMI Beam Simulation with Flugg, NOνA-doc 5388.

[62] Laura Loiacono, Private communication. Laura provided a g4lbne version from /cvs/projects/lbne-beamsim/repository/show/g4lbne.

[63] Luis Alvarez-Ruso, Costas Andreopoules *et al.*, The GENIE Neutrino Monte Carlo Generator, November 2011.

[64] Anthony Mann and Minerba Betancourt, Scanning Evaluations for the Selected QE events, NOvA-doc 7854.

[65] Susan Lein, NOνA-doc 6805.

[66] Nicholas Raddatz, NOνA-doc 5855, 6111, 6828, 7232, 8065.

[67] Nicholas Raddatz, NOνA-doc 7232.

[68] Christopher Backhouse, NOνA-doc 8221, Nov 2012.

[69] Christopher Backhouse, NOνA-doc 7410, May 2012.

[70] Susan Lein, NOνA-doc 6515, October 2011.

[71] Susan Lein, NOνA Internal Note, NOνA-doc 6515, October 2011.

[72] arXiv:physics/0703039, Data Analysis, Statistic and Probability. November 3, 2009.

[73] Kanika Sachdev, NOνA Internal Note , NOνA-doc 7752.

[74] Michael Baird, An update on POT accounting and the number of neutrinos per spill in GENIE, NOνA-doc 7915.

[75] Anna Pla-Dalmau, Private communication and Nova Collaboration, NuMI Off-Axis nue Appearance Experiment, Technical Design Report.

[76] Karen Kephart, NOνA Internal Note, NOνA-doc 1136, Near Detector Parameters.

[77] G. DAgostini. A multidimensional unfolding method based on Bayes theorem. In: Nuclear Instruments and Methods in Physics Research Section A: Accelerators, Spectrometers, Detectors and Associated Equipment 362.2-3 (1995), pp. 487 498.

[78] Steven K. Linden, Measurement of the ν_μ charged current π^+ to quasi-elastic cross section ratio on mineral oil in a 0.8 GeV neutrino beam, PhD thesis, Yale University, 2011.

[79] M. Betancourt, NOνA Internal Note, NOνA-doc-7852, 7890, 7927, QE Studies update.

[80] M. Betancourt, NOνA Internal Note, NOνA-doc-7927, QE Studies update.

[81] Robert Hatcher, NOνA Internal note, NOνA-doc-7789-v1.

[82] Robert Hatcher, NOνA Internal note, NOνA-doc-7789, 6636.

[83] arXiv:0812.4543, (2009). A. A. Aguilar-Arevalo, et al., Phys. Rev. Lett. 100, 032301(2008),0706.0926.

[84] Robert Hatcher, Private communication. Using TGraph file extracted from the 3665 version of GENIE splines:$/nova/app/users/rhatcher/xsec_graphs_v3665_HCNOSClTiFe.root$.

[85] John W. Cooper, NOνA Internal Note, NOνA-doc 540, Feb 2010.

[86] Patricia Vahle, Muon catcher steel measurements, NOνA Internal Note, NOνA-doc 5221.

[87] PBEAM documentation: $http://home.fnal.gov/\%7Edharris/pbeamdoc/guide_pbeam.txt$

[88] Sacha E. Kopp, Zarko Pavlovic, NOνA Internal Note, NuMI Neutrino Fluxes at the MiniBooNE Detector, nova-doc 3375.

[89] Sacha E. Kopp, Zarko Pavlovic, Dharmaraj Indurtly, MINOS Internal Note, Systematic Uncertainties in the NuMI Beam Flux, MINOS-doc 1283.

[90] Alexander Himmel, The NuMI Beam simulation with Flugg, MINOS Internal Note, MINOS-doc 6316.

[91] Inclusive production of charged kaons in p+p collisions at 158 GeV/c beam momentum and a new evaluation of the energy dependence of kaon production up to collider energies, arXiv:1004.1889 [hep-ex].

[92] Anna Holin, MINOS Internal Note, MINOS-doc 9603.

[93] Bob Zwaska, Private communication, March 21-2013.

[94] Nathan Mayer, NOνA Internal Note, GENIE Reweighting, nova-db 7732, 7917, 8043.

[95] Luis A., Costas Andreopoulos GENIE Physics And User Manual, 2011.

[96] Melody Ravonel Salzgeber, Measurment of the Inclusive ν_μ Charged Current Cross Section in the Near Detector of the T2K Experiment, Ph.D Thesis (2012).

[97] Minerba Betancourt, NOνA Internal Note, A note to summary the application of bad channels on the offline files, NOvA-doc 7302.

[98] Ryan Patterson, Private communication, (Estimation of calibration uncertainty 6%).

[99] Christopher J Backhouse, NOνA Internal Note, Finding bad channels via cosmic ray efficiency, NOvA-doc 7302.

[100] A. A. Aguilar-Arevalo, et al., Phys. Rev. Lett. 100, 032301(2008),0706.0926.

[101] Gavin S. Davies, NOνA Internal Note, Geometry (mis)Alignment and (Mis) Alignment Infrastructure, NOνA-doc 8362, 8530.

[102] P. Adamson et al., Study of muon neutrino disappearance using the Fermilab Main Injector neutrino beam, Phys. Rev. D **77**, 072002(2008).

[103] Hugh Gallagher, Private communication.

[104] Steven Cavabaugh, MINOS Internal Note, doc-db 4145-v3.

[105] Minerba Betancourt, NOνA Internal Note, Cosmic Background Study, NOνA-doc-db 7027, 7156.

[106] P. Adamson *et al.* [MiniBooNE and Minos Collaboration], Phys. Rev. Lett. **102**, 211801 (2009) [arXiv:0809.2447 [hep-ex]].

[107] Private communication with Zarko Pavlovic, he provided the flux histogram.

[108] A. A. Aguilar-Arevalo *et al.* [MiniBooNE Collaboration], arXiv:1301.7067 [hep-ex].

[109] C. Alt *et al.* [NA49 Collaboration], Eur. Phys. J. C **49** (2007) 897 [hep-ex/0606028].

[110] Nicholas Raddatz, NOνA-doc 7739,8321.

[111] V. Lyubushkin, *et al.*, [NOMAD collaboration], Eur. Phys. J. **C 63**, 355 (2009). A. A. Aguilar-Arevalo, *et al.*, Phys. Rev. D **81**, 092005 (2010). K. L. Miller, *et al.*, Phys. Rev. D **26**, 537 (1982).

[112] T. Kitagaki, *et al.*, Phys. Rev. D **28**, 436 (1983).

Appendix A

Study of Cosmic Background

This section presents a summary of the study of cosmic background for the quasi-elastic analysis. We explored different methods to reject the cosmic background. This section shows study of different cuts and the final cuts chose for the analysis.

The study was made using the data corresponding to October 2012 to April 2013 for the neutrino run (configuration 2). For the study of cosmic background we use cosmic data which is out of time from of the spill window from $0\mu s$ to $217\mu s$ and from $227\mu s$ to $500\mu s$ for the NuMI trigger.

Method to eliminate the cosmic background

Different variables were explored to reject the cosmic background, two variables used in the Nue Cosmic background analysis in MINOS [104] were explored. The variables are the following:

1. The Zenith angle. This angle is defined $\theta_{zenith} = acos(\frac{|y2-y1|}{\sqrt{dx^2+dy^2+dz^2}})$, where $dx = x2 - x1, \quad dy = y2 - y1, \quad and \quad dz = z2 - z1.$

2. The difference of the beginning and end of the track in the vertical view ($|y2 - y1|$).

Figure A.1 shows the separation of the cosmic data and beam MC simulations for the Zenith angle and for the difference in y2 and y1 coordinates, where the beam MC includes CC and NC interactions. To reject the cosmic background, a cut in the Zenith angle was chosen $\theta_{zenith} < 0.7$. The second cut is made ($|y2 - y1|$), ($|y2 - y1|$) $> 300cm$. These cuts are very conservative. No signal is rejected as can be seen in Figure A.1. The efficiency of cosmic background rejection is 32% using the two cuts.

A third variable is the inverse of the slope in y. This variable is defined as $\frac{Z2-Z1}{Y2-Y1}$. Figure

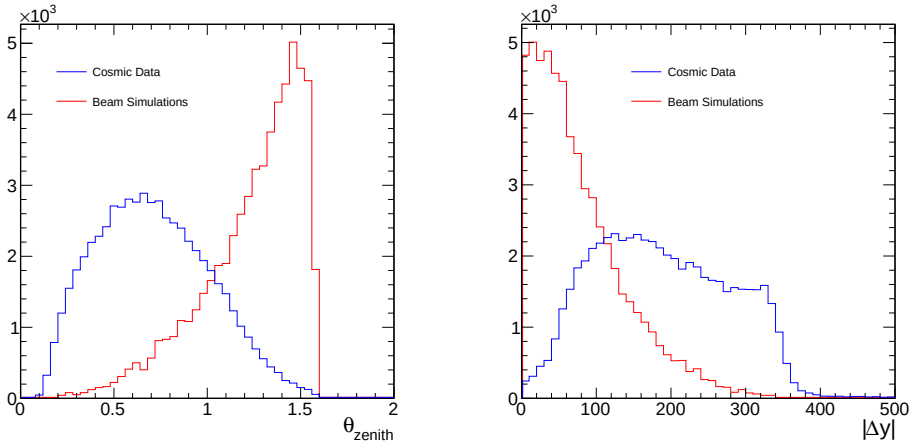

Figure A.1: Zenith angle, the red distribution is the beam MC and the blue is the cosmic background data. Events after fiducial cuts.

A.2 on the right hand left shows the beam MC and the cosmic background separation. The efficiency of cosmic background rejection is 50% using the inverse of the slope variable. The ratio of signal to background using the first two variables is 2.9. Now, using the inverse of the slope variable the ratio of signal to background is 3.8. Using the best ratio of signal to background, the inverse of the slope was selected to reject the cosmic background. The right hand plot on figure A.2 shows the figure of merit FOM for the inverse of the slope

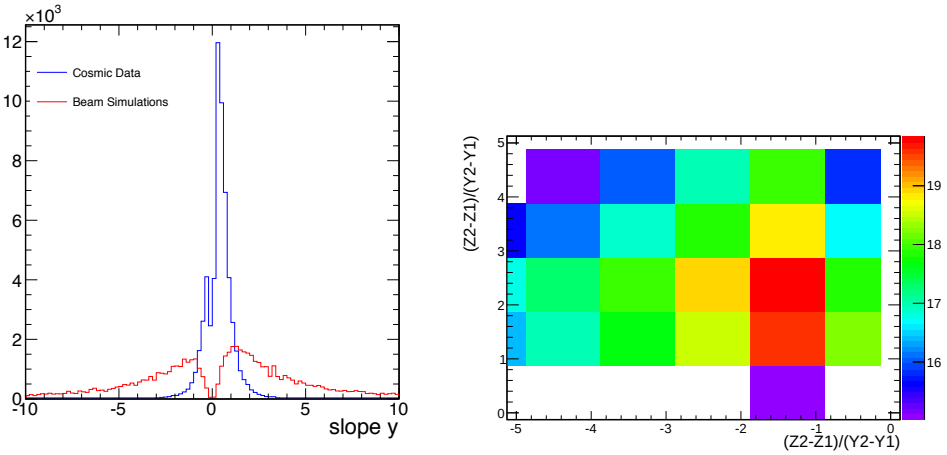

Figure A.2: Left: Slope in Y $\frac{Z2-Z1}{Y2-Y1}$. Right: plot shows the FOM for the inverse of slope distribution $\frac{Z2-Z1}{Y2-Y1}$.

variable. The figure shows the $\frac{Z2-Z1}{Y2-Y1}$ from 0 to 5 in Y axis and $\frac{Z2-Z1}{Y2-Y1}$ from -5 to 0 in the X axis. The maximum FOM is represented by the maximum color in the 2D distribution.

Furthermore, we show the reconstructed angle with respect to the beam direction after the cuts $\frac{Z2-Z1}{Y2-Y1} < -1$ or $\frac{Z2-Z1}{Y2-Y1} > 1$ and the rest of pre-selection cuts (one and only one reconstructed track, fully contained events and events with track length greater than 60 cm) in figure A.3. The distribution shows the cosmic background events in blue and the neutrino candidates in black. And the table table A.1 shows a summary of the cosmic background events after each of the cuts.

Table A.1: Cosmic background events

In fiducial	Cosmic cut	One track	Track length ($> 60cm$)	Fully contained	After PID cut
9194	757	612	558	64	24

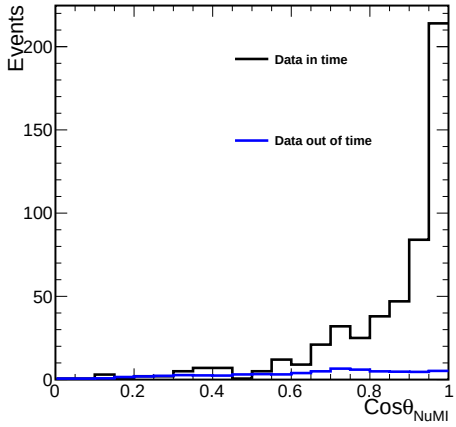

Figure A.3: Angle of the tracks with respect to the beam direction for pre-selected events, the black is the data in the spill window and the blue is the cosmic background events.

The cosmic background is rejected by applying the cuts in the inverse of the slope variable. More details for the studies can be found in NOνA doc-db [105].

Appendix B

Cross section analysis for configuration 1

This section shows the analysis distributions used to compute the cross section for configuration 1. This data set correspond to $1 \times 10^{19} POT$.

We start with the event selection, we show the input variables for the kNN selector in figure B.1. These distributions have been made using the pre-selection cuts from section 5.1.1. The left hand plots are area normalized and the right hand plots are POT normalized. Similar Data-MC disagreement for the POT normalized distributions as for configuration 2 in section 5.4. The output selector is shown in figure B.3. Again the Data-MC shows more disagreement between Data and MC in the first bin for both area and POT normalized distributions.

Next, we show Data-MC comparison for the scattering angle and the momentum prediction in figures B.4 and B.5 after the CC QE selection (preselection cuts and PID cut from Chapter 5), where left distribution is MC normalized to Data and right distribution is POT normalized. Similar normalization differences for both Data and MC after analysis selection.

Neutrino Energy and cross section as a function of energy

Using the momentum and angle prediction we calculate the neutrino energy spectrum for this configuration. The reconstructed neutrino energy is shown in figure B.6. Similar normalization differences for both area and POT normalized distributions.

Figure B.7 shows reconstructed energy with the predictions for the background in the left hand plot, where pink curve represents the background from RES, DIS, NC and COH interactions and red curve is the total MC including signal events.

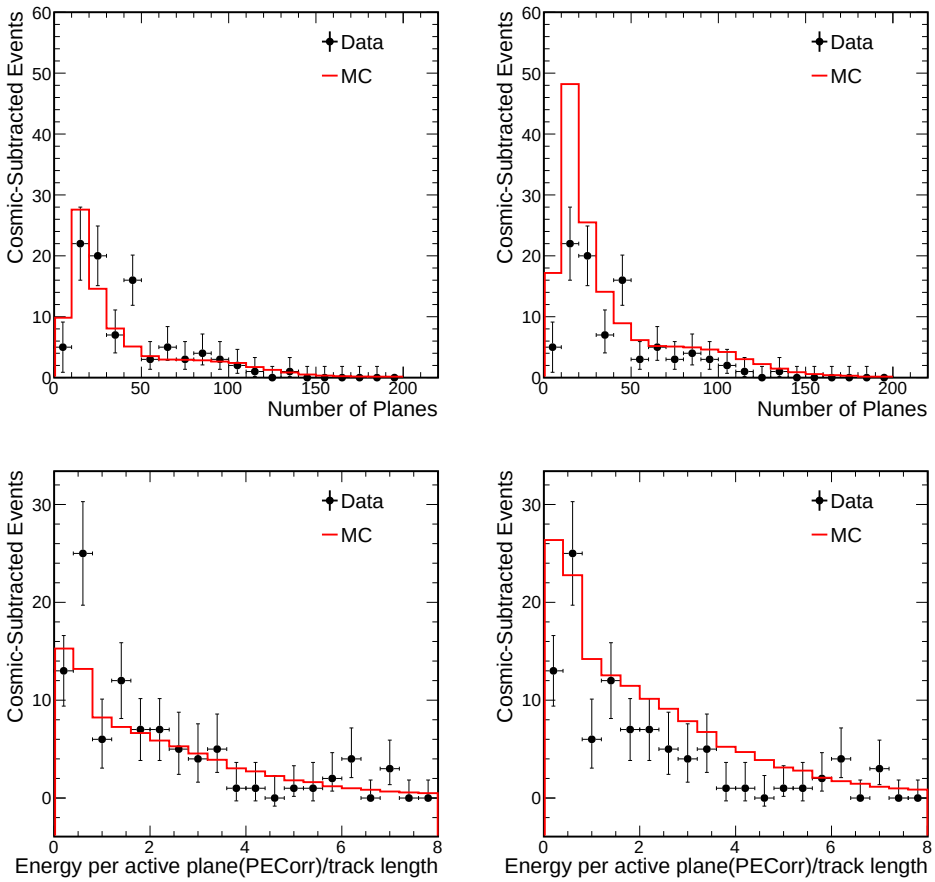

Figure B.1: Input variables for the kNN. The top distributions are the number of crossed planes by the event. The bottom plots are the energy per active plane to track length. Red is the total MC after pre-selection cuts and the black is the data after pre-selection cuts and cosmic background subtracted events.

Using the MC background prediction we subtract the background in Data and MC. The background subtracted plot is shown on the right hand distribution of figure B.7.

Using the ratio of ν_μ to $(\nu_\mu + \bar{\nu}_\mu)$ equation 6.11 we estimate the ν_μ component. The ratio as a function of energy is shown in figure B.8.

The efficiency as a function of neutrino energy is shown in the right hand distribution of figure B.8, we used the same definition used for configuration 2 from equation 6.12.

Using the MC simulations the expected signal and background number of events are shown in table B.1. The current data selection criteria gives 55 neutrino candidates and 11 cosmic background events.

Table B.1: Signal and background events

CC-QE ν_μ	CC-QE $\bar{\nu}_\mu$	CC RES	CC DIS	NC	COH	CC-QE ν_e	Total
27	11	11	4	5	1	1	59

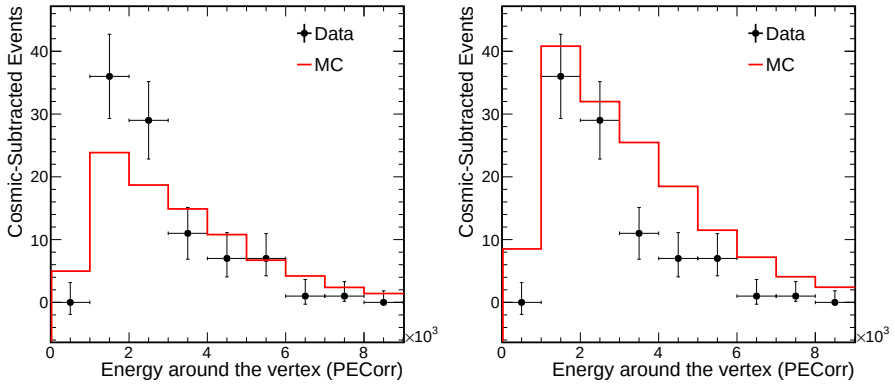

Figure B.2: Energy around the vertex. Red is the total MC after pre-selection cuts and the black is the data after pre-selection cuts and cosmic background subtracted events.

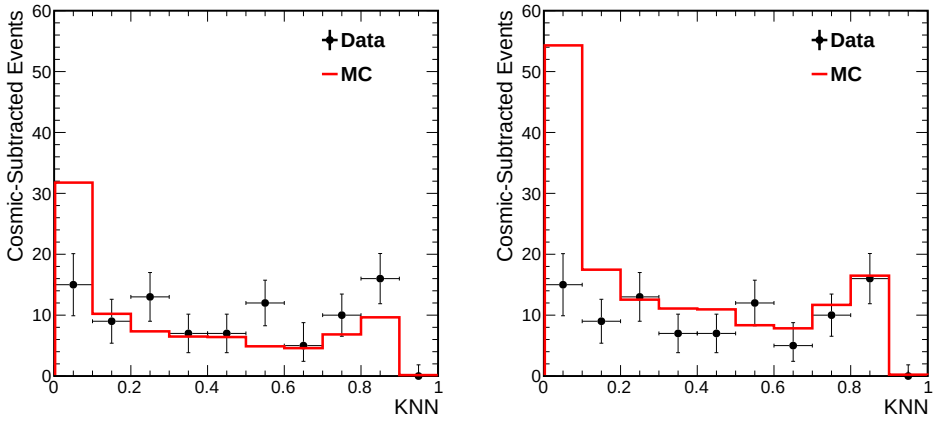

Figure B.3: Left: kNN area normalized. Right: kNN POT normalized for configuration 1.

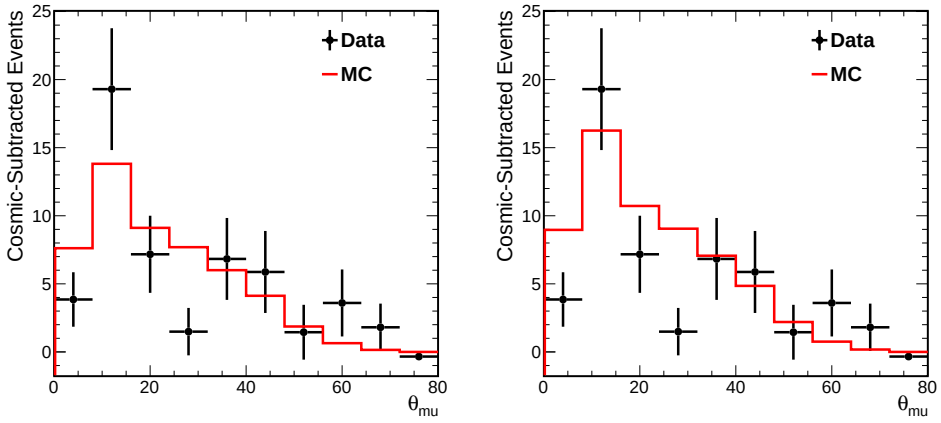

Figure B.4: Left: Scattering angle area normalized. Right: Scattering angle POT normalized for configuration 1.

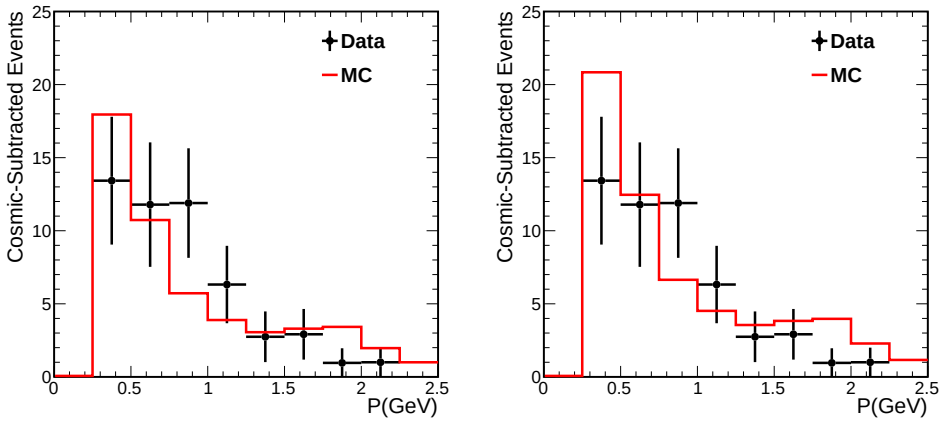

Figure B.5: Left: Momentum area normalized. Right: Momentum POT normalized for configuration 1.

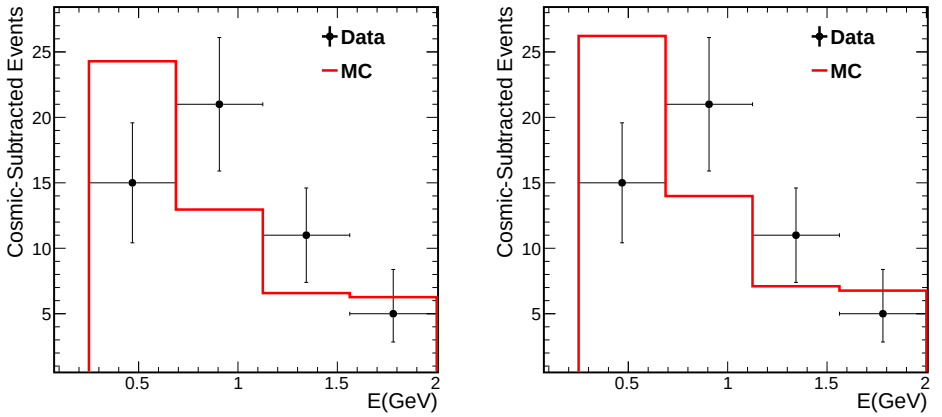

Figure B.6: Comparison of reconstructed neutrino energy for ν_μ CC QE selected events after cosmic background subtraction and MC simulation. Left: MC normalized to Data. Right: Neutrino energy POT normalized.

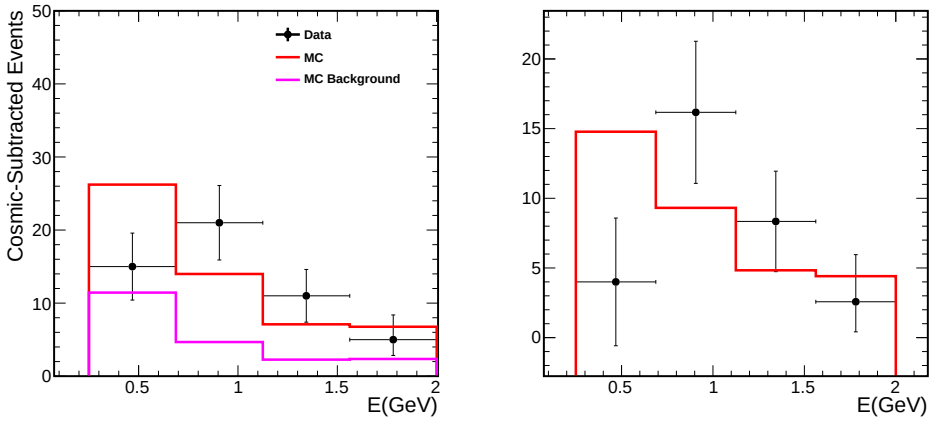

Figure B.7: Left: Comparison of reconstructed neutrino energy for ν_μ CC QE selected events after cosmic background subtraction and MC simulation for each of the interaction contributions. Red distribution is the total MC prediction and pink curve is the MC background prediction. Right: Comparison of reconstructed neutrino energy for events after cosmic and interaction background subtraction.

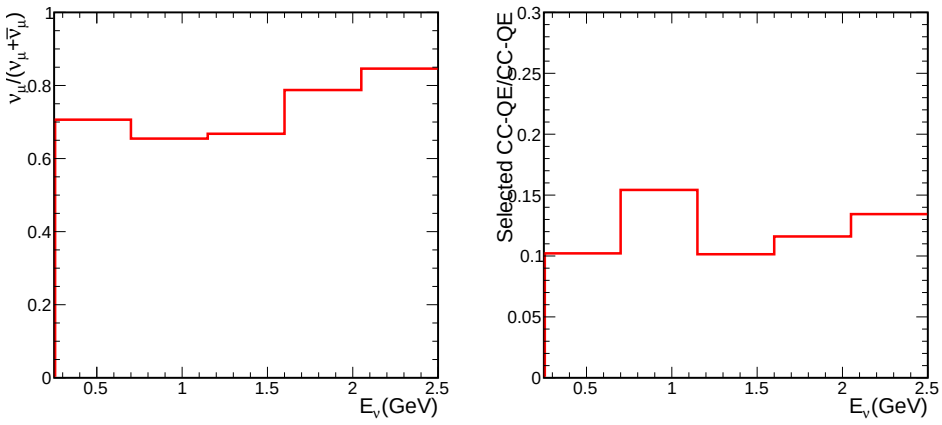

Figure B.8: Left: Ratio of ν_μ to $(\nu_\mu + \bar{\nu}_\mu)$ as a function of reconstructed neutrino energy for the CC QE selected events. Right: Efficiency as a function of energy for configuration 1.

Using the procedure described in Chapter 6, we calculate the cross section for configuration 1, since we have very small statistic for this configuration we show only one data point in figure B.9. This figure shows the extracted cross section and the GENIE true cross section prediction. We find good agreement between the Data and GENIE simulation for configuration 1 within the uncertainties.

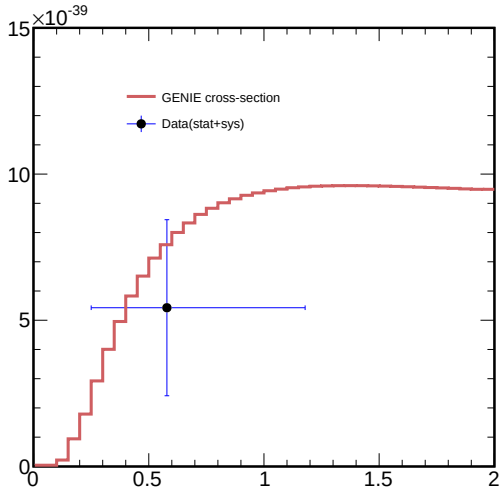

Figure B.9: Comparison of the calculated cross-section for the configuration 1 and the GENIE MC prediction.

Flux Integrated Single Differential Cross Section

We use similar procedure as used in Section 6.2 to compute the flux single differential cross section. Figure B.10 shows the four momentum transfer area and POT normalized. The POT normalized comparison shows Data-MC discrepancy for the first bin.

The left hand plot on figure B.11 shows the background prediction and the right hand distributions on this figure shows the four momentum transfer after the cosmic and interactions background subtraction.

Following the same procedure as in Chapter 6, we multiply the ratio ν_μ to $(\nu_\mu + \bar{\nu}_\mu)$ by the subtracted four momentum distribution in figure B.11 and dividing by the integrated flux, bin width, number of neutron target and efficiency from distribution B.13, we produce the flux integrated single differential cross section. This distribution is shown in figure B.14. The left plot MC is normalized to data and the right distributions are POT normalized.

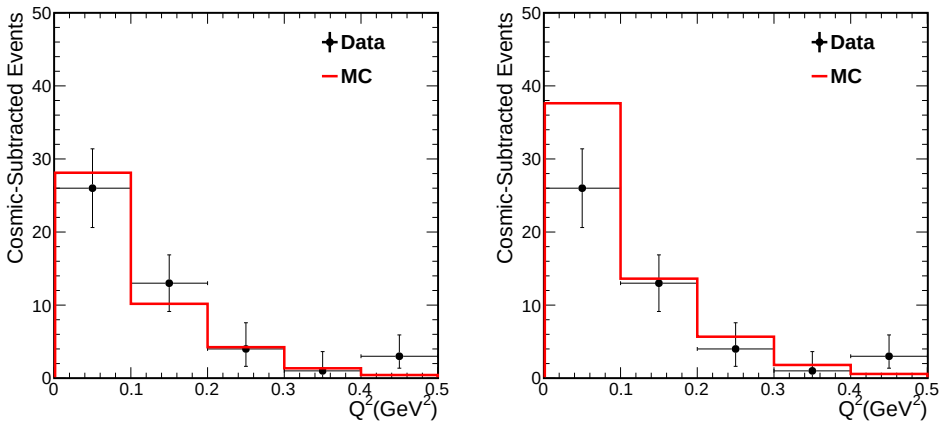

Figure B.10: Left: Four momentum transfer area normalized. Right: Four momentum transfer POT normalized for configuration 1.

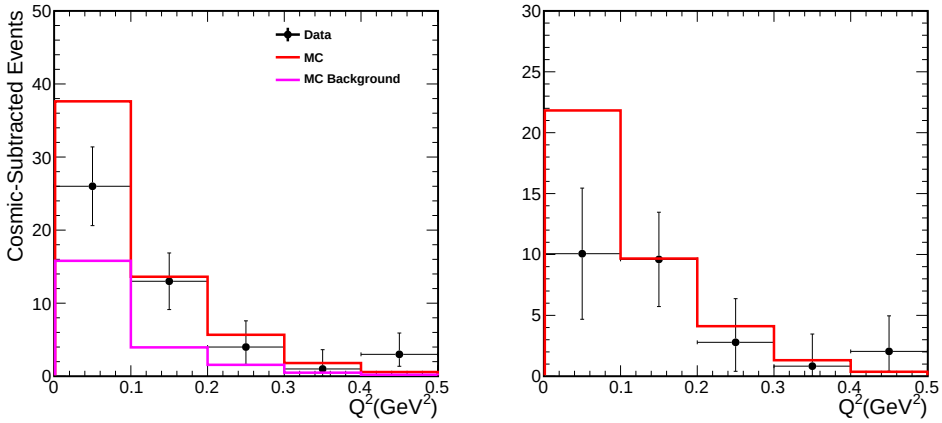

Figure B.11: Left: Four momentum transfer POT normalized, red curve is the total MC prediction and pink curve represent the irreducible background. Right: Four momentum transfer after cosmic and interactions background subtraction, POT normalized for configuration 1.

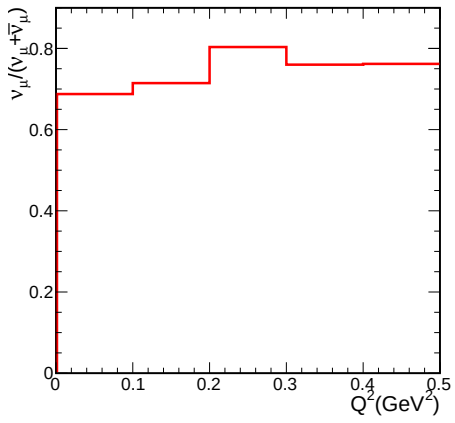

Figure B.12: Ratio of ν_μ to $(\nu_\mu + \bar{\nu}_\mu)$ as a function of four momentum transfer for the CC QE selected events.

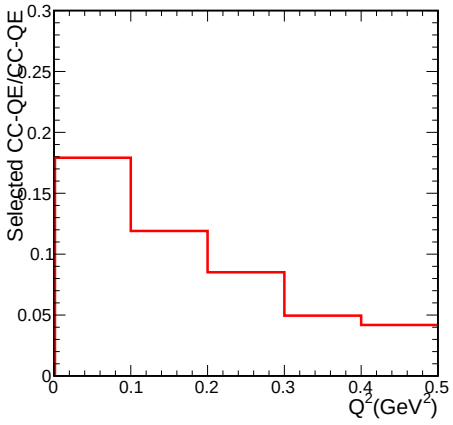

Figure B.13: Efficiency as a function of energy for configuration 2.

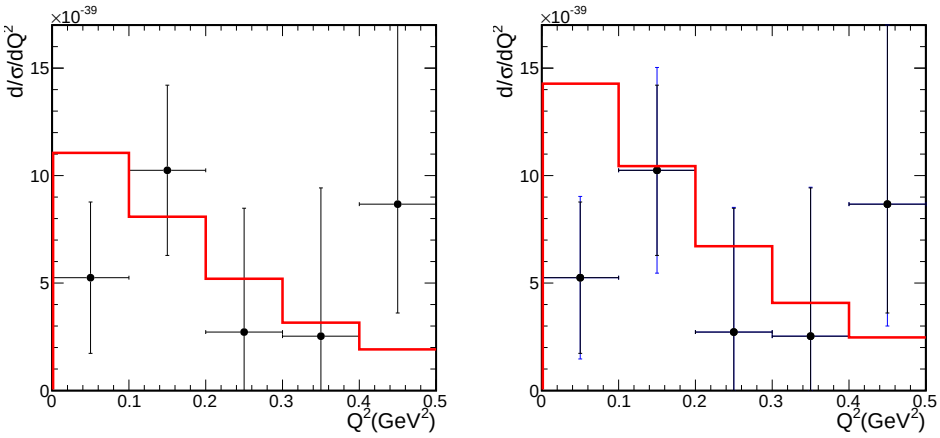

Figure B.14: Flux integrated single differential cross-section for configuration 1. Left: MC normalized to Data. Right: Distributions POT normalized.

Appendix C

Normalization checks

We study the Data-MC normalization. The MC prediction and data agrees within one sigma of systematic uncertainty. However, we made a study to investigate the source of normalization difference as a cross check. This appendix summary the studies, the list of checks include:

- Fit the data with the kaons and pions MC components.
- Cosmic Data-MC comparison, (cosmic exposure normalized).
- Study of bad channels.
- Comparison of the simulations used in this analysis and simulations used by MiniBooNE experiment in the study of NuMI off axis beam.

Data and MC simulations

Figure C.1 shows the reconstructed neutrino energy for the CC QE selected events in Data and MC simulations. In addition, we plot the reconstructed neutrino energy for each parent contribution (pions and kaons) in the left plot of figure.

A crude study was made to explore the Data and Monte Carlo comparison differences, we reweighed the neutrinos coming from kaon by a factor of 0.7. The right hand plot in figure C.1 shows the Data and MC comparison, gray distribution shows the neutrino energy after reweighing. We note comparison Data-MC neutrino has better agreement after the reweighing.

In addition, we fit simultaneously the MC predictions from pions and kaons with the data using $MC(total) = \alpha \times MC(pions) + \beta \times MC(kaons)$. This fit produces $\alpha = 0.8$ and $\beta = 0.7$ with a $\chi^2/NDF = 1.99/4$ the result is shown in left plot of figure C.2.

Normalizing the MC simulations to the data we find $\chi^2/NDF = 2.17/4$. The area normalized distribution is shown in the right plot of figure C.2. Both χ^2/NDF are very similar for

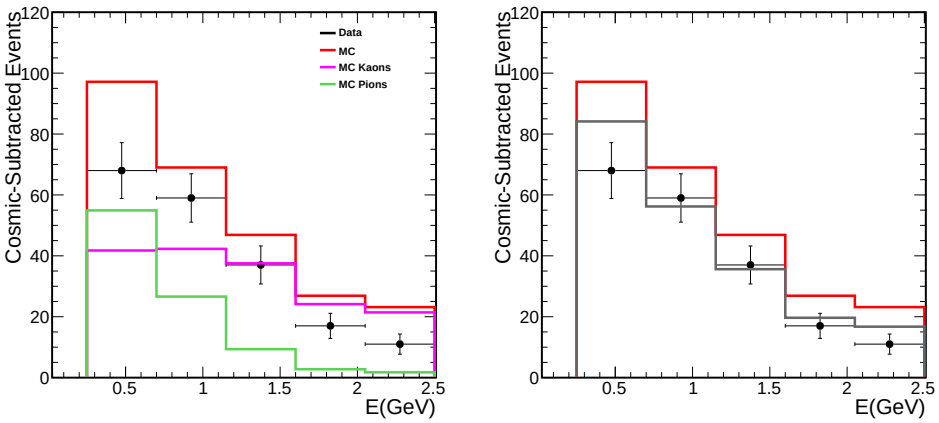

Figure C.1: Reconstructed Neutrino Energy. Left: Comparison of CC QE selected events and MC simulations. Green curve represents neutrinos produced by the pions parent and the pink curve is the neutrino energy from the kaons. Right: Gray color represents the MC after reweighing the kaons composition by 0.7.

the area normalized and the distributions after we fit the pions and kaons with our data. Also figure C.3 shows the ratio of pions to kaons as a function of the neutrino energy after POT normalization and from the result of the fit, ratio is very similar. This shows that Data-MC comparison is consistent and we do not find any problem from the simulations of our hadron production.

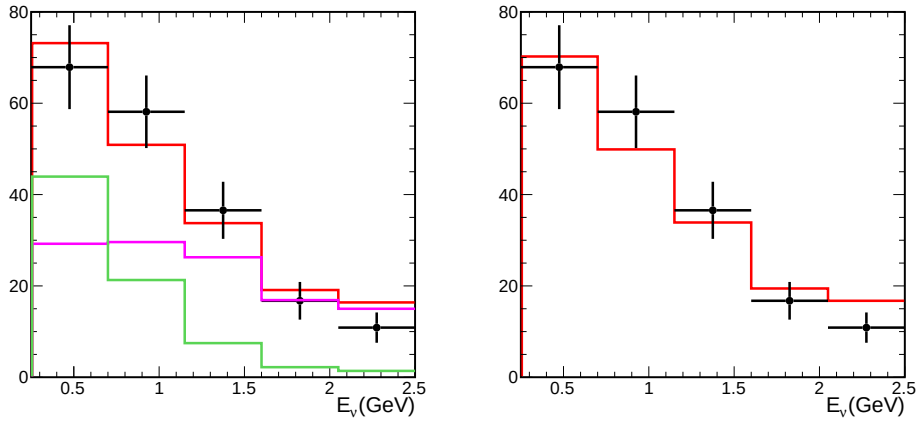

Figure C.2: Comparison of the CC QE selected events and the MC simulations after the fit.

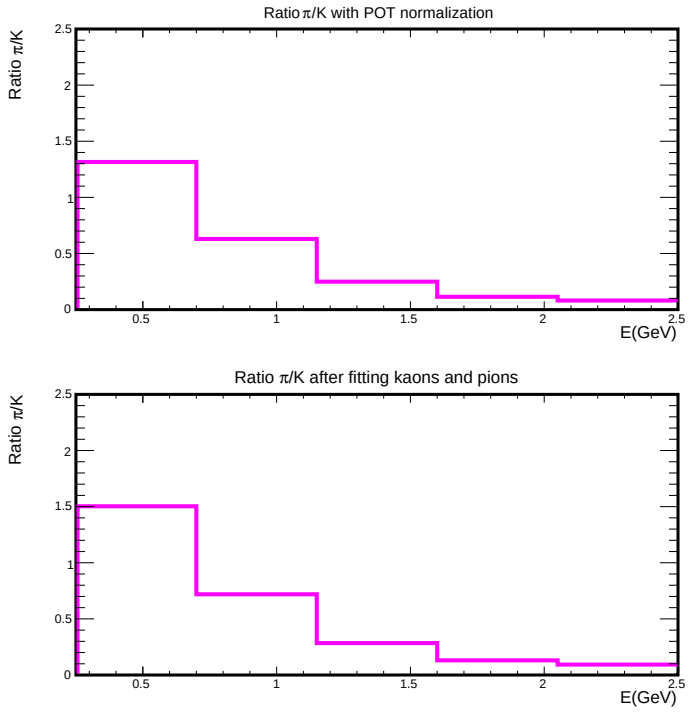

Figure C.3: Ratio of π/K as a function of neutrino energy. Top shows the ratio π/K with POT normalization and bottom shows the ratio after the fit of pions and kaons with the data.

Cosmic Data-MC comparison

Comparison of the cosmic data and cosmic MC simulation is made. The figure C.4 shows the cosmic Data and cosmic MC simulation, where the MC has been normalized by the data cosmic exposure. The comparison shows MC simulation agrees with the cosmic Data.

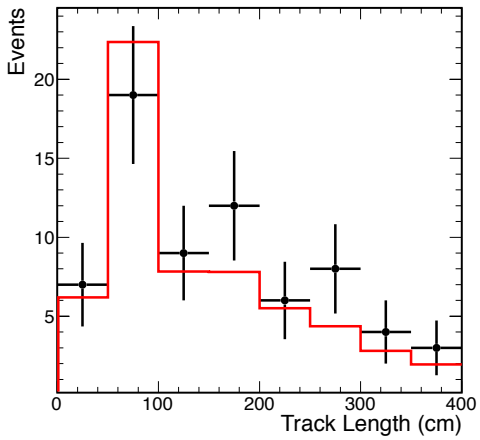

Figure C.4: Cosmic data and cosmic MC simulation. MC has been normalized using the data cosmic exposure. The red is the MC and black the cosmic data.

Bad Channels Study

We remove the data with shut off Front End Boards and make the Data-MC comparisons excluding these sub runs. We found similar Data-MC comparison. This study shows the comparison is not affected by the data with shut off FEBs.

In addition, we removed the bad channels determined with the cosmic data[99] and make the comparison again. We found Data-MC comparison is consistent with previous comparisons.

Comparing our simulations with external simulations used to study the NuMI beam at off axis location

The MiniBooNE experiment measured the ν_μ events in an off axis neutrino beam (NuMI) at 110 mrad. The study showed good agreement between data and MC simulations [106].

Exploring the Data-MC agreement from their measurement to constraint our MC. We compare our MC simulations with their MC simulations. Figure C.5 shows the flux comparison for the Near Detector Prototype and the NuMI at MiniBooNE detector, red distribution

is our MC simulation and the black is the MC used for the MiniBooNE collaboration on the left hand distributions and the ratio is shown in the right hand distribution.
Furthermore, we compare the cross sections. We use GENIE event generator and Mini-

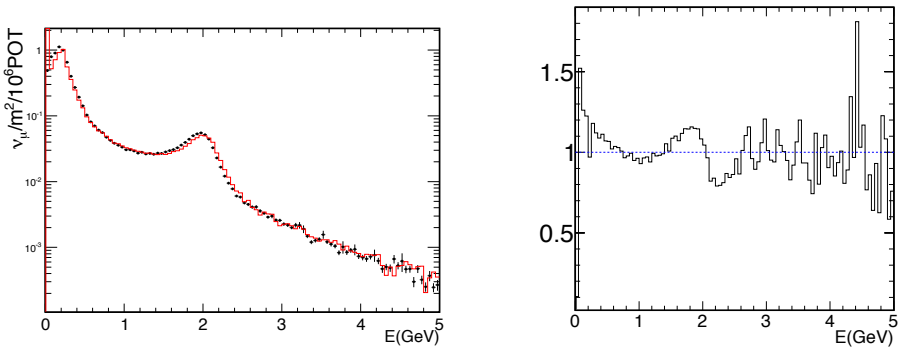

Figure C.5: Comparison of the flux at the Near Detector Prototype and the flux at the MiniBooNE detector [107]. Right: Ratio Flux at MiniBooNE detector to Flux at Near Detector Prototype.

BooNE uses NUANCE event generator, the figure C.6 shows the comparison for the cross section for GENIE and NUANCE.
Figures C.5 and C.6 shows the MC simulation differences between our simulation and the

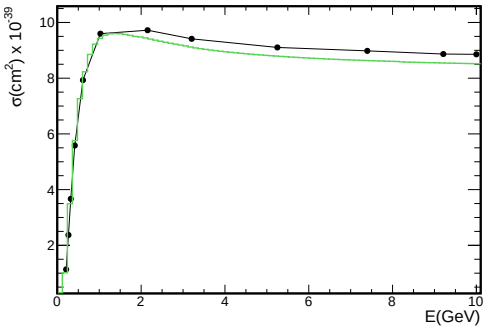

Figure C.6: Comparison of GENIE cross section and NUANCE cross section. The green curve corresponds to GENIE cross section with $Ma = 0.99GeV/c^2$ and the black is the cross section from NUANCE with $Ma = 1.02GeV/c^2$ [108].

simulation used by MiniBooNE experiment to study the NuMI off axis. However, those differences does not cover the normalization differences we see in our Data-MC comparisons.